DISSERTATION

A BIOMECHANICAL ANALYSIS OF VENOUS TISSUE IN ITS NORMAL, POST-PHLEBITIC, AND GENETICALLY ALTERED CONDITIONS

Submitted by

Kirk Cameron M^{c}Gilvray

Mechanical Engineering Department

In partial fulfillment of the requirements

For the Degree of Doctor of Philosophy

Colorado State University

Fort Collins, Colorado

Fall 2009

COLORADO STATE UNIVERSITY

June 11th, 2009

WE HEREBY RECOMMEND THAT THE DISSERTATION PREPARED UNDER OUR SUPERVISION BY KIRK CAMERON M^{C}GILVRAY ENTITLED "A BIOMECHANICAL ANALYSIS OF VENOUS TISSUE IN ITS NORMAL, POST-PHLEBITIC, AND GENETICALLY ALTERED CONDITIONS" BE ACCEPTED AS FULFILLING IN PART REQUIREMENTS FOR THE DEGREE OF DOCTOR OF PHILOSOPHY.

Committee on Graduate work

(Paul R. Heyliger)

(Susan P. James)

(Hiroshi Sakurai)

Advisor (Christian M. Puttlitz)

Department Head (Allan T. Kirkpatrick)

ABSTRACT OF DISSERTATION

A BIOMECHANICAL ANALYSIS OF VENOUS TISSUE IN ITS NORMAL, POST-PHLEBITIC, AND GENETICALLY ALTERED CONDITIONS

The incidence of vein disease is very high, affecting more than 2% of the hospitalized patients in the United States; a number that is expected to increase. Post phlebitic veins, the result of chronic deep vein thrombosis, is considered to be one of the most important venous disease pathologies. Unfortunately, little information is currently available on the biomechanical effects of thrombus resolution in the deep veins.

The aim of this research was to characterize the biomechanical response of both healthy and diseased venous tissue using a murine model. It was hypothesized that biomechanical response parameters derived from healthy and diseased tissue would give insight into the resultant clinical complications observed in patients following thrombus resolution.

Biomechanical analysis revealed that statistically significant deleterious changes in vein wall compliance were observed following thrombus resolution. Data also revealed that matrix metallopeptidase 9 expression has a statistically significant effect on the biomechanical response of the tissue. These results indicate that clinical complications following deep venous thrombosis manifest from significant decreases in the compliance of the vein wall.

Finite element analyses were also performed. Biomechanical data served as input material parameters for modeling. Finite element modeling was used to evaluate the response of the inferior vena cava under physiologic loads. The results indicate that peak stresses are generated in the circumferential direction of loading during luminal pressurization. Decreased dilatation was observed following thrombus resolution. The data indicates that deep venous thrombosis lead to increased vein wall stress in correlation with decreased luminal distensability.

Kirk Cameron M^{c}Gilvray
Mechanical Engineering Department
Colorado State University
Fort Collins, CO 80523
Fall 2009

AKNOWLEDGEMENTS

This work was supported by a grant (number: RFA-HL-05-014) provided by the National Institutes of Health (NIH) (Bethesda, Maryland).

A special thanks to Dr. Christian Puttlitz for his role as Co-Investigator in the aforementioned grant and also for his function as a mentor and for supplying invaluable guidance thought this research endeavor.

Thank you to Dr. Susan P. James for her role as a committee member.

Thank you to Dr. Paul R. Heyliger for his role as a committee member.

Thank you to Dr. Hiroshi Sakurai for his role as a committee member.

Thanks to Dr. Rajabrata Sarkar at the Northern California Institute for Research and Education (NCIRE) at the University of California San Francisco (UCSF) for playing the role of Principle Investigator for this funding mechanism.

Thanks to Dave Reed at the National Institute of Standards and Technology (NIST) in Boulder, CO for access to testing equipment and technical training.

Thanks to Khanh Nguyen and Lornie Phillip at USCF/NCIRE for supplying the murine vascular tissue used in this study.

Thanks to Wesley Womack for computer programming assistance.

Thanks to all of the auxiliary support received from the member at the Orthopeadic Bioengineering Research Laboratory (OBRL) including Dr. Brandon Santoni, Snehal Shetye, Ugur Ayturk and Amy Lyons-Santoni.

Thanks to my family, Alan (Dad), Susan (Mom), and Kyle (Bro) M^{c}Gilvray for support and encouragement.

Thanks to Jim, Sue, and Dave Sampson for back-up support and encouragement.

Thanks to Kizlow and Furio for being furry little friends.

DEDICATION

This work is dedicated to my lovely and loving wife, Ashley Marie M^{c}Gilvray.

TABLE OF CONTENTS

LIST OF FIGURES

LIST OF TABLES

LIST OF EQUATIONS

1.0 INTRODUCTION

Although the incidence of vein disease is relatively high [60], the investigation of the biomechanical properties of either healthy or diseased venous tissue is rather limited [20]. The need for this information is apparent when one considers that the biomechanical properties of cardiovascular tissue can be used as functional indicators of local vessel biology and the development/progression of disease pathology [34]. It is well-known that cardiovascular performance is a function of a number of biomechanical indices and parameters [78]. Previous studies, mainly exploring arterial tissue [6, 14, 18, 22, 28, 36, 39, 44-46, 59, 61, 63, 68, 69, 77, 89, 91, 92, 95, 97, 98, 100-109], have addressed the influence of mechanical parameters on various length scales due to disease states of the cardiovascular system. However, to our knowledge, there are no studies with regard to the biomechanical properties of either clinical or experimental post-phlebitic veins (PPV). The lack of biomechanical information about PPV is disconcerting when one considers that complications from acute and chronic deep venous thrombosis (DVT), the precursor to PPV, contribute to more deaths each year than AIDS and breast cancer combined, affecting between 1 to 2% of hospitalized patients in the United States [3]. Therefore, deep vein thrombosis is considered to be one of the most important venous pathologies [2].

The capacitive and efficient conduit function of the venous system is critically dependent on the biomechanical properties of the vein wall. Our understanding of venous function now extends beyond a simple passive conduit function, as the vasomotor and biomechanical characteristics of the vein structure allow modulation of

volume and flow throughout the cardiovascular system. Even slight changes in the biomechanical properties of the vein wall can cause significant shifts in the pressure-distension relationship of the vessel. This can affect proper venous return, particularly in the lower extremities where the hydrostatic venous pressure gradient is the greatest. A common and well-established disruption of normal venous function occurs in post-thrombotic syndrome, a clinical condition attributed to increased lower extremity venous pressure. Normal venous return is disrupted due to loss of venous valve function and decreased elasticity of the vein wall from post-inflammatory changes associated with thrombus resolution. Measurement of vein wall compliance in patients after deep venous thrombosis has shown decreased venous compliance [58], consistent with the fibrotic changes induced by thrombus resolution.

Post-thrombotic (or post-phlebitic) syndrome is a substantial health problem that manifests as pain, swelling, and progressive skin changes including chronic venous ulceration. Approximately 5% of individuals in the U.S. over the age of 65 have a venous ulcer, and the costs of venous ulcer care exceed 2% of the total health care costs [50, 67, 70, 87]. Treatment of deep venous thrombosis with anticoagulation effectively prevents pulmonary embolism but does not hasten thrombus resolution and does not prevent the subsequent development of post-thrombotic syndrome. Rapid spontaneous resolution of deep venous thrombosis is associated with a subsequent decrease in the incidence of post-thrombotic syndrome, and thus, there is increasing research interest in the cellular and molecular mechanisms involved in thrombus resolution.

Experimental models of venous thrombus resolution, including both mouse and rat models of vena cava ligation, have been used to define the cellular and molecular mechanisms of thrombus resolution. The mouse model of vena cava ligation coupled with genetically altered mice can definitively identify a role for individual genes in thrombus resolution. Although biomechanical studies of the rat vein wall have been described [73, 99], there are no biomechanical studies of the effects of thrombus formation on the mouse vein wall. The small size and delicate nature of mouse veins has challenged the development of reliable biomechanical measures of thrombus-induced changes in compliance, and the lack of such measures prevents us from defining the effects of individual genes on the biomechanical changes in the vein wall. Current studies implicating individual genes (urokinase-type plasminogen activator and CXC chemokine receptors) in thrombus resolution are thus limited to static and non-functional morphometric endpoints such as molecular expression, thrombus weight and histological composition [57]. Given the importance of the mouse as a model system for critically defining the role of individual genes in thrombus resolution, we sought to develop a reproducible method of accurately and quantitatively measuring the biomechanical properties of both normal and post-thrombotic mouse veins. Such an experimental approach would allow determination of the role of individual genes in the biomechanical changes of thrombus resolution.

Previous studies have demonstrated that vascular tissue will remodel if its mechanical environment is altered [48]. It is theorized that PPV-affected vessels possess a reduced capacity to distend. Thus, elevated intraluminal pressure is transmitted in the

lower extremity, contributing to the symptoms and complications of post-phlebitic syndrome [12, 13, 19, 52, 65]. Clinical symptoms are considered to be a direct consequence of changes in vein wall compliance. However, quantification of these biomechanical properties has not been reported. Accordingly, the prediction of the stress and strain states of blood vessels has become important for investigators studying how these factors influence the progression of certain vascular pathologies [93]. Clearly there is a need for both a better understanding of the pathophysiology of PPV and the resulting biomechanical consequences from chronic DVT. Direct measurement of physiologically-relevant biomechanical properties of vessels affected by PPV is technically challenging and has not been described.

Using models of thrombus resolution, we measured distinct thrombus-induced changes in the biomechanical properties of the vein wall which parallel those seen in human post-thrombotic syndrome. The current study described the load-displacement and stress–strain behavior of murine inferior vena cava that had been induced with chronic DVT using three experimental approaches: uniaxial tensile testing, biaxial tensile testing and nanoindentation compression testing. These data were utilized to determine the effects of DVT on vessel wall compliance and elasticity via material property measurements. In addition, biaxial tensile testing data gave insight into the biomechanical effects that the matrix metalloproteinase 9 (MMP-9) had on the biomechanical response parameters of PPV using a murine knock-out model, in which the specific protein MMP-9 expression was suppressed. These data served as input for a specific strain energy function that has been developed for soft tissues that assume

material anisotropy, highly nonlinear stress-strain relationships, and large deformations for implementation into a finite element (FE) model. FE predictions were computed to discern the differences between the *in vivo* biomechanical response of healthy and diseased venous tissue. The objective was to measure the biomechanical response of DVT-induced vessels and incorporate them into a comprehensive hyperelastic material model for FE analysis. The overarching goal of these current endeavors was to develop a finite element model (FEM) that can be used to investigate the mechanobiology of PPV secondary to DVT.

2.0 BACKGROUND

2.1 Blood Vessel Anatomy and Physiology

This work focused on the functionality and biomechanical properties of veins, specifically the murine infrarenal inferior vena cave (IVC) in order to examine the affects of deep venous thrombosis. Arterial anatomy and physiology will be largely ignored in order to focus on the germane venous tissue.

All vascular vessels are composed of similar tissue, and, in general, can be divided into arteries and veins; carrying blood away from or towards the heart, respectively. The vein wall has three general structural layers, called "tunics" that surround a hollow lumen. The innermost layer, called the tunica intima or interna, consists of a single layer of squamous, endothelial cells on top of a thin, elastic basement membrane called the internal elastic lamina. This internal elastic lamina is primarily composed of type IV collagen. The endothelial cells form a smooth inner

surface on the lumen, and acts as a selective barrier which specific cellular material and biochemical species are allowed to pass. The endothelium also serves as a signal transduction interface for the vessel [64]. The middle, much thicker layer is the tunica media, which consists of helically-arranged smooth muscle cells with elastic connective tissue fibers. These smooth muscle cells, which are under the control of the sympathetic nervous system, function to adjust the diameter of the lumen, thereby regulating the flow of blood through the vessel. Smooth muscle cells make up 40 to 60% of the medial portion of the vascular wall [55]. Interposed among the smooth muscle cells are variable amounts of elastic fibers and lamellae, reticular fibers (type III collagen), proteoglycans, and glycolproteins. Smooth muscle cells generate the extracellular matrix in which the constituents of the vascular wall are embedded. The extracellular matrix is an amorphous, mucopolysaccharide ground substance [55]. However, studies examining enzymatic degradation of ground substance have demonstrated that this non-fibrous connective tissue has little direct effect on wall mechanics [23]. The third, outermost layer is the tunica adventitia or externa, which is composed primarily of elastin and collagen connective tissue fibers. It primarily functions to support and protect the vessel. Type 1 collagen dominates the adventitia. The adventitial layer gradually becomes continuous with the surrounding local connective tissue. Structurally, veins contain a relatively high amount of collagen; the elastin/collagen ratio is about 1:3 [29].

To summarize, the main mechanically relevant constituents of the venous wall are collagen, elastin, and smooth muscle. These components are normally under

tension, or vascular tone as indicated by the contraction of the vessel length and diameter by about 40% when the vessel is isolated [72]. In general terms, veins have a larger diameter and smaller wall thickness to diameter ratio then other vascular conduits [99]. The thickness of the vein wall is chiefly controlled by the internal pressure of the vessel. The internal luminal pressure of veins (>20mm Hg) is much less then the pressure measured in arteries (120-70 mm Hg) [10]. This pressure differential is due to the vascular resistance blood encounters as it passes through the arterioles and capillaries. Vascular resistance acts to dissipate the pressure generated by the pumping heart. Rhythmic contractions of smooth muscles in the walls of the veins account for a small portion of blood movement. Mainly, blood flows through veins as a result of skeletal muscle action; skeletal muscles compress the venous tissue and squeeze blood though them [10]. Within veins, flaps of tissue act as one-way valves that allow blood to flow only toward the heart, preventing blood pooling and/or backflow in the extremities due to gravity.

Venous vasculature serves not only a conduit function, but also through its mechanical properties, plays an important role in modulating pressure and flow in the entire cardiovascular system [21]. A majority of the blood volume is contained in the systemic veins. With their passive and active wall properties, veins contribute to the distribution of blood in the periphery, and between the periphery and heart, influencing cardiac filling and regulating cardiac output [20]. The systemic venal blood volume more than equals the total arterial blood volume of the cardiovascular system, thus venous tissue fulfills a variable reservoir function [99]. Intact, the reservoir function of

veins is well understood, with the venous vasculature accommodating 60-75% of the blood volume of the body [15]. Veins also participate in complex cardiovascular reflexes and appear to be an important determinant in homeostatis [11]. Even slight changes in the biomechanical properties of the vein wall can cause significant shifts in the pressure-distension relationship of the vessel, and thus affect the entire cardiovascular system.

2.2 Blood Vessel Mechanics

Surprisingly little information can be found in the literature on the biomechanical properties of veins, particularly the vena cava [20]. Experimental data on the deformation characteristics of human or animal vena cava are very limited. However, the mechanical properties of veins are determined by their highly variable micro-structural composition [74]. Meaning there is a clear understanding that the biomechanical response parameters of veins have a structural basis [29, 99]. Veins display a large variety of structural inhomogeneity accompanied by an equally large range of active biomechanical responses [99]. The viscoelastic behavior of hierarchical biomaterial, such as vascular tissue, reflects primarily the properties of the fibrous components [4]. The main constituents of the venous wall are collagen, elastin, and smooth muscle. However, in the venous wall, these elements are not organized into perfectly distinguishable layers and laminae, but form a network of collagen bundles throughout the wall, with interwoven elastic and muscular fibers [33, 51, 56, 84, 96]. This network of fibrous tissue creates a continuum that does not mechanically conform to linear elasticity, with highly nonlinear stress-stain behavior, the existence of

hysteresis, and advanced creep under constant stress and stress relaxation under constant strain [29]. It is also known that this microstructural organization leads to anisotropic mechanical responses (i.e., circumferential versus longitudinal). Vascular tissue is assumed to be an incompressible, nonlinear, anisotropic and viscoelastic soft biomaterial. Vascular tissue is anisotropic as a consequence of the preferred orientation of the collagen fibers, and inhomogeneous, since the collagen density and degree of collagen cross-linking vary spatially within the tissue [66]. The incompressibility assumption is very commonly imposed when one considers vascular mechanics [8, 9, 18, 23, 29, 34, 47, 80, 82]. Under the incompressibility assumption, the analysis of stress and strain in the vessel wall is greatly simplified because the deformation in the luminal direction is explicitly determined by those in the circumferential and longitudinal direction [34].

Veins are extremely compliant (elastic modulus less than 1MPa) when subjected to *in vivo* pressure magnitudes. This is largely due to the mechanical properties of the elastin in the vessel wall. When loaded, elastic fibers are easily extended by 50 to 70% of their original length during protein chain unfolding. Elastin bears a large portion of the circumferential distending force in the vessel wall, and there is a direct relationship between the strength of the wall and the number of elastic lamellae present [23]. Collagen is the second major fibrous connective tissue in the wall. The structure of collagen is fundamentally different from that of elastin as it is composed of closely-wound helical chains. The chains of these proteins are tightly cross-linked, thereby restricting their extensibility. In contrast, collagen fibers are fully uncrimped at 2 to 4%.

The elastic modulus of collagen and elastin clearly demonstrates these function-property relationships wherein stretched collagen is several hundred to one thousand times stiffer than stretched elastin [23]. These two fibrous constituents dominate the biomechanical behavior of the vascular wall. When veins are pressurized and distended circumferentially, the elastic lamellae and some of the collagen fibers in the media tunica are stretched [23]. The collagen fibers in the adventitia are not stretched unless the vessel is over distended to extreme, non-physiological levels. At high internal pressure, the collagen network becomes rigid, limiting vascular distensability. Thus, much of the *in vivo* service load on the wall is born by elastin.

Connective tissue content alone does not completely account for the mechanical behavior of the vessel, suggesting that architectural as well as compositional differences are important determinants of vessel wall behavior [23]. Mechanical forces are also known to significantly affect the metabolism, phenotype, and secretory pathways of vascular cells composing the wall tissue, thus affecting the biomechanical response of the tissue [16]. Among these influences, shear stress and radial or circumferential stretch are the most commonly suspected mechanical regulatory parameters for endothelial and smooth muscle cell metabolism [27].

2.3 Cardiovascular Disease

Cardiovascular diseases (CVDs) are the leading cause of death in the United States and most other developed nations. The most excepted theory for the development of CVDs is that injury to the endothelial layer of the lumen is the initiating

cause of CVDs. The initial insult can be mechanical, chemical, or hemodynamic. Following insult, the damaged endothelial cells transport low density lipoproteins from the blood to the subintimal layer. Lipid oxidation during transport from the plasma or within the subendothelial space attracts monocytes and other inflammatory cells, leading to further endothelial damage [75, 76]. Macrophages endocytose lipids and low density lipoproteins, which they are unable to metabolize, leading to the formation of foam cells. Foam cells are derived from both macrophages and smooth muscle cells, which have accumulated low density lipoproteins that have been oxidized by reactive oxygen species produced by the endothelial cells. Foam cells are macroscopically visualized as fatty like streaks, and typically line the intima media of the vasculature. Foam cells continue to accumulate within the subendothelial space, eventually leading to a necrotic lipid core composed of cholesterol and cholesterol esters, foam cells, and cellular debris from dead foam cells [24]. The inflammatory cells and the damaged endothelial cells also secrete cytokines that attract smooth muscle cells from the medial layer of the vessel wall to the intima, and stimulate them to convert from a contractile to a synthetic phenotype [75, 76]. These cells produce fibrous tissue that surrounds the necrotic lipid core in a response resembling wound healing. Matrix proteins, proteoglycans, and elastin may also be synthesized by the synthetic smooth muscle cells, resulting in the formation of a layer of fibrous tissue surrounding the core [42]. The resultant conglomeration of lipids and fibrous tissue is called atherosclerosis plaque. This healing cascade is also typically associated with a thickening of the intimal layer of the vessel wall. The increased mass and irregular composition of the intima

results in atrophy of the medial layer and inflammation of the adventitia, thereby extending the effects of the disease through the entire vessel wall [83]. Histological studies have demonstrated that CVD causes qualitative changes in the hierarchical cellular microstructure of the vessel wall [88].

The present work focuses the specific cardiovascular disease (CVD), post-phlebitic syndrome (PPS), which is a consequence of chronic deep venous thrombosis (DVT). Succinctly, DVT occurs when a thrombus forms in one of the deep veins of the legs, pelvis or arms following the CVD cascade outlined above. The thrombus embedded in the vessel wall causes flow occlusion and an inflammatory reaction. When a thrombus forms in the endothelium, it stimulates a hyperemic inflammatory response that initiates a tissue organization cascade. The clot is invaded by granulomatous host response cells and is replaced by fibrous tissue [49]. A vigorous release of pro-inflammatory cytokines and leukocyte influx of neutrophils typically occurs, followed by monocyte and macrophage involvement [17]. This cascade promotes remodeling of the vessel wall in the region of the thrombus. Studies have also demonstrated that DVT results in the accumulation of extracellular matrix proteins (tropoelastin and fibronectin) and collagen deposition in the remodeling vessels, which is typically associated with localized activation of matrix metalloproteinases (MMPs) [30]. Thrombus retraction and organization eventually leads to recanalization and endothelialization, a process that destroys all the valves in the affected segment and produces an enlargement of the collateral venous channels [49]. Remodeling changes in the vessel wall also lead to prolonged venous hypertension, producing clinical

complications that can include persistent edema, pain, purpura, skin pigmentation, eczematoid, dermatitis, pruritus, ulceration, cellulitis, and pulmonary embolism. Many fatal emboli originate from thrombi in the proximal lower limb or the pelvis. Each year approximately 200,000 patients in the United States die as a result of thrombi embolism [49].

From a structural and material perspective, cardiovascular disease can fundamentally be associated with changes in the biomechanical properties of the vessel wall. Studies have demonstrated that the mechanical properties of cardiovascular tissue can be used as functional indicators of local vessel biology and the development/progression of diseases pathology [34]]. It is believed that vascular disease, both acute and chronic, leads to quantitative changes in the biomechanical and physiological response parameters of the diseased tissue in direct correlation with the formation of atherosclerosis plaque (AP). As alluded to above, atherosclerosis plaque is associated with the accumulation of lipids, calcification, fibrous tissue, and cellular debris in the vessel wall. AP progress also leads to stenosis of the lumen, which is manifested as numerous clinical complications. It has been shown that diseased cardiovascular tissue is heterogeneous with distributed regions of fibrous tissue, calcification, lipid, and hematoma [24]. In order to fully understand how these changes in tissue architecture affect the *in vivo* physiological response of the diseased vascular conduit, a spatial mapping of the vessel wall biomechanical properties must be determined.

3.0 SPECIFIC AIMS

The overreaching goal of this research was to demonstrate that alterations, secondary to DVT, in that the vessel wall material properties lead to significant deviations in vessel mechanics and function. In order to achieve this goal the following specific aims were identified and completed.

3.1 Specific Aim-Uniaxial Tension Testing

The primary aim was to present previously unpublished data that correlates the affects of DVT on the longitudinal biomechanical changes in DVT-induced murine IVC. Concisely, uniaxial tension testing involved applying a quasi-static longitudinal load to planar sheet of vascular tissue; recording the biomechanical parameters of interest. The resultant outcome data focused on the relationship between both healthy and diseased longitudinal biomechanical indices.

3.2 Specific Aim-Nanoindentation Testing

The primary aim of the nanoindentation work was to characterize and map, on a cellular scale, the differences in material properties that exist in healthy and diseased murine IVC tissue in the three primary axes of loading (longitudinal, circumferential, and luminal direction). Statistical differences in these biomechanical parameters were discerned between the healthy and diseased tissue, and in each of the aforementioned axes of loading (not only when comparing healthy to diseased, but also when comparing healthy to healthy, and diseased to diseased).

3.3 Specific Aim-Biaxial Stretch Testing

Biaxial experimentation data was used to determine the material constants derived from a specific strain energy function, which were then incorporated into a finite element model (FEM). Biaxial stretch testing involved applying simultaneous loads to the longitudinal and circumferential cross-sections of a planar sheet of venous tissue. From these experiments stress-strain relationships were derived. In addition to the parameters required for finite element modeling, biaxial tension testing provided data on the biomechanical effects of MMP-9 on DVT and the resultant mechanical consequences insufficiency of this protein.

3.4 Specific Aim-Finite Element Modeling (FEM)

The primary aim of the FEM was to develop and validate (using biaxial data sets) a simple "straight tube" model that mimics the biomechanical responses observed from the battery of biomechanical testing presented in this study. It was hypothesized that this model would give insight into the vessel wall stress and strain distribution that cannot be duplicated via experimentation or measured clinically.

4.0 SPECIMENT GENERATION - MODELS OF THROMBUS RESULUTION

All animal surgeries were performed by licensed vascular surgeons at the Venous Center, UCSF Division of Vascular Surgery, San Francisco, California under the supervision of Rajabrata Sarkar M.D., Ph.D. All animal studies conformed to the *Guide for the Care and Use of Laboratory Animals* published by the US National Institutes of

Health (NIH Publication No. 85-23, revised 1996.). To examine the effects of DVT resolution on wall biomechanics two distinct DVT induced murine models were used [17, 41]. These models have demonstrated a strong correlation with thrombotic predisposition clinically and histologically. Creation of the first treatment group (designated as No Flow or Ligation) involved complete ligation of the murine inferior vena cava (IVC) inducing stasis laminar thrombi as previously described in our laboratory and by others [17]. In brief, under isofluorane anesthesia, the infrarenal vena cava of adult mice was ligated immediately below the renal veins after division of all lumbar branches to the iliac bifurcation. Following seven days of thrombus resolution the mice were euthanized and the IVC was freed from the remaining thrombus for biomechanical testing (Figure 1). The seven day time point was chosen because the thrombus becomes surgically inseparable from the vein wall after this time point [35]. The second thrombus resolution model (designated as Low Flow) utilized was the cava flow restriction which exhibits more rapid thrombus resolution due to ongoing thrombus recanalization due to peri- and intra-thrombus blood flow [17, 41]. The cava flow restriction model was generated as previously described [85]. The endothelium of the inferior vena cava was injured by application of a vascular clamp for 15 seconds to the area below the renal veins, and then a defined caval stenosis was generated by tying a suture around both the vena cava and a rigid suture of defined size (5-0 polypropylene) and then the polypropylene suture was removed allowing the constricted vena cava to expand slightly. Residual caval blood flow (10-15%) was confirmed with a flow probe (Transonics, Ithaca, NY). By 28 days in this model the remaining thrombus is laminated

to the vein wall and these caval specimens were harvested at this time point for biomechanical testing. Sham specimens were also created for each murine model and underwent identical laparotomy, pericaval dissection and branch ligation but without caval occlusion or constriction. Samples for biomechanical testing consisted of IVC segments collected caudal to the renal veins junction and cranial to the iliac bifurcation. Samples were carefully transected longitudinally through the vascular wall creating a planar vascular sheet. Harvested IVC samples were stored in cool isotonic saline (0.9%w/v sodium chloride) and biomechanically tested within 48 hours post sacrifice.

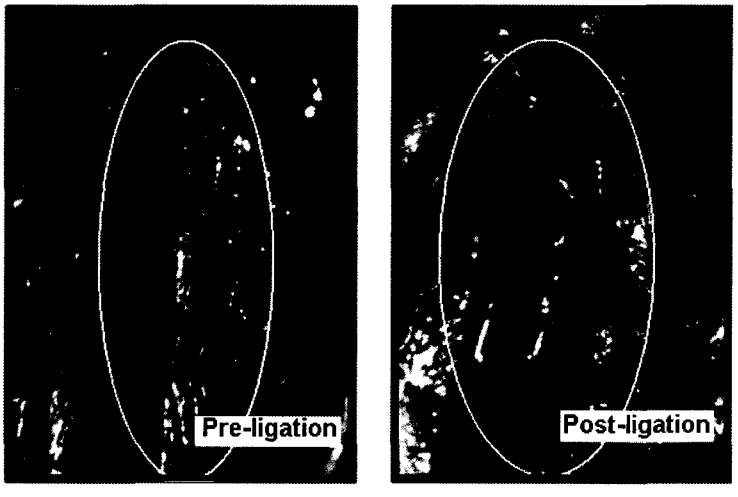

Figure 1: A stasis-based model was used to generate DVTs. The murine inferior vena cava has been highlighted, demonstrating the inferior vena cava is exposed for ligation. A nylon ligature is placed infrarenally and the vena cava is occluded. A surgeon is placing a ligature around the exposed vena cava (LEFT). Clot formation observed after seven days in vivo (LEFT).

5.0 Uniaxial Tension Experiment

5.1 Uniaxial Tension Experiment: Background

The primary focus of this specific aim of the study was to determine the biomechanical properties of murine vena cava, both healthy and those with induced DVT. It was determined that uniaxial tensile testing of cardiovascular tissue "strips", specifically murine inferior vena cava transected longitudinally to create a planar sheet, provided a practical and useful method to extract some of the more relevant biomechanical parameters. Specifically, both structural and material properties were derived from these experiments.

5.2 Uniaxial Tension Experiment: Methods

Quasi-static uniaxial tensile tests were performed on the planar sheets of murine vena cava tissue. In order to grip the specimens, the tunica externa on the extreme ends of each planar vessel sheet were chemically fixed to polymethylmethacrylate (PMMA),(GC America Inc., Alsip, IL, USA) coupons using a cyanoacrylate gel (Loctite, Avon, OH, USA) (Figure 2). To insure that the mid-substance of the samples was not adversely affected during the mounting procedure, care was taken to insure that only the extreme dimensional aspects of the vessel came into contact with the PMMA coupons and the cyanoacrylate gel. Following fixation, the testing constructs (PMMA coupon-IVC-PMMA coupon) were soaked in isotonic saline (sodium chloride 0.85-0.90% w/v) for a minimum of 30 minutes to insure complete equilibrium hydration during

testing. Following hydration, the coupon-sample-coupon constructs were attached to the testing system (Figure 2).

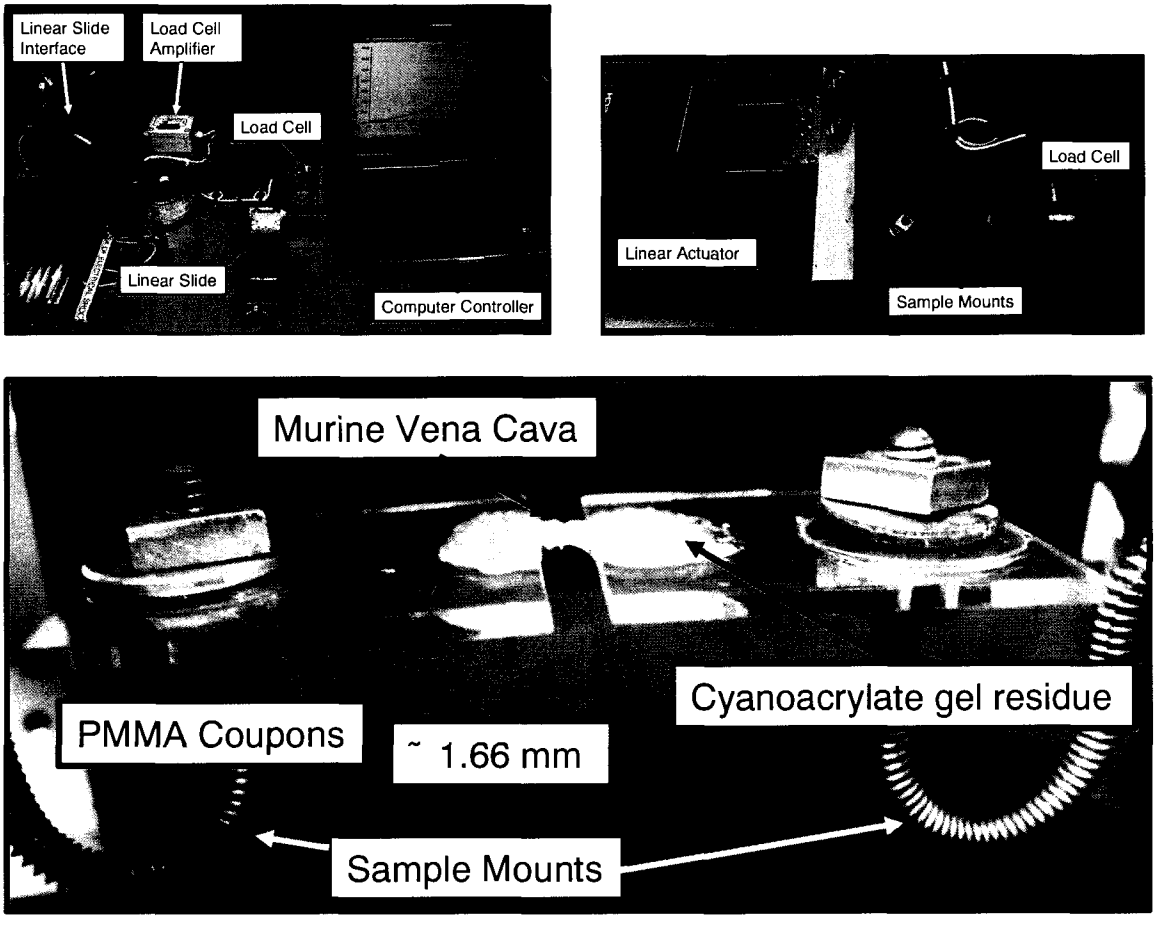

Figure 2: Uniaxial tension experiments testing system. Murine IVC mounted for uniaxial testing (*Bottom)*.

Samples constructs were aligned in the uniaxial testing machine to minimize sample shear loading during testing. A static preload of one gram was applied to all specimens, after which the sample was allowed to relax for 5 minutes at which time high resolution (8M pixel, PowerShot S80, Canon, NY, USA) digital images were taken from multiple perspectives. All images were captured at room temperature and within

eight minutes after removal of the specimens from the saline bath. Image data were used to determine the specimen's dimensions (for cross-sectional area and gauge length calculations), which were required for *post hoc* transformation of the load-displacement data into the stress-strain space. Sample thickness, width, and gauge length was determined by taking length measurements at five equally-spaced locations along the vessel using imaging software (ImageJ 1.38x, National Institutes of Health, Bethesda, MD). Ten cyclic tensile loads ranging between 0% and 2% strain were applied for the purpose of preconditioning and to minimize the viscoelastic effects on the measured biomechanical responses.

Each sample was tested in quasi-static uniaxial tension at a displacement rate of 0.33mm per second until failure. Force and displacement data were collected at a rate of 60Hz. Structural properties (failure force, failure displacement, and stiffness) were calculated from the resulting force-displacement data. All biomechanical tests were performed within ten minutes after removal from the saline bath. Failure was characterized when the mechanical integrity of the sample was lost, indicated by a substantial decrease in the monotonically-increasing force-displacement behavior as measured by the load cell and loading apparatus. Stiffness was defined as the slope of the load-displacement curve in the linear portion of the loading profile. Using a linear trend line generator, an equation of the general form $y=mx+b$ was fitted to the initial linear loading portion of the curve, where m is the slope of the line or the sample stiffness. Material properties (stress, strain, and elastic modulus) were calculated by normalizing the structural properties to the aforementioned geometric parameters.

Normal engineering stress (σ) was determined as the ratio of applied load (F) to the product of the original width (w) and thickness (t) (cross-sectional area) of the specimens following full relaxation from a one gram pre-load.

$$\sigma = \frac{F}{wt} \qquad \textbf{Equation 1}$$

Normal engineering strain (ε) was calculated as the instantaneous deformed length (l_{final}-$l_{initial}$) of the specimens divided by the original length ($l_{initial}$) of the specimen following full relaxation from a one gram pre-load. Displacement data at failure was standardized to the pre-test gauge length to characterize failure strain.

$$\varepsilon = \frac{l_{final} - l_{initial}}{l_{initial}} \qquad \textbf{Equation 2}$$

Elastic modulus was defined as the tangent modulus, namely as the first derivative of stress with respect to strain in the linear portion of the stress-strain profile. The elastic modulus was determined by finding the slope of the stress-strain curve in the linear portion of the loading profile, similar to the formulation of stiffness.

Statistical significance in the aforementioned biomechanical parameters between groups was determined using a student's t-test (SigmaStat, Systat Software Inc. Richmond, California, USA). P-values less than 0.05 were considered statistically significant. If equal variance tests between specific data sets failed for a given comparison then a Mann-Whitney rank sum test was performed, where p-values less than 0.05 were considered statistically significant.

5.3 Uniaxial Tension Experiment: Results

Samples from both DVT-induced models macroscopically exhibited yellowish plaque deposition on the luminal aspect of the planar sheet construct. Plaque deposition varied across the two flow-restricted models and ranged from small, discrete islands of deposition to complete wall coverage. Control samples did not show macroscopic signs of discoloration or deposition.

Complete ligation (No Flow) had the most profound effect on the geometric parameters. Specifically, complete ligation of the vessel resulted in a significant mean area increase ($p=0.020$) by 379% as compared to the mean area of the controls. No Flow samples also demonstrated a significant areal increase of 350% as compared to the Low Flow group ($p=0.018$). Furthermore, the No Flow sample population exhibited significantly greater mean thickness than control values ($p=0.018$). The initial gauge length was equivalent for all groups. No statistical differences were noted between the Low Flow and control groups for any of the geometric parameters.

Treatment	n	Width (mm)	Thickness (mm)	Gauge Length (mm)	Area (mm^2)
Controls	8	1.5945 ± 0.358^{b}	0.425 ± 0.109^{a}	4.2131 ± 1.933	0.667 ± 0.180^{d}
No Flow 8Day	9	$2.830 \pm 1.394^{b,c}$	0.954 ± 0.442^{a}	2.8000 ± 1.0422	$3.197 \pm 2.735^{d,e}$
Low Flow 28Day	8	0.915 ± 0.283^{c}	0.808 ± 0.363	3.5930 ± 0.5542	0.711 ± 0.297^{e}
		(a) p=0.018, (b) p=0.031, (c) p<0.001, (d) p=0.020, (e) p=0.018			

Table 1: Inferior vena cava geometric parameters (means ± standard deviations) calculated following preconditioning and relaxation under a one gram preload. Like letters indicate statistical differences ($p<0.05$) corresponding to the given P-values.

Low Flow samples demonstrated a 313% failure load increase, from 0.15 N to 0.47 N, as compared to the control group (p=0.003) (Figure 3). The control group demonstrated a significantly lower mean structural stiffness as compared to the two flow-restricted groups (Figure 3). The difference in stiffness between the No Flow group (0.24 N/mm) and the Low Flow population (0.31 N/mm) was not statistically significant. The DVT-induced models were statistically equivalent to the control groups with respect to failure displacement.

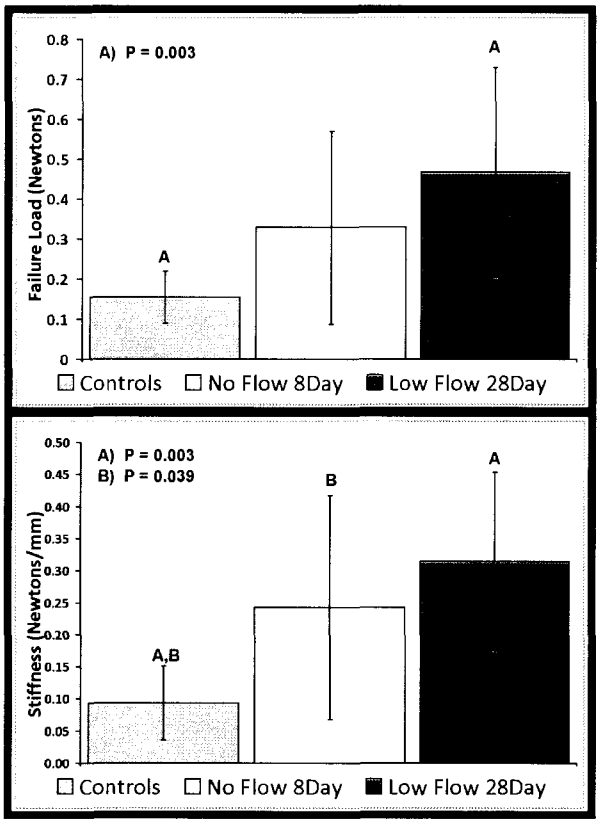

Figure 3: Failure load (TOP) and stiffness (BOTTOM) calculated following quasi-static ramp to failure testing. Like letters indicate statistical differences ($p<0.05$) corresponding to the given p-values. Calculated means are shown with standard deviations error bars.

Reflecting the structural parameters above, the Low Flow samples demonstrated significant increases in mean failure stress and elastic modulus as compared to the other two groups (Figure 4). Specifically, the Low Flow group demonstrated statistical increases of 342% and 608% in ultimate stress compared to the control (p=0.014) and No Flow (p=0.005) groups, respectively. Partial stenosis (Low Flow) statistically increased the elastic modulus by 578% from the control group value (0.30MPa) to 1.75Mpa (p=0.004). Elastic moduli values calculated for the No Flow samples demonstrated on average, a 458% decrease in elastic modulus values when compared to the Low Flow experimental set (p=0.006). No differences were noted for ultimate (failure) strain between any of the groups. No statistical findings were observed between the No Flow and control groups for any of the material parameters calculated.

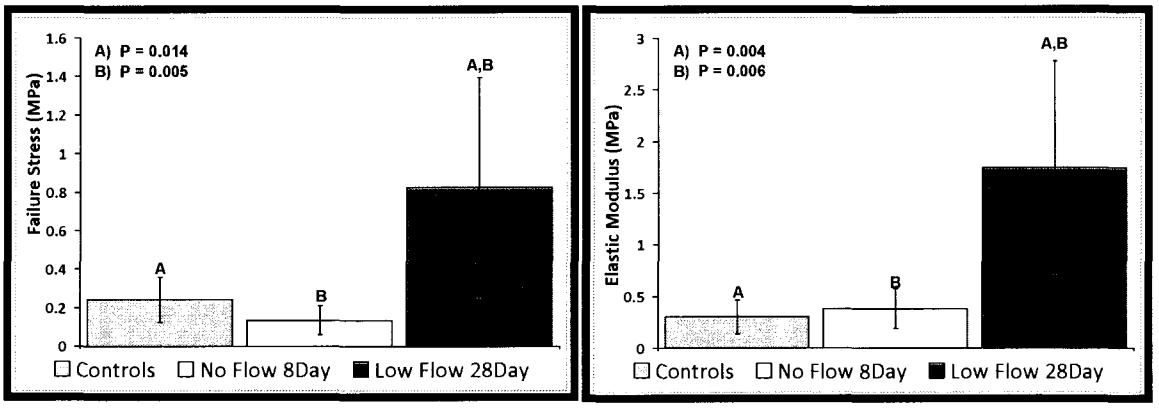

Figure 4: Failure stress (*Right*) and elastic modulus (*Left*) calculated following quasi-static ramp to failure testing. Like letters indicate statistical differences ($p<0.05$) corresponding to the given p-values. Calculated means are shown with standard deviations error bars. Statistical differences between groups were noted for failure stress and elastic modulus.

5.4 Uniaxial Tension Experiment: Discussion

Statistical analyses between the DVT-induced groups and controls indicate significant changes in the vein wall compliance, demonstrated by changes in the reciprocal of stiffness. It is of note that many of the mechanical metrics studied in this investigation were also different between the two DVT-induced groups for geometric, structural and material properties (Table 1, Figure 3, and Figure 4, respectively). The data demonstrate that complete vessel occlusion (No Flow) leads to the greatest degree of deviation in the geometric parameters of the vessel. These geometric changes are most likely reflective of a larger thrombus. Future histological efforts could confirm this hypothesis. The statistical findings demonstrate that complete ligation (No Flow) of a vessel causes increased thickness of the vessel wall and cross sectional area compared to geometric changes following partial occlusion. Interestingly, structural parameters do not follow these same trends, indicating geometric parameters are not necessarily indicators for structural changes. This is illustrated by the Low Flow group, demonstrating significant changes in failure load and stiffness, but not width and cross-sectional area. Surprisingly, the partially occluded vessels (Low Flow) had equivalent cross-sectional area to the controls, yet had the most significant increase in stiffness and elastic modulus. Increases in modulus and stiffness are indicative of a less compliant, more rigid vascular construct. The data demonstrate that partial occlusion of the IVC for seven days produces a less distensible vascular conduit. This correlates with observations observed clinically, in which palpation of PPV reveals relatively rigid vessels. Decreases in vascular flow of 80-90% inevitably lead to increased inter-luminal

pressure via significant increases in vein wall stiffness and modulus. Complete removal of vascular flow (No Flow) causes significant decrease in the dispensability of the vessel via changes in the stiffness of the vein wall. Differences between the biomechanical response parameters for the DVT-induced groups indicate that the method by which a PPV is developed is also an important factor that leads to distinct vein wall mechanics. The data demonstrate that the inherent global mechanical behavior of the vessel tissue is altered due to DVT.

6.0 Nanoindentation Experiment

6.1 Nanoindentation Experiment: Background

In order to better understand the resultant outcome of deep vein thrombosis (DVT), a technique that has significant spatial resolution must be employed to examine the biomechanical changes of the intra-wall constituents. Therefore, the purpose of this portion of the study was to quantitatively compare the structural/material changes through the use of nanoindentation between healthy and DVT-induced veins "diseased", in the three primary axes of loading: in the circumferential (perpendicular to the surface created by transecting the vein wall longitudinally), longitudinal (perpendicular to beginning/end surfaces of the isolated intact vessel segment), and luminal (perpendicular to inner surface of vessel) directions (Figure 5).

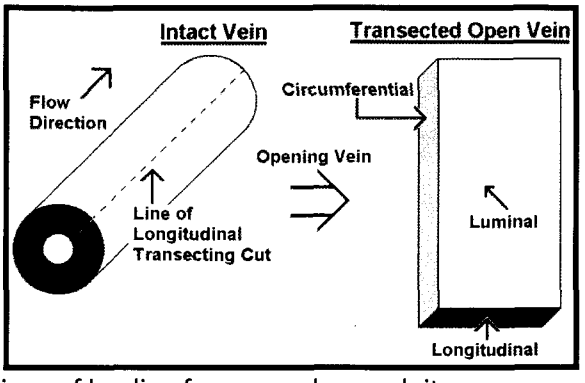

Figure 5: Primary directions of loading for a vascular conduit.

The biomechanical properties of vascular tissue on the cellular scale are difficult to evaluate through traditional mechanical testing techniques [26]. However, by using small-diameter spherical tips (approximate 100μm) and micro-scale loads (approximate 100mN) and displacements (1000nm), local measurements can be accurately performed in small tissue regions nondestructively and with high spatial resolution [25]. Nanoindentation has recently gained popularity for testing soft (elastic modulus ≈ 1MPa) biologic materials on the micrometer length scale [24-26, 32]. A number of studies have demonstrated the feasibility of using nanoindentation to elicit biomechanical properties of vascular tissue, yet, to date, few have reported quantitative values comparing healthy and diseased vascular tissue. To our knowledge, no study has examined the biomechanical properties of each of the primary loading axes (longitudinal, circumferential, and luminal) of healthy and diseased vascular tissue. An understanding of these properties, on all scales, may aid researchers in quantitatively characterizing local mechanics on the cell-to-tissue scale and could clarify relationships between tissue mechanics and pathologic response [43].

Nanoindentation involves application of a controlled load to a surface, with force applications typically ranging between 100nN and 500μN and spatial resolutions between 1nm and 30μm through the use of the nanoindenter [24]. Load-displacement data obtained during one cycle of loading and unloading can be analyzed using equations based on elastic contact theory (Hertzian contact) to quantify structural and material properties such as stiffness and reduced elastic modulus. Currently, the standard technique for analyzing nanoindentation data has been developed and validated for elastic and elastic-plastic materials. The form most often used is that presented by Oliver and Pharr [71]. The formulae are based on the classical elastic solutions by Sneddon [86], who derived general relationships among the load, displacement, and contact area for any indenter shape that can be described as a solid revolution of a smooth function [71, 86]. Sneddon demonstrated that the applied load (*P*) is related to the shear modulus of the material (μ), the radius of contact (*a*), and the penetration depth (*h*) through the following relationship:

$$P = \frac{4\mu a h}{1+\upsilon} \quad or \; P = \frac{2E\sqrt{A}h}{(1+\nu)^2\sqrt{\pi}} \qquad \textbf{Equation 3}$$

where v is the Poisson ratio of the material. The elastic modulus (E) of a material is defined as the ratio of normal engineering stress (σ) over engineering strain (ε) in the portion of the stress-strain relationship that obeys Hooke's laws. The applied load can also be formulated by recalling that the shear modulus for an isotropic material is related to the elastic modulus of a material by $E = 2\mu(1 + \nu)$, and recalling that the contact area for spherical punch is given by $A = \pi a^2$. Therefore, by taking the first derivative of the applied load with respect to the indenter penetration depth, the

unloading stiffness (S) of the substrate can be expressed as a function of the contact area (A) and steady state elastic modulus (E).

$$E = 2\mu(1 + v)$$ **Equation 4**

The contact area (A_c) between a spherical indenter tip and the substrate can be calculated as follows.

$$A_c = \pi\left(2Rh_c - {h_c}^2\right)$$ **Equation 5**

where h_c is the contact depth at the maximum load, and R is the nominal radius of the spherical indenter (Figure 6).

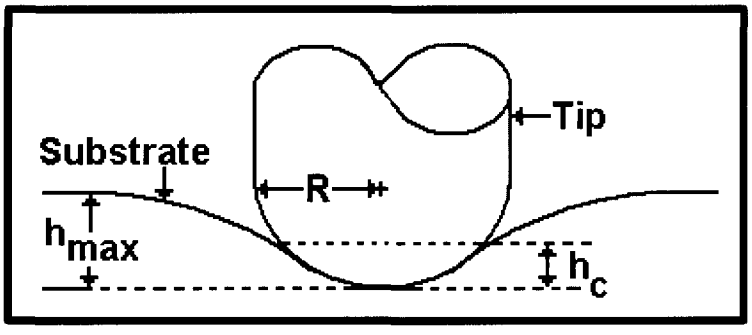

Figure 6: Schematic demonstrating the interaction between an indenter tip and the underlying substrate.

The compliance of the indenter is considered to be several orders of magnitude less than the compliance of the substrate, and thus can be ignored in the calculation of the elastic modulus. Under these assumptions, the elastic modulus, termed the "reduced modulus" (E_r), can be recast as a function of unloading stiffness and contact area (A_c):

$$E_r = \frac{S\sqrt{\pi}}{2\sqrt{A_c}}$$ **Equation 6**

It has been found empirically that both elastic and plastic deformation may occur during the loading phase, but that the unloading phase is dominated by the elastic response of the substrate material. That is, even if plastic or viscoelastic deformation occurs in the material, the instantaneous elastic response dominates the initial portion of the unloading curve [24]. Thus, calculating the reduced plastic modulus from nanoindentation data simply involves measuring the unloading stiffness and the contact depth at maximum load.

Since Oliver and Pharr first proposed the formulation for reduced modulus, several modifications and improvements have been proposed in order to account for deviations from the idealized Hertzian contact conditions. Nanoindentation of soft substrates usually involves a significant adhesive effect between the indenter tip and the sample. The two most common models used to describe the effects of adhesion on contact mechanics behavior are the Johnson, Kendall, Roberts (JKR) and Deraguin-Muller-Toporov (DMT) models [32]. For low modulus materials, the JKR model, which accounts for adhesion forces only within the expanded area of contact, is considered to give a better representation of the elastic modulus. Specifically, work by Gupta *et al* has demonstrated that adhesion plays a significant role in soft tissue contact mechanics [32]. Their work confirmed that the work of adhesion must be included in the experimental protocol and resulting calculations for determining the mechanical properties with nanoindentation [32]. The presence of adhesion between the tip and the tissue may also result in an increase in the effective contact depth [32]. According to the JKR model, the work of adhesion is related to the magnitude of the maximum

tensile pull-off adhesive force, measured during the unloading of the substrate (Figure 7). The authors of this model postulated that the thermodynamic work of adhesion per unit of contact area (W_a) is related to the pull-off adhesion force:

$$F_{pull-off}{}^{JKR} = \frac{3\pi}{2} R W_a \qquad \textbf{Equation 7}$$

Explicitly, the thermodynamic work of adhesion per unit of contact area (W_a) is the work required to separate two surfaces from finite to infinite contact. This parameter can be directly calculated from the load-displacement profile generated during nanoindentation testing. Using the JKR formulation, the elastic modulus for a spherical indenter can be expressed as:

$$E_r^{JKR} = \sqrt{\frac{S^3(1-\nu_s{}^2)^2}{6R\left[P+2F_{pull-off}{}^{JKR}+2F_{pull-off}{}^{JKR}\sqrt{\left(\frac{P}{F_{pull-off}{}^{JKR}}+1\right)}\right]}} \qquad \textbf{Equation 8}$$

where S is the unloading stiffness, R is the nominal radius of the indenter tip, and $F_{Pull\text{-}off}$ is a measure of the adhesion force generated during tip-substrate separation. The JKR model, which accounts for interfacial forces outside the Hertzian contact area, is the most applicable adhesion model for compliant material indented with spherical probes with a large radius of curvature(approximate 100μm) [32].

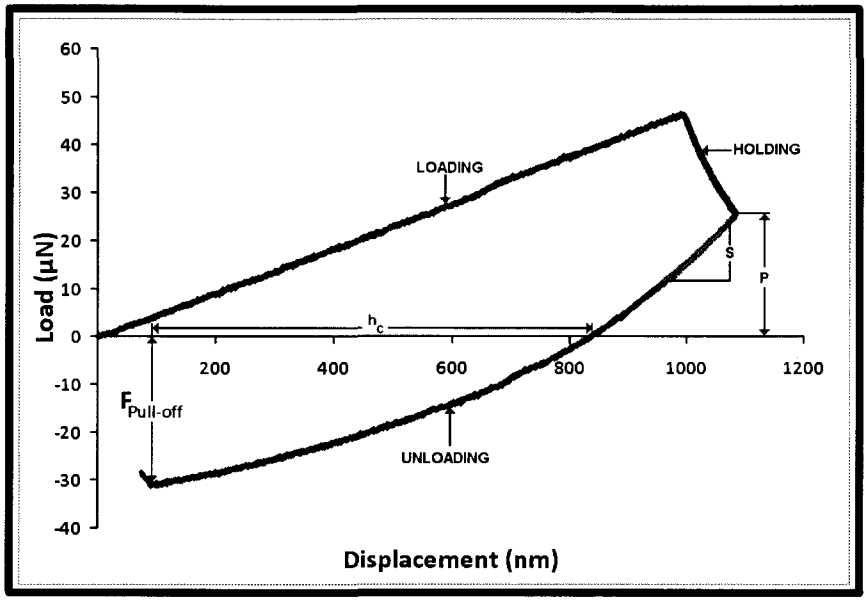

Figure 7: Typical Load-Displacement curve observed during nanoindentation testing. Biomechanical indices used in the formulation of Equations 6 and Equation 8 have been labeled.

6.2 Nanoindentation Experiment: Methods

Nanoindentation tests were performed on both healthy and DVT induced [41] ("diseased") murine inferior vena cava tissue (IVC) (n = 8 IVC/group). Diseased murine vena cava tissue samples were created by causing ligation for seven days via tightening a suture around the IVC of a mouse, invariably producing occlusive, laminar thrombi [41, 54]. Harvested IVC were transected longitudinally along the flow direction, creating a planar sheet. The thrombus was then separated from the vessel wall for the diseased group. Each planar murine sample was sectioned circumferentially into three equal samples sections. Samples were stored in cool (approximately 20ºC) isotonic saline (0.9%w/v sodium chloride) and biomechanically tested within forty-eight hours post sacrifice. Care was taken to ensure that the primary directions of physiological

loading (circumferential, longitudinal, and luminal) were "tracked" through all processing procedures for each piece of tissue (Figure 8). Prior to nanoindentation testing, the samples were mounted using previously reported techniques[24-26], which have been shown to maintain sample hydration for up to eight hours and provide adequate mechanical substrate support for testing [26] (Figure 9). To insure complete equilibrium hydration testing, samples were submerged in saline at forty-five minute intervals for a minimum of twenty minutes. Using these dissection and hydration techniques, it was possible to mount hydrated samples such that one of the six sides from each planar sheet was aligned in one of the primary directions of interest.

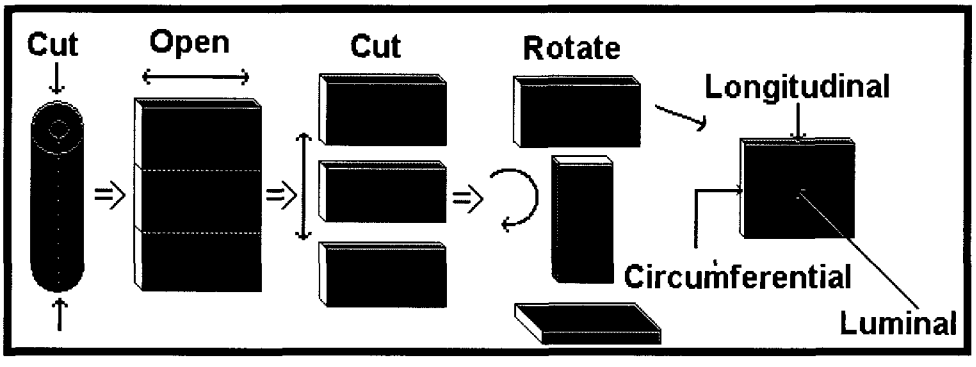

Figure 8: Schematic of IVC sample preparation for nanoindentation testing. The respective biomechanical/physiological loading directions of the vessel wall have been labeled.

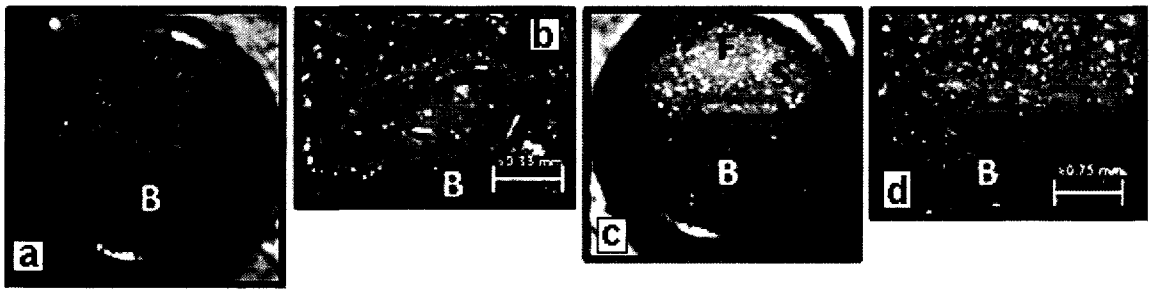

Figure 9: Murine inferior vena cava samples mounted for nanoindentation testing. Vascular samples (S) have been outlined for emphases. IVC samples were mounted against a rigid substrate (B), the tissue was surrounded by saline soaked polymeric foam (F) to insure sample hydration throughout testing. The two left photos (macro-view 'a', micro-view 'b') are of a No Flow sample mounted in the circumferential direction. The right two photos (macro-view 'c', micro-view 'd') are of a Control sample mounted in the circumferential direction.

Nanoindentation measurements were performed using a Hysitron TriboIndenter (Hysitron Inc., Minneapolis, MN) with closed loop feedback in load-controlled mode. A 100μm, 90º cone angle fluid cell nonporous diamond tip was used for all experiments. Ebenstein *et al* showed a conospherical diamond probe, with a 100μm radius of curvature was found to be suitable for testing a variety of soft hydrated materials [26]. Their work demonstrated repeatable measurement on all of the materials they tested, exhibited minimal approach problems, and had reasonable projected contact area to measure local tissue properties rather than individual cells or globally averaged tissue properties [26]. A trapezoidal loading profile was selected; once the tip was brought into contact with the sample, the load was applied at a rate of 100 μN/s, held for 10 seconds at the maximum load (400 μN) to permit viscoelastic dissipation, and subsequently withdrawn at a rate of 100 μN/s [25, 26, 32]. Because much of the applied

load goes into moving the tip at large displacements, the actual peak load felt by the samples ranged from 10–80 μN (Figure 7). A trapezoidal load function was utilized to allow creep in the substrate to dissipate prior to unloading. Load–displacement curves were corrected for large displacements and 8 μN force offsets were imposed prior to the analysis. Brisceo et al. demonstrated that this loading profile, while not long enough for creep to fully dissipate, was sufficient for the unloading behavior to dominant the inherent viscoelastic effects [7]. Load and displacement were recorded simultaneously during indentation at 228 Hz. Three parameters were reported here as measures of tissue mechanical properties: the unloading stiffness, the reduced moduli (Oliver-Pharr and JKR formulations). Because an identical load function was applied to each indenter site, the changes in the indentation response of the tissue, as quantified by these parameters, provide a measure of relative functional properties in the different tissue specimens [26]. The unloading stiffness (S), was calculated by fitting a linear slope to the initial 10% portion of the unloading curve. Reduced modulus (Oliver-Pharr and JKR formulations) were calculated from equations 6 and equation 8, respectively.

Statistical testing in the aforementioned biomechanical parameters between groups was performed using a student's t-test (SigmaStat, Systat Software Inc. Richmond, California, USA). P-values less than 0.05 were considered statistically significant. If equal variance between specific data sets failed ($p<0.005$) for a specific comparison, Mann-Whitney rank sum tests were performed, where p-values less than 0.05 were considered statistically significant.

6.3 Nanoindentation Experiment: Results

Using the JKR formulation of elastic modulus, which is considered to be the most accurate for "soft" biomaterials, the data indicate that the mean elastic moduli of healthy murine IVC ranges from 238.1 kPa in the luminal direction to 362.6 kPa in the circumferential direction. The mean elastic modulus in the longitudinal direction was 270.5 kPa. The DVT-induced samples had mean elastic moduli of 340.5 kPa in the luminal direction, 397.3 kPa in the circumferential direction, and 381.1 kPa in the longitudinal direction.

No statistically significant differences between the healthy and diseased tissue was found for the unloading stiffness parameters in the three orthogonal directions. However, statistical differences were observed intra-group (Table 2). The longitudinal unloading stiffness of the healthy tissue demonstrated a statistical increase of 43.6% and 62.5% as compared to the circumferential and luminal directions, respectively (Figure 10). Similarly the diseased tissue showed a statistically significant increase in the unloading stiffness in the longitudinal direction of 40.5% and 62.2% when compared to the circumferential and luminal direction, respectively (Figure 10).

All reduced elastic moduli calculations were statistically different ($p<0.05$) from the corresponding JKR elastic moduli calculations, for the three primary directions of interest. No statistically significant moduli findings were noted between the healthy and diseased tissue in the circumferential direction (Table 3). The circumferential direction did demonstrate a non-significant increase of 9.51% between the healthy and

diseased tissue for the JKR elastic modulus formulation. The longitudinal reduced elastic modulus was statically greater (111.8%) for the diseased tissue as compared to the healthy tissue (Table 3, Figure 11). The longitudinal JKR elastic modulus for the diseased tissue was not statistically different than that of the healthy tissue; however, an increase of 40.9% was calculated for the diseased tissue. The luminal JKR elastic modulus was statistically greater (43%) for the diseased tissue compared to the healthy tissue (Table 3, Figure 12).

Unloading Stiffness (μN/nm)

	Circumferential	Longitudinal	Luminal
Healthy	0.0275 ± 0.0120 A (A) p=0.340	0.0440 ± 0.0127 B (B) p=0.117	0.0192 ± 0.0080 C (C) p=0.736
Diseased	0.0319 ± 0.0024 A	0.0513 ± 0.0099 B	0.0208 ± 0.0049 C

In Healthy:	***In Diseased:***
Circumferential ≥ Longitudinal p = 0.002	Circumferential ≥ Longitudinal p = 0.001
Luminal ≥ Longitudinal p = 0.001	Luminal ≥ Longitudinal p = 0.001

Table 2: Unloading stiffness formulations in the circumferential, longitudinal, and luminal directions based on nanoindentation data for healthy and diseased (induced with deep vein thrombosis) groups. Calculated means are shown with (±) one standard deviation. Similar letters correspond to the given p-values.

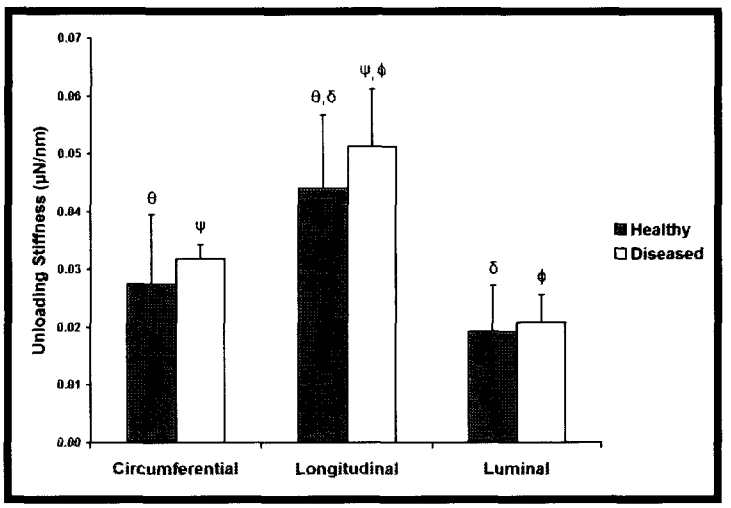

Figure 10: Unloading stiffness calculated from nanoindentation data in the three primary axes of loading. Averages are shown with one standard deviation error bars, with similar letters indicating statistical differences. Statistically significant p-values are as follows: (θ) p =0.002, (ψ) p < 0.001, (δ) p < 0.001, (ϕ) p < 0.001.

CIRCUMFERENTIAL PARAMATERS

	Reduced Elastic Modulus (MPa)		Elastic Modulus JKR (MPa)	
Healthy	0.6108 ± 0.1819 [A]	(A) p = 0.583	0.3626 ± 0.1207 [B]	(B) p = 0.579
Diseased	0.6455 ± 0.1132 [A]		0.3973 ± 0.0424 [B]	

LONGITUDINAL PARAMATERS

	Reduced Elastic Modulus (MPa)		Elastic Modulus JKR (MPa)	
Healthy	0.4558 ± 0.0222 [C]	(C) p < 0.001	0.2705 ± 0.0153 [D]	(D) p = 0.201
Diseased	0.9654 ± 0.3243 [C]		0.3811 ± 0.0902 [D]	

LUMINAL PARAMATERS

	Reduced Elastic Modulus (MPa)		Elastic Modulus JKR (MPa)	
Healthy	0.4651 ± 0.1007 [E]	(E) p = 0.086	0.2381 ± 0.0461 [F]	(F) p = 0.024
Diseased	0.5412 ± 0.0985 [E]		0.3406 ± 0.0854 [F]	

NOTE: ALL Reduced Elastic Modulus calculations where statically different from the corresponding JKR Elastic Modulus calculations p < 0.05.

Table 3: Elastic modulus formulations (Reduced and JKR) in the circumferential, longitudinal, and luminal directions based on nanoindentation data for healthy and diseased (induced with deep vein thrombosis) groups. Calculated means are shown with (±) one standard deviation. Similar letters correspond to the given p-values.

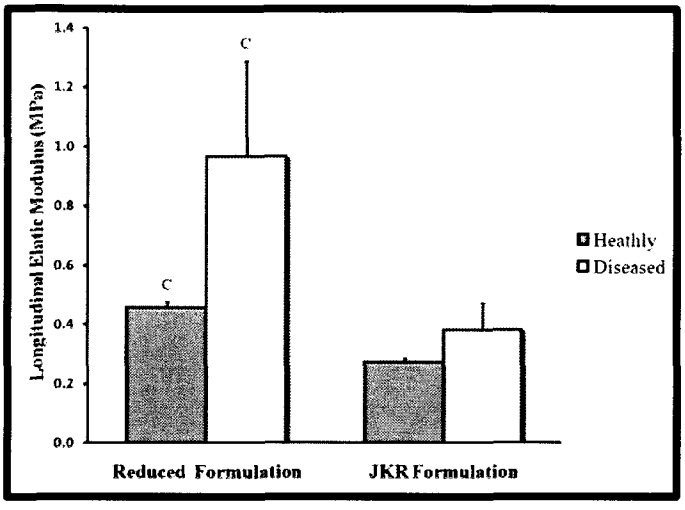

Figure 11: Elastic moduli (Reduced and JKR formulations) calculated from nanoindentation data in the longitudinal axes of loading. Averages are shown with one standard deviation error bars, with similar letters indicating statistical differences. Statistically significant p-values are as follows: (C) $p < 0.001$.

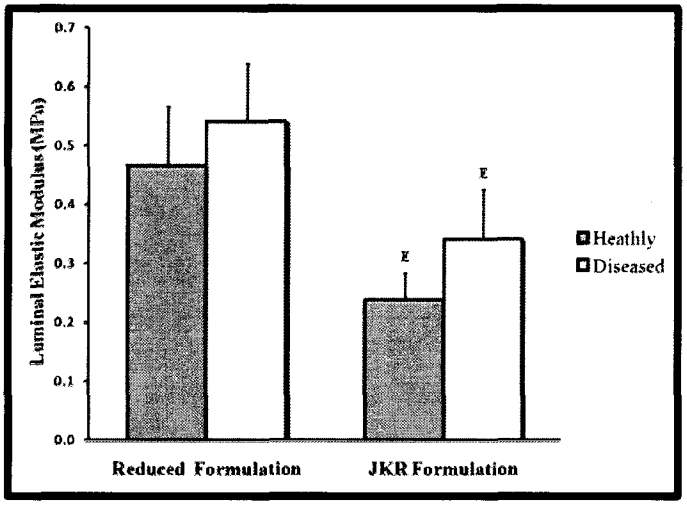

Figure 12: Elastic moduli (Reduced and JKR formulations) calculated from nanoindentation data in the luminal axis of loading. Averages are shown with one standard deviation error bars, with similar letters indicating statistical differences.

6.4 Nanoindentation Experiment: Discussion

The data indicated that the longitudinal unloading stiffness was statistically greater than the circumferential or luminal responses. This could possibly be correlated to the physiologic *in vivo* response of the tissue, were the tissue is generally under circumferential stress rather than longitudinal or luminal stresses. It is hypothesized by our group that increased stiffness in the longitudinal direction in a 3D loading case is important in maintaining physiologic homeostasis and can be directly correlated to collagen and elastin fiber alignment within the tissue. Future finite element and histological work by our lab will address this hypothesis.

The only statistical difference from normal, healthy baseline data based on the JKR elastic modulus formulation was noted in the luminal direction. This correlates with previously published data examining only the luminal surface of vascular tissue [24, 26]. Surprisingly, no statistical changes where observed in the circumferential and longitudinal direction. Clinically, increases in intra-luminal pressure following DVT are associated with a reduced capability of the vessel to distend [23]. The DVT model used here has previously demonstrated strong histologic correlation to clinically recovered DVT veins [41]. The data presented seems to indicate that even non-statistical changes in the circumferential and longitudinal response parameter coupled with statistical changes only in the luminal direction can have a large affect on the response of the tissue (and the entire venous system).

This experiment does contain some inherent assumptions about loading anisotropy. Nanoindentation is a compressive testing process. This type of testing does not explicitly mimic the physiologic *in vivo* loads expected. However, nanoindentation does give insight into general comparisons of the biomechanical response of the tissue. The assumption used for this analysis is that the relationships between the compressive load histories can be applied to the more physiologically relevant tensile loading history. This is to say that the compressive-tensile anisotropy is known to exist *in vivo*, however in order to make conclusions based on the presented nanoindentation data the underlying assumption is that the *in vivo* tensile response of the tissue due to DVT is altered in a manner that is similar to our compressive indentation data.

7.0 Biaxial Stretch Experiment

7.1 Biaxial Stretch Experiment: Background

A thorough understanding of the anisotropic, non-linear, and viscoelastic mechanical properties of both healthy and diseased IVC is clearly required to characterize the *in vivo* functional performance of the tissue. The mechanical properties of veins exhibit a strong variability in their respective biomechanical response [2]. Experimental procedures such as inflation tests [62, 99], biaxial tests [79, 80, 82], and simple tension tests [5] have been used to determine the mechanical properties of venous tissue [2]. Those experiments as well as the research presented within this study reveal that the passive behavior of venous tissue is highly non-linear and anisotropic under elastic finite strains, which is usually modeled within the framework of hyperelasticity.

The predictive and modeling applications of the vessel's functional biomechanical performance require an appropriate constitutive model. Constitutive modeling allows quantitative predictions of the biomechanical behavior of the tissue under any loading state. To achieve this goal, rigorous experimentation using physiological deformation states, including planar biaxial stretch, were performed in order to obtain material constants and to evaluate the model's predictive ability. Vascular tissue is assumed incompressible, and thus planar biaxial testing generates a two-dimensional (2-D) stress-state that could be used to fully characterize the three-dimensional (3-D) mechanical properties of the tissue [82]. Therefore, biaxial stretch testing was used to determine the biomechanical performance of the tissue.

Biaxial experiments of soft biological tissues are generally difficult to perform and present challenges unique to biological tissue. Some of these experimental issues include small specimen sizes, structural and compositional heterogeneity, difficulty in gripping (without causing damage), localized effects of different gripping techniques (St. Venant-like effects), difficulty in precisely identifying material axes, difficulty in assuring constant forces along specimen edges, and large specimen-to-specimen variability [82].

In general, biaxial testing devices have to be much more complex than standard uniaxial testing devices because of the need to independently control two boundary conditions. Also, to simplify data analysis, the edges must be free to expand in the lateral direction, and the central target region stress-strain distribution should be uniform. The target region is remote from the outer edges of the sample to avoid edge

effects due to tethering. Non-contact optical data from the target region allows for the planar calculation of tissue strain in the axes of loading.

In addition to determining the biomechanical effects secondary to DVT, biaxial stretch experiment were also designed to assess the effects of metalloproteinase-9 on thrombus resolution Proteins of the matrix metalloproteinase (MMP) family are involved in the breakdown of extracellular matrix in normal physiological processes, including tissue remodeling, as well as in disease processes, such as DVT. These highly regulated enzymes mediate the remodeling of the extracellular matrix (ECM) [35]. MMPs are known to be active in wound healing and tissue regeneration as well as in diseases that feature prominent vascular remodeling, notably atherosclerosis and aneurismal disease [35]. Further, it has been shown that MMP activity is modulated in the presence of serine proteases, notably, plasmin. This may be especially important in DVT resolution, as plasmin is the prime mediator of fibrinolysis [35]. Vein wall remodeling after DVT is associated with increased early MMP-9 expression and activity after DVT resolution. The sham and ligation groups (both WT and KO) have been previously described [17, 41,Henke, 2004 #183]. Briefly, for the Ligation groups (both WT and KO) the IVC was dissected from the adjacent section of aorta, and all visible side and back branches distal to the renal veins and proximal to the iliac bifurcation were ligated. The IVC was then ligated immediately distal to the renal veins.

7.2 Biaxial Stretch Experiment: Methods

A custom built biaxial mechanical testing device was used to perform these experiments (Figure 13). The biaxial testing device was similar in design and functionality to the devices described in previous studies [81, 82]. Two pairs of independent, orthogonally-positioned, computer-controlled linear actuators (0.05μm linear resolution; Soloist, Aerotech USA and Zaber Technologies, British Columbia, Canada) applied linear displacements to planar sections of venous tissue, while two independent in-line load cells (0.01 gram resolution, Sensotec, Ohio) measured the resultant forces along their respective loading directions (i.e. Axial and Circumferential). Both load and displacement data were simultaneously collected at 1000Hz, then reduced to 15Hz to sync with the associated strain data.

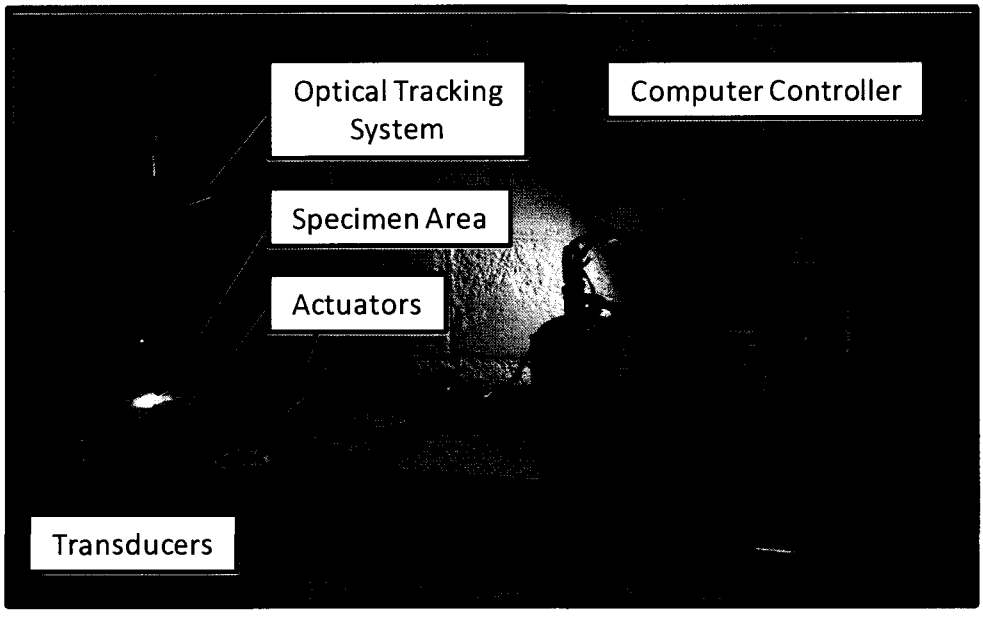

Figure 13: Biaxial stretch experiments testing apparatus.

Specimens were mounted to the biaxial device in a trampoline-like fashion by passing two thin threads per side (7-0 suture, 0.03mm diameter) through the sample, allowing the edges to expand freely in the lateral directions (Figure 14). The longitudinal/axial direction (AD) and circumferential direction (CD) of the specimen where aligned with the x_1 and x_2 stretch axes of the testing device, respectively. The local longitudinal direction of the biaxial specimen was designated as being parallel to the luminal blood flow [94].

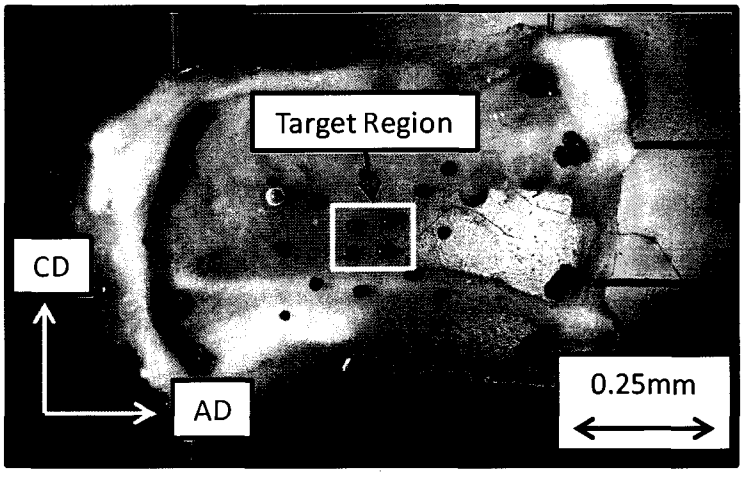

Figure 14: Specimen (planar sheet of vein wall) mounted in trampoline like fashion for biaxial stretch experiments. The primary directions of loading, circumferential (CD) and axial (AD) (i.e. longitudinal or flow direction) have been highlighted.

Low friction pulleys attached to the motion carriages of the linear actuators insured equal tension on each suture line. This design eliminated the use of individual actuators and force transducers for each suture line, as well the need for adjustment of individual suture line tensions [79]. Testing was performed with the specimen completely immersed in phosphate-buffered saline at room temperature.

Localized tissue deformations were measured by monitoring the in-plane motion of four contrast marks placed on the sample that formed square target region in the center of the specimen (Figure 14). Using standard macro-filming techniques with lenses and bellows, digital video with a spatial resolution of approximately 2.5μm/pixel was recorded at 15Hz to determine the tissue strains throughout the biaxial loading protocols. Following testing, the non-contact video data was decompiled into individual frames (15 frames per second of testing). Position data for each marker was extracted from each frame using a custom-written video marker-tracking algorithm. This program (Visual Basic, Microsoft) utilized manual selection of the contrast marks from the first video frame to establish initial marker positions and threshold limits. Thresholding of the contrast markers allowed the program to delineate the boundary between the low intensity dark markers and the high intensity white background. Following marker selection, the custom executable algorithm calculated the geometric centroid of each individual marker based on threshold levels and marker geometry, writing the absolute marker position to a file. The program automatically advanced to the next frame and, using the previous centroid locations, calculated the new position of the centroid. Marker locations in the reference state were determined with the specimens in the initial unloaded or stress-free configuration state while immersed in the saline bath just prior to the start of testing. This procedure produced smooth positional data (Figure 15).

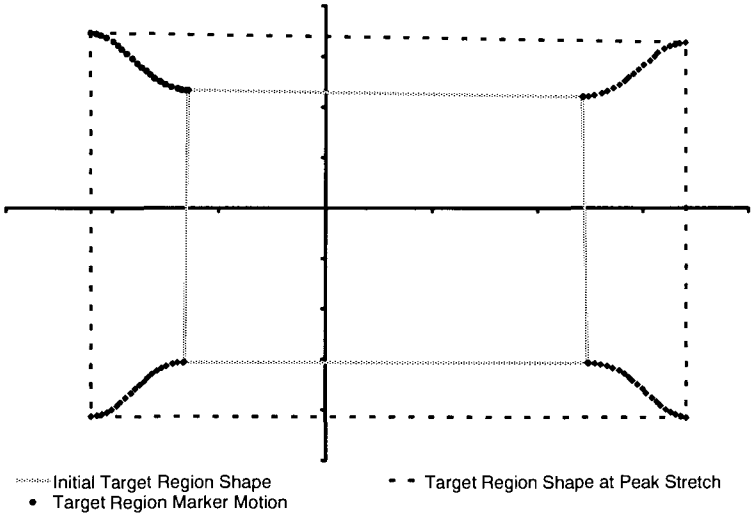

Figure 15: Example target region position data *pre* and *post* equal biaxial stretch loading. Marker displacements were used to calculate the axial and circumferential stretch values during testing.

The in-plane Green's strain components, E_{FD} and E_{CD}, along the flow and circumferential directions, respectively were computed from the contrast markers' displacements using a four-node finite element technique [40]. For this technique the in-plane deformation gradient tensor F_{ij} was computed from the non-contact optical marker data for each datum load point, where the physical components of the deformation gradient tensor F_{ij} are

$$F_{ij} = \begin{bmatrix} \lambda_1 & \kappa_1 \\ \kappa_2 & \lambda_2 \end{bmatrix} \qquad \textbf{Equation 9}$$

where λ_i and κ_i represent the stretch ratios and the shear ratios, respectively. These relationships are derived from the homogeneous biaxial deformation:

$$x_1 = \lambda_1 X_1 + \kappa_1 X_2 \qquad \textbf{Equation 10}$$

$$x_2 = \lambda_2 X_2 + \kappa_2 X_1 \qquad \textbf{Equation 11}$$

$$x_3 = \lambda_3 X_3 \qquad \textbf{Equation 12}$$

where x_i and X_i are the location of the contrast markers in the unstressed and stressed states, respectively. It is important to note that in the target region the stress-strain field is assumed to be homogenous, and thus, the components of F_{ij} are independent of position. Also, vascular tissue is generally considered to be incompressible such that that λ_3 is calculated by setting the determinate of the deformation gradient tensor equal to unity. Therefore, the components of the in-plane Green strain tensor, E_{ij}, are calculated as:

$$E_{11} = E_{CD} = \frac{1}{2}\left(\lambda_1^2 + \kappa_1^2 - 1\right) \qquad \textbf{Equation 13}$$

$$E_{12} = E_{CD\_FD} = \frac{1}{2}(\lambda_1 \kappa_1 + \lambda_2 \kappa_2) \qquad \textbf{Equation 14}$$

Lagrangian stresses (load per unit of the stress free cross-sectional area) were computed along the primary directions of loading (flow and circumferential). This analysis assumes that the samples can be treated as an orthotropic, hyperelastic material following the behavior according to the theory of pseudoelasticity [29]. The stress components, T_{ij}, were computed from the measured axial forces, F and the initial geometric parameters:

$$T_{ij} = \begin{bmatrix} \frac{F_1}{tL_2} & 0 \\ 0 & \frac{F_2}{tL_1} \end{bmatrix} \qquad \textbf{Equation 15}$$

where t is the specimen thickness and L_i are the specimen lengths. In this formulation the subscripts connection follows that $\mathbf{T_{11} = T_{CD}}$ **and** $\mathbf{T_{22} = T_{FD}}$. The stresses were converted to second-order Piola-Kirchoff stresses according to the relationships,

$$S_{FD} = \frac{T_{FD}}{\lambda_{FD}} \qquad \textbf{Equation 16}$$

$$S_{CD} = \frac{T_{CD}}{\lambda_{CD}} \qquad \textbf{Equation 17}$$

where λ denotes the stretch ratio, which is related to the respective Green strain (E_{ij}) by $\lambda = \sqrt{1 + 2E}$. The Cauchy stress, t_{ij}, can be determined from the Lagrangian stresses, T_{ij}, and the deformation gradient tensor, F_{ij}:

$$t_{ij} = \begin{bmatrix} \lambda_1 T_{11} & \kappa_1 T_{22} \\ \kappa_2 T_{11} & \lambda_2 T_{22} \end{bmatrix} \qquad \textbf{Equation 18}$$

Specimen thickness, width, and length were measured from high resolution (8M pixel, PowerShot S80, Canon, Lake Success, NY, USA) digital images taken from multiple perspectives. All images were captured at room temperature, with the specimen completely submerged in saline. Image data were used to determine the specimen's dimensions, which were required for *post-hoc* transformation of the load-displacement data into the stress-strain space. Sample thickness, width, and length were determined by taking length measurements at five equally-spaced locations along the vessel using imaging software (ImageJ 1.38x, National Institutes of Health, Bethesda, MD). This technique produced less than a one percent error in measured values, with a resolution of approximately 2.5μm per pixel.

The testing protocol consisted of normal strain component-controlled biaxial testing where the ratio of $E_{\text{Flow (i.e. Axial) Direction (FD)}}$: $E_{\text{Circumferential Direction (CD)}}$ was kept constant [81, 82, 90, 93, 94]. A preload of 0.1g was applied quasi-statically to each specimen to ensure that the biaxial specimen was planar prior to the start of the biaxial protocols. Specimens were preconditioned with 20 cycles of equilbiaxial stretch

(E_{FD}:E_{CD}=1:1) to a maximum strain level of 10% at a strain rate of 0.05 sec^{-1}. In order to characterize the mechanical properties over a wide range of the strain space a sufficient data density for constitutive modeling is needed. Therefore, each specimen was subjected to four different test protocols where the ratio of E_{FD}:E_{CD} was kept constant [81]. Specifically, following preconditioning four cycle testing protocols were performed: E_{FD}:E_{CD}=1:1, 1:2, 0:1, 1:0. Equal-biaxial testing (E_{FD}:E_{CD}=1:1) was performed throughout testing to ensure that no structural damage occurred as a result of the biomechanical testing [94]. The two constant stretch tests (E_{FD}:E_{CD}=0:1 and E_{FD}:E_{CD}=1:0) were used to check the predictive capability of the constitutive model. Samples were cycled for twenty cycles for each loading protocol, where data from the 20^{th} cycle was used for analysis and coefficient parameterization.

Hyperelastic materials are described in terms of a strain energy potential which defines the strain energy stored in the material per unit of the reference volume (volume in the initial configuration) as a function of the deformation at the point in the material. The anisotropic hyperelastic material model provides a general capability for modeling materials that exhibit highly anisotropic and nonlinear elastic behavior, such as vascular tissue. These types of materials exhibit highly anisotropic and nonlinear elastic behavior due to rearrangements in the microstructure, such as reorientation of the fiber directions with deformation. Of the two distinct formulations that can be used for the representation of the strain energy potential of anisotropic hyperelastic materials, this work focuses on the invariant based approach. The strain energy function can be expressed directly in terms of the invariants of the deformations tensor

and the fiber directions. Specifically, the invariant-based energy function selected for this study was the form proposed by Holzapfel, Gasser, and Ogden [38]. This form is micromechanically based as compared to other hyperelastic strain energy functions that are purely phenomenological (e.g. the Fung form). Ogden *et al.*'s form of the strain energy potential was proposed for modeling arterial layers with distributed collagen fiber orientations [31, 38] and can be expressed as:

$$U = C_{10}(\bar{I}_1 - 3) + \frac{1}{D}\left(\frac{(J^{el})^2 - 1}{2} - \ln J^{el}\right) + \frac{k_1}{2k_2}\sum_{\alpha=1}^{N}\left\{e^{k_2\langle\bar{E}_\alpha\rangle^2}\right\} \quad \textbf{Equation 19}$$

with

$$\bar{E}_\alpha \stackrel{\text{def}}{=} \kappa(\bar{I}_1 - 3) + (1 - 3\kappa)\left(\bar{I}_{4(\alpha\alpha)} - 1\right) \quad \textbf{Equation 20}$$

where U is the strain energy per unit of reference volume; C_{10}, D, k_1, k_2, and κ are material parameters; N is the number of families of fibers; and $\bar{I}_1$ is the first invariant of the deformation gradient; J^{el} is the elastic volume ration; and $\bar{I}_{4(\alpha\alpha)}$ are the pseudo-invariants of the deformation gradient. The second term in Equation 20, including the material parameter D and J^{el} is assumed to be zero for this analysis to force the incompressibility constraint. Therefore, for the specific case where there are two families of fibers (as is the case for this analysis), the strain energy function can be expressed in terms of the strain invariants as:

$$\psi(\bar{I}_1, \bar{I}_4, \bar{I}_6) = C_{10}(\bar{I}_1 - 3) + \frac{k_1}{2k_2}\sum_{\alpha=1}^{2}\left[e^{k_2\left[\kappa(\bar{I}_1 - 3) + (1-3\kappa)\left(\bar{I}_\beta - 1\right)^2\right]}\right];\ \beta = 4,6$$

Equation21

where k_1, k_2, and κ are material parameters (k_1 has dimensions of stress, k_2, and κ are dimensionless structural parameters). The first term in the expression of the strain

energy function (ψ) represents the distortional and volumetric contributions of the non-collagenous isotropic ground material, where C_{10} is a material property with dimensions of stress. The second term represents the contributions from the different families of collagen/elastin fibers, taking into account the effects of fiber dispersion (κ). The kappa parameter ($0 \leq \kappa \leq 1/3$) describes the level of dispersion in the fiber directions. When $\kappa = 0$, the fibers are perfectly aligned (no dispersion) whereas when $\kappa = 1/3$ the fibers are randomly distributed and the material becomes isotropic. The model assumes that the directions of the collagen/elastin fibers (γ) within each family are dispersed (with rotational symmetry) about a mean preferred direction. It is also assumed that all families of fibers have the same mechanical properties and the same dispersion, and thus the fourth and sixth strain invariant are considered equivalent. A basic assumption of the model is that the collagen/elastin fibers can support only tension, since they would buckle under compressive loading. Thus, the anisotropic contribution in the strain energy function appears only when the strain of the fibers is positive. An appropriate choice of k_1 and k_2 enables the histologically-based assumption that the collage/elastin fibers do not influence the mechanical response of the vessel wall in the low pressure domain to be modeled [38]. Under these assumptions of incompressibility and negligible shear stress the strain invariants are directly calculated from the stretch values as:

$$\bar{I}_1 = \lambda_{axial}^2 + \lambda_{circumferential}^2 + \left(\lambda_{axial}\lambda_{circumferential}\right)^{-2} \quad \textbf{Equation 22}$$

$$\bar{I}_4 = \bar{I}_6 = \lambda_{axial}^2 \sin^2(\gamma) + \lambda_{circumferential}^2 \cos^2(\gamma) \quad \textbf{Equation 23}$$

where γ is a structural parameter denoting the angle between the circumferential and mean orientation of the fiber families. Shear stretch measurement were not included in the calculations of the strain invariants because experimentally measured values for shear stretch were several orders of magnitude below the primary (axial) stretch values, failing within the limit of experimental accuracy. It was determined that shear stretch values introduced experimental noise in the *post-hoc* calculations without adding appreciable accuracy, and thus, were ignored.

Since, the strain energy function (ψ) is based on strain invariants, we may regard ψ as a function off the principal stretches λ_α, α=1 (circumferential), α=2 (axial / flow). Consequently, the principal Cauchy stresses σ_α, α=1 (circumferential), α=2 (axial / flow) simply result from:

$$\sigma_\alpha = J^{-1}\lambda_\alpha \frac{\partial}{\partial \lambda_\alpha} \psi(\bar{I}_1, \bar{I}_4, \bar{I}_6) = \lambda_\alpha \frac{\partial}{\partial \lambda_\alpha} \psi(\bar{I}_1, \bar{I}_4, \bar{I}_6) \; with \; \alpha = 1,2 \quad \textbf{Equation 24}$$

A complete derivation of the partial derivatives of the strain energy function as a function of the strain invariants and the stretch ratios is given in Appendix A.

The optically measured stretch data from the E_{FD}:E_{CD}=1:1, 1:2 experimental protocols and the corresponding Cauchy stress data for each sample was simultaneously fit to the above constitutive relation using a Levenberg-Marquardt nonlinear curve-fitting algorithm (MATLab, MathWorks, Natick, MA). This nonlinear regression algorithm uses iterative convergence to find the coefficients of the independent variables that give the "best fit" between the material model equation (e.g. strain energy function) and the experimentally measured data. This algorithm uses a functional scheme that minimizes the sum of the squared differences between the

values of the observed and predicted values of the dependent variable [53]. This iterative process begins with an initial "guess" at the independent parameter(s), checking to see how well the equation fits the input data, continuing until the differences between the residual sum of squares converges (minimia).

Fiber dispersion, the parameter kappa (κ) and the structural parameter γ, which denotes the angle between the circumferential and mean orientation of the fiber families, where not determined by the Levenberg-Marquardt nonlinear curve-fitting algorithm. These parameters were manually varied over a range of discrete values: kappa was parameterized in the range $0/18 \leq \kappa \leq 6/18$ at 1/18 increments and gamma was parameterized in the range $0 \text{ deg} \leq \gamma \leq 45 \text{ deg}$ at 15 degree increments. The parameters k_1, k_2, and C_{10} were recorded from the curve fitting algorithm when the maximum residual value between the experimental and strain energy-based Cauchy stresses matrices were at a minimum over the range of kappa and gamma.

Five experimental groups were tested: 1) CD1-Non-operated, 2) MMP-9 Knock Out (KO) Sham, 3) MMP-9 KO Ligation, 4) MMP-9 Wild Type (WT) Sham, 5) MMP-9 WT Ligation. The CD1-Non-operated group came from CD1 mice, the most common general multipurpose murine model, which served as the control group for this study. The MMP-9 Wild Type (WT) groups included mice which were bred as the precursor to the MMP-9 Knock Out (KO) model, most commonly use to study the expression and effects of matrix metalloproteinase (MMP). The MMP-9 KO murine model was bred with a disruption of the MMP-9 gene, in which the matrix metallopeptidase 9 is not expressed. Both WT and KO sham groups were subjected to the same preparation, including

dissection and mobilization of the IVC, however a ligature was not placed on the IVC nor were any side branches ligated. A more detailed description of the surgical procedure is given above.

In order to delineate statistical significance, a student's t-test analysis of variance was performed. In cases where normality failed, a Mann-Whitney Rank Sum test analysis of variance was performed. These analyses were performed on the coefficients determined to best fit the strain energy function calculated for each sample in each group (Sigma Stat 3.1, Ashburn, VA). A p-value of less than 0.05 was considered to be significant.

7.2 Biaxial Stretch Experiment: Results

The identified material parameters, based on the nonlinear curve fit of the strain energy function, are reported in the Tables 4 - 8 and Figure 16 - 17. Statistical summary of significant differences between groups are highlighted in Figure 16, and listed in Table 9.

CD1 Non-Operated Group Coefficients					
Specimen	**C_{10}**	**k_1**	**k_2**	**θ (deg)**	**γ**
CD1-Non-OP I	0.0361	0.2598	0.4124	30.00	0.2778
CD1-Non-OP II	0.0098	0.3524	0.7649	0.00	0.1667
CD1-Non-OP III	0.0483	0.2004	1.1520	0.00	0.0000
CD1-Non-OP IV	0.0189	0.1867	0.8991	15.00	0.0556
CD1-Non-OP V	0.0389	0.2403	0.3380	0.00	0.1667
CD1-Non-OP VI	0.0140	0.1981	0.1950	0.00	0.1111
CD1-Non-OP VII	0.0163	0.1787	0.0780	15.00	0.1667
CD1-Non-OP VIII	0.0047	0.0646	0.3881	15.00	0.0556
CD1-Non-OP IX	0.0084	0.0581	0.3892	0.00	0.1667
Average	0.0217	0.1932	0.5130	8.33	0.1296
SD	0.0155	0.0916	0.3505	10.90	0.0833

Table 4: Material parameters identified from fitting experimental data to the strain energy function (SEF). The coefficients C_{10} and k_1 have the stress dimensions (MPa). The coefficients k_2 and γ are dimensionless parameters. Samples were individually fit to the SEF, the averaged coefficients served as the input parameters needed to model the materials biomechanical response of the material.

MMP9 KO Sham Group Coefficients					
Specimen	**C_{10}**	**k_1**	**k_2**	**θ (deg)**	**γ**
MMP9 KO Sham I	0.1296	0.1721	0.8689	0.00	0.0556
MMP9 KO Sham II	0.1427	0.0956	1.4668	0.00	0.1111
MMP9 KO Sham III	0.1104	0.0630	1.4809	0.00	0.1111
MMP9 KO Sham IV	0.0441	0.1087	0.6777	0.00	0.0556
MMP9 KO Sham V	0.0515	0.1106	0.2931	0.00	0.0556
MMP9 KO Sham VI	0.0442	0.1050	0.3047	0.00	0.0556
MMP9 KO Sham VII	0.0490	0.1032	0.3102	0.00	0.0556
MMP9 KO Sham VIII	0.0288	0.0656	0.2596	0.00	0.2222
Average	0.0750	0.1030	0.7077	0.00	0.0903
SD	0.0449	0.0336	0.5202	0.00	0.0589

Table 5: Material parameters identified from fitting experimental data to the strain energy function (SEF). The coefficients C_{10} and k_1 have the stress dimensions (MPa). The coefficients k_2 and γ are dimensionless parameters. Samples were individually fit to the SEF, the averaged coefficients served as the input parameters needed to model the materials biomechanical response of the material.

MMP9 KO Ligation Group Coefficients					
Specimen	**C_{10}**	**k_1**	**k_2**	**θ (deg)**	**γ**
MMP9 KO Ligation I	0.0341	0.3608	0.0100	0.00	0.1111
MMP9 KO Ligation II	0.0458	0.2056	0.1159	0.00	0.0556
MMP9 KO Ligation III	0.0281	0.2152	0.3538	15.00	0.1111
MMP9 KO Ligation IV	0.1721	0.1085	1.6320	0.00	0.0556
MMP9 KO Ligation V	0.0785	0.3102	1.4492	0.00	0.1667
MMP9 KO Ligation VI	0.0551	0.3270	1.6125	0.00	0.1667
MMP9 KO Ligation VII	0.1197	0.1771	1.4838	0.00	0.1111
MMP9 KO Ligation IX	0.1284	1.1674	0.1965	0.00	0.1111
MMP9 KO Ligation X	0.0564	1.2839	0.0849	0.00	0.1667
MMP9 KO Ligation XI	0.1140	0.7010	0.1138	0.00	0.0556
MMP9 KO Ligation XII	0.2517	0.8944	0.0510	15.00	0.0556
Average	0.0985	0.5228	0.6458	2.7273	0.1061
SD	0.0681	0.4196	0.7196	6.0678	0.0462

Table 6: Material parameters identified from fitting experimental data to the strain energy function (SEF). The coefficients C_{10} and k_1 have the stress dimensions (MPa). The coefficients k_2 and γ are dimensionless parameters. Samples were individually fit to the SEF, the averaged coefficients served as the input parameters needed to model the materials biomechanical response of the material.

MMP9 WT Sham Group Coefficients					
Specimen	**C_{10}**	**k_1**	**k_2**	**θ (deg)**	**γ**
MMP9 WT Sham I	0.1001	0.3671	0.4739	15.00	0.1111
MMP9 WT Sham II	0.1672	0.1841	1.6975	15.00	0.1111
MMP9 WT Sham III	0.1018	0.1964	1.5241	0.00	0.1667
MMP9 WT Sham IV	0.0507	0.0745	1.0432	0.00	0.0556
MMP9 WT Sham V	0.1257	0.0929	0.4203	0.00	0.0000
MMP9 WT Sham VI	0.0652	0.1012	0.6131	0.00	0.0556
MMP9 WT Sham VII	0.0304	0.2976	0.6764	0.00	0.1111
MMP9 WT Sham VIII	0.5130	0.9470	0.2621	0.00	0.1667
Average	0.1443	0.2826	0.8388	3.75	0.0972
SD	0.1552	0.2874	0.5301	6.94	0.0575

Table 7: Material parameters identified from fitting experimental data to the strain energy function (SEF). The coefficients C_{10} and k_1 have the stress dimensions (MPa). The coefficients k_2 and γ are dimensionless parameters. Samples were individually fit to the SEF, the averaged coefficients served as the input parameters needed to model the materials biomechanical response of the material.

MMP9 WT Ligation Group Coefficients					
Specimen	**C_{10}**	**k_1**	**k_2**	**θ (deg)**	**γ**
MMP9 WT Ligation I	0.3326	0.9655	0.3471	0.00	0.0000
MMP9 WT Ligation II	0.5377	0.1210	1.9975	0.00	0.0000
MMP9 WT Ligation III	0.1850	1.1610	1.4272	0.00	0.1667
MMP9 WT Ligation IV	0.0242	0.8928	0.9582	0.00	0.1667
MMP9 WT Ligation V	0.1572	0.3459	0.3221	0.00	0.0556
MMP9 WT Ligation VI	0.1640	0.7352	0.5553	15.00	0.1667
MMP9 WT Ligation VII	0.3140	0.5615	0.3250	0.00	0.1111
MMP9 WT Ligation VIII	0.4090	0.5882	0.0127	0.00	0.1667
Average	0.2655	0.6714	0.7431	1.88	0.1042
SD	0.1640	0.3396	0.6725	5.30	0.0753

Table 8: Material parameters identified from fitting experimental data to the strain energy function (SEF). The coefficients C_{10} and k_1 have the stress dimensions (MPa). The coefficients k_2 and γ are dimensionless parameters. Samples were individually fit to the SEF, the averaged coefficients served as the input parameters needed to model the materials biomechanical response of the material.

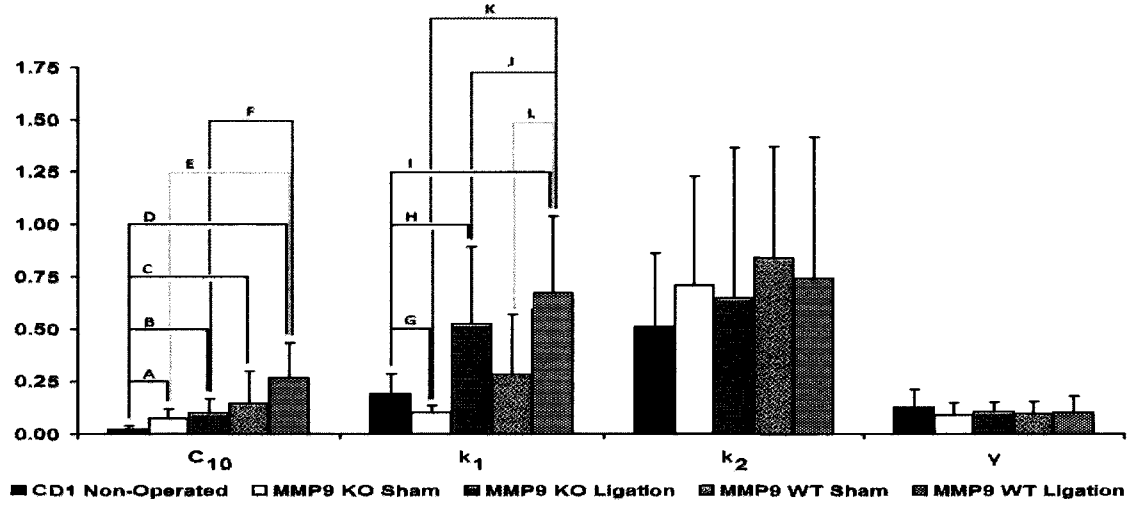

Figure 16: Material parameters (C_{10}, k_1, k_2, and γ) identified from fitting experimental data to the strain energy function (SEF) shown with means and error bars representing standard deviations. The coefficients C_{10} and k_1 have the dimensions of stress (MPa). The coefficients k_2 and γ are dimensionless parameters. The letters indicate a statistical difference with a p-value less than 0.005. P-values are listed in Table 9.

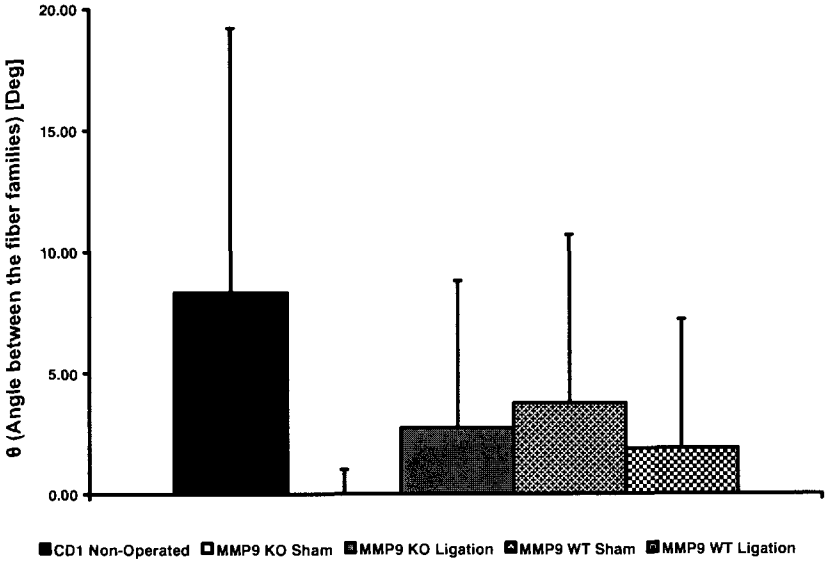

Figure 17: Material parameter (θ) identified from fitting experimental data to the strain energy function (SEF) shown with means and error bars representing standard deviations. The coefficients θ has the dimensions of degrees. P-values are listed in Table 9.

P-Values for Strain Energy Function Coefficients

C_{10}	CD1 Non-Operated	MMP9 KO Sham	MMP9 KO Ligation	MMP9 WT Sham
MMP9 KO Sham	[A] p = 0.004			
MMP9 KO Ligation	[B] p = 0.001	p = 0.483		
MMP9 WT Sham	[C] p = 0.002	p = 0.328	p = 0.710	
MMP WT Ligation	[D] p = 0.002	[E] p = 0.010	[F] p = 0.023	p = 0.151

k_1	CD1 Non-Operated	MMP9 KO Sham	MMP9 KO Ligation	MMP9 WT Sham
MMP9 KO Sham	[G] p = 0.049			
MMP9 KO Ligation	[H] p = 0.040	[J] p = 0.050		
MMP9 WT Sham	p = 0.810	p = 0.130	p = 0.107	
MMP WT Ligation	[I] p = 0.008	[K] p = 0.001	p = 0.422	[L] p = 0.027

k_2	CD1 Non-Operated	MMP9 KO Sham	MMP9 KO Ligation	MMP9 WT Sham
MMP9 KO Sham	p = 0.375			
MMP9 KO Ligation	p = 0.704	p = 0.433		
MMP9 WT Sham	p = 0.136	p = 0.625	p = 0.173	
MMP WT Ligation	p = 0.810	p = 0.721	p = 0.591	p = 0.505

θ	CD1 Non-Operated	MMP9 KO Sham	MMP9 KO Ligation	MMP9 WT Sham
MMP9 KO Sham	p = 0.131			
MMP9 KO Ligation	p = 0.301	p = 0.528		
MMP9 WT Sham	p = 0.467	p = 0.442	p = 0.834	
MMP WT Ligation	p = 0.264	p = 0.721	p = 0.867	p = 0.721

γ	CD1 Non-Operated	MMP9 KO Sham	MMP9 KO Ligation	MMP9 WT Sham
MMP9 KO Sham	p = 0.360			
MMP9 KO Ligation	p = 0.594	p = 0.264		
MMP9 WT Sham	p = 0.413	p = 0.721	p = 0.714	
MMP WT Ligation	p = 0.629	p = 0.688	p = 0.967	p = 0.839

Table 9: P-values comparing the material parameter coefficients for each sample groups calculated from the SEF. Values preceded by a brackets letter correspond to a significant difference highlighted in Figure 16. P-values less than 0.05 where considered statistically significant.

To illustrate the simulated response relative to the averaged material parameters from the strain energy function, plots of the simulated stress-stretch behavior based on the strain energy function together with the underlying averaged experimental data (1 to 1 and 2 to 1 stretch protocols) are depicted in Figures 18-22. The stress-stretch plots show the mechanical responses, i.e., Cauchy stress vs. stretch of

the different tissues in the circumferential and axial directions. All five tissue groups exhibited a pronounced anisotropic and nonlinear mechanical response. It was observed that the model evaluated with the average constants provided a good approximation of the averaged experimental data.

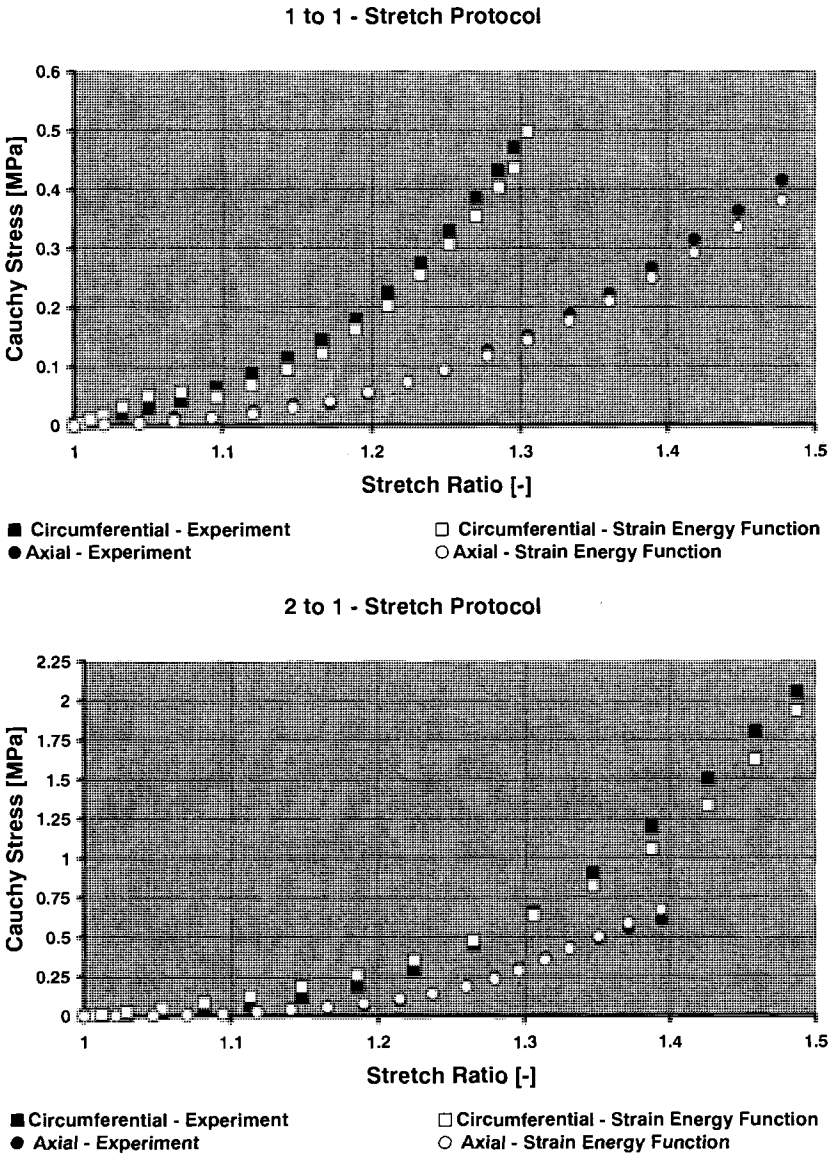

Figure 18: CD1 Non-Operated group: Cauchy stress versus stretch ratio for the 1 to 1 (*Top)* and 2 to 1 (*Bottom*) biaxial stretch testing protocols. The stress based on the strain energy function along with the experimentally measured stress are plotted against the corresponding primary stretches (Axial and Circumferential).

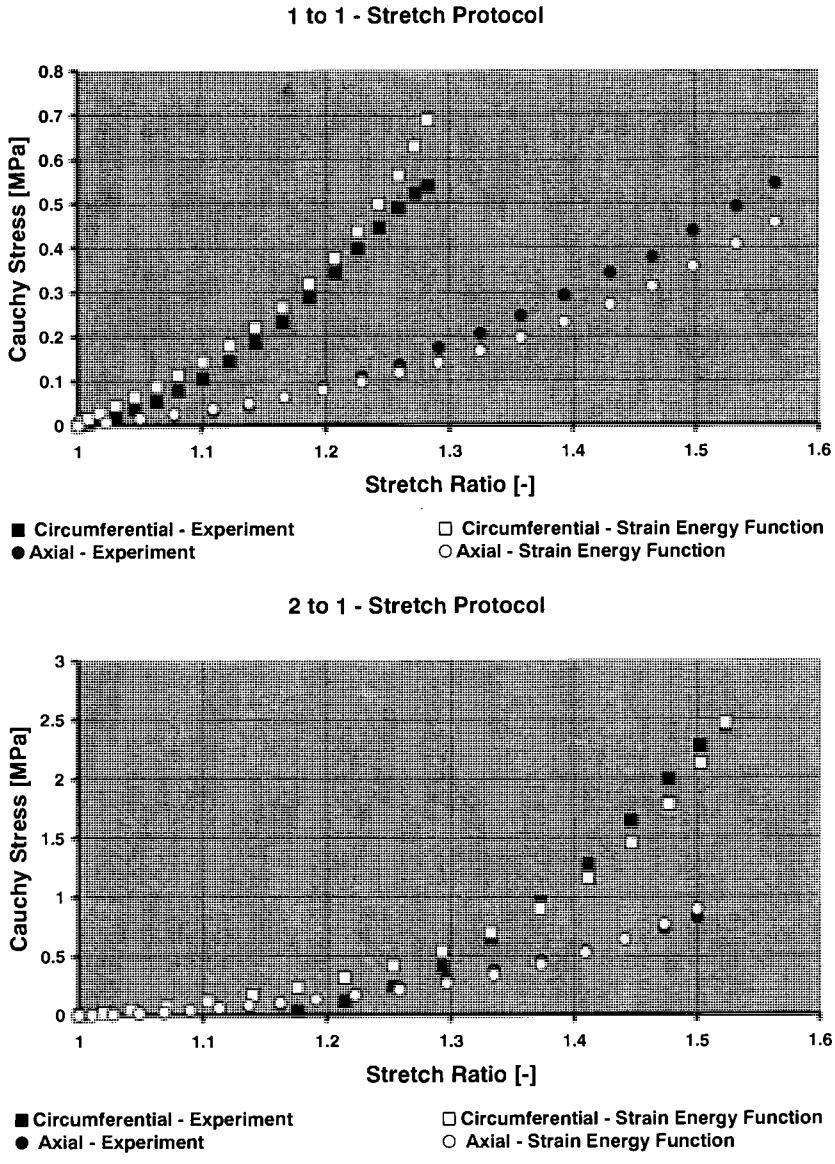

Figure 19: MMP-9 KO Sham group: Cauchy stress versus stretch ratio for the 1 to 1 (*Top*) and 2 to 1 (*Bottom*) biaxial stretch testing protocols. The stress based on the strain energy function along with the experimentally measured stress are plotted against the corresponding primary stretches (Axial and Circumferential).

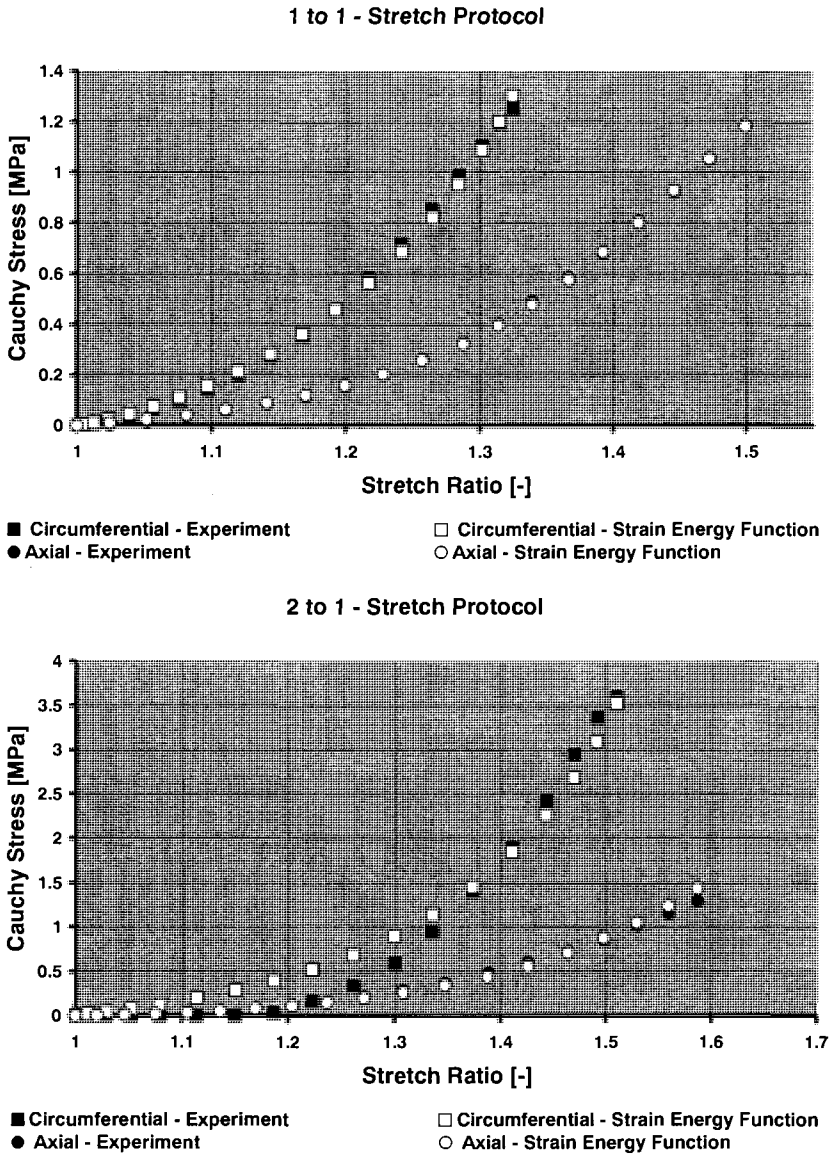

Figure 20: MMP-9 KO Ligation group: Cauchy stress versus stretch ratio for the 1 to 1 (*Top*) and 2 to 1 (*Bottom*) biaxial stretch testing protocols. The stress based on the strain energy function along with the experimentally measured stress are plotted against the corresponding primary stretches (Axial and Circumferential).

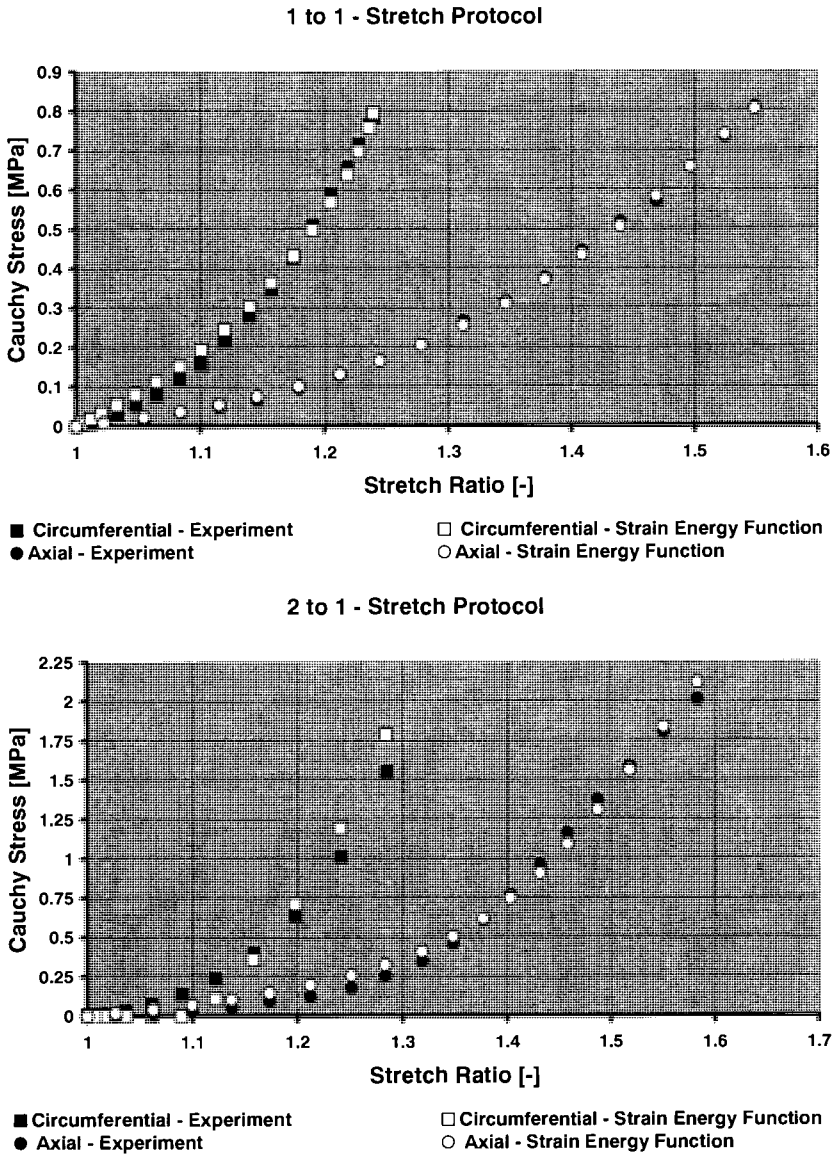

Figure 21: MMP-9 WT Sham group: Cauchy stress versus stretch ratio for the 1 to 1 (*Top*) and 2 to 1 (*Bottom*) biaxial stretch testing protocols. The stress based on the strain energy function along with the experimentally measured stress are plotted against the corresponding primary stretches (Axial and Circumferential).

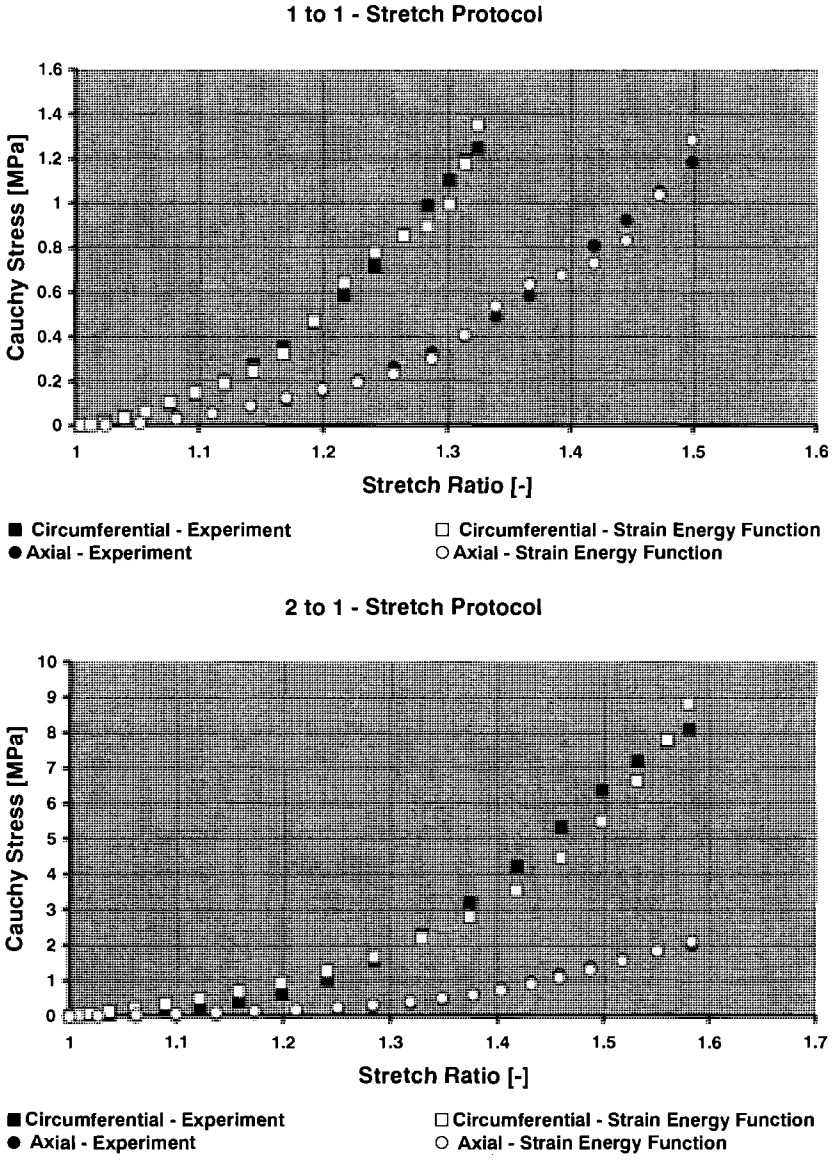

Figure 22: MMP-9 WT Ligation group: Cauchy stress versus stretch ratio for the 1 to 1 (*Top*) and 2 to 1 (*Bottom*) biaxial stretch testing protocols. The stress based on the strain energy function along with the experimentally measured stress are plotted against the corresponding primary stretches (Axial and Circumferential).

To check the analytic validity and accuracy of the material parameters derived from the strain energy function, the experimentally measured stresses from the 0 to1 and 1 to 0 stretch protocols were compared to the simulated stress data based on the

experimentally measured stretch profiles from these protocols. Succinctly, the stretch values, measured during the uniaxial loading protocols (0 to 1 and 1 to 0), along with corresponding material parameters (C_{10}, k_1, k_2, κ, and y) calculated from the 1 to 1 and 2 to 1 stretch protocols served as input variables into the strain energy function. The resultant simulated stress outputs were compared to the experimentally measured stresses for the same stretch protocols. The responses are illustrated in Figures 23-27. To add in visualization two vertical axes scales were employed, where curves on the right of the plot area correspond to the axis on the right. The excellent agreement ($r^2 \geq$ 0.95 for all cases) between the simulated and experimental stresses for these stretch protocols indicates that the derived material coefficients provide a good model for the material's biomechanical response under a wide range of loading cases - both uniaxial and biaxial.

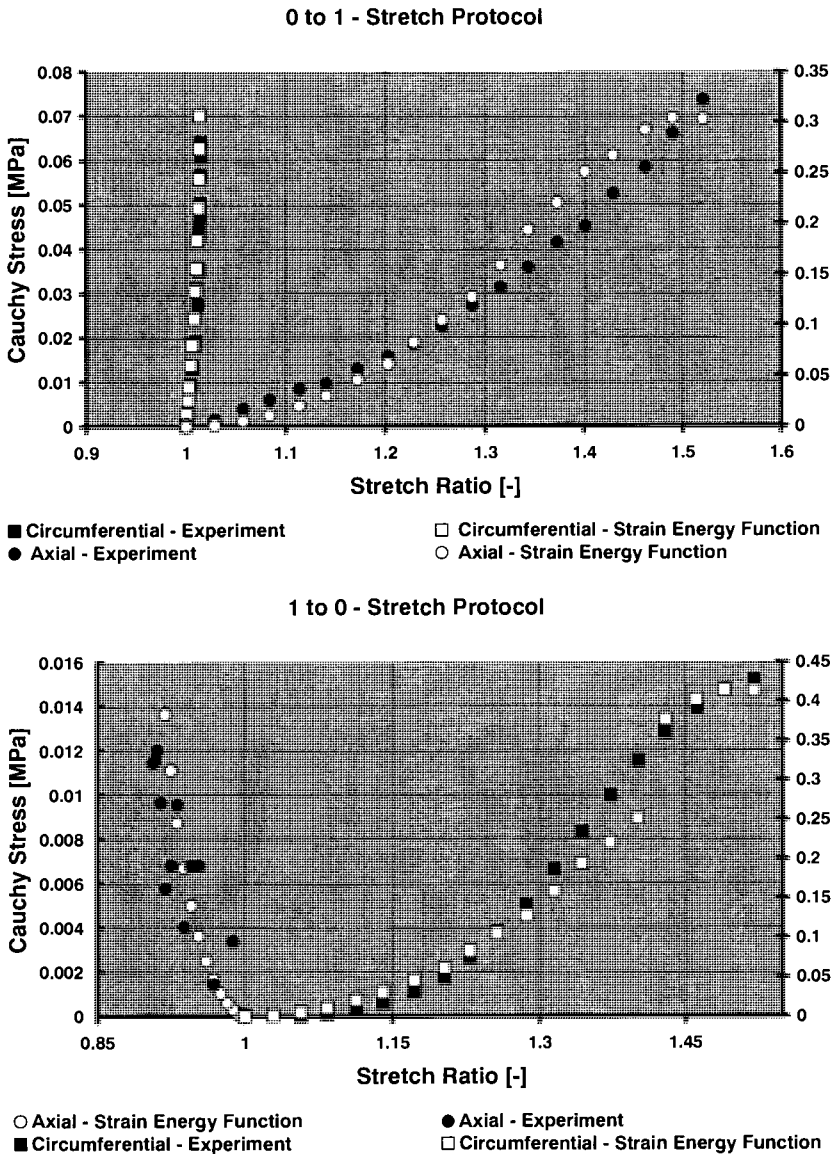

Figure 23: CD1 Non-Operated group: Cauchy stress versus stretch ratio for the 0 to 1 (*Top*) and 1 to 0 (*Bottom*) biaxial stretch testing protocols. Material parameter coefficients used were derived from the 1 to 1 and 2 to 1 stretch protocols for the sample group. Vertical axes values correspond with the curve to which they are closest.

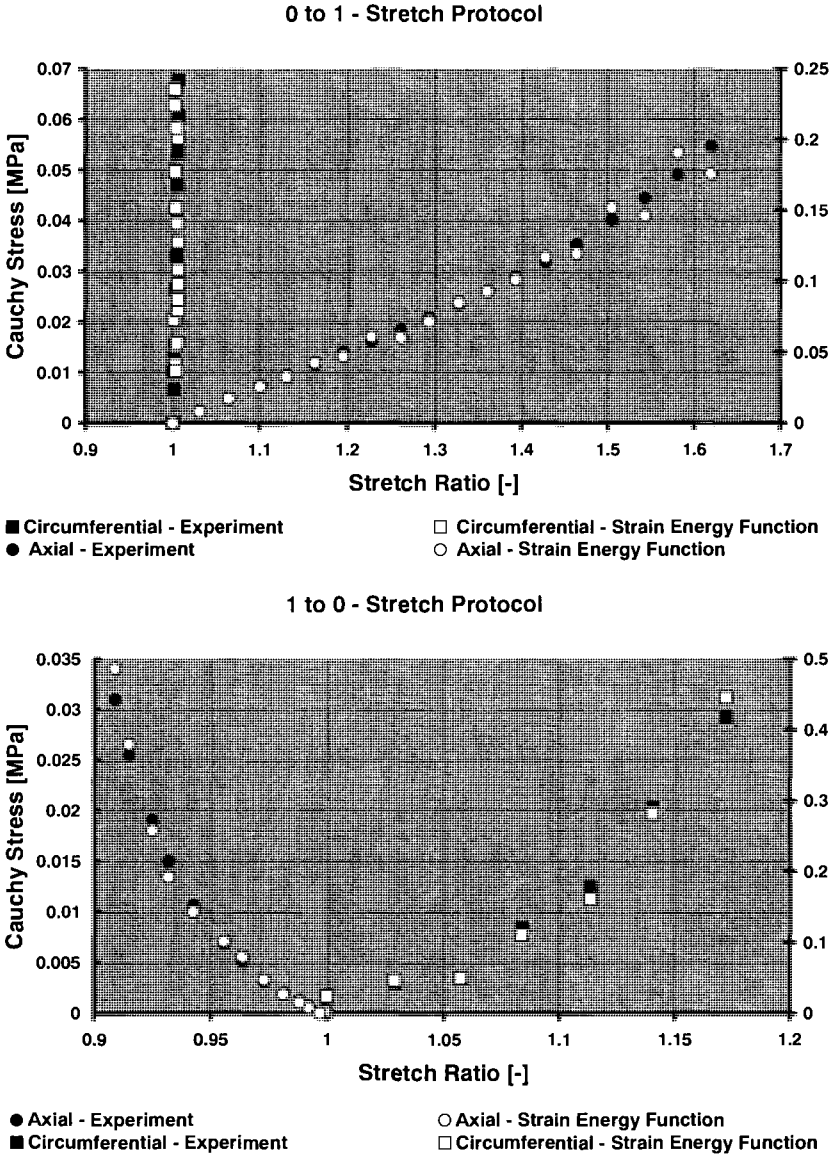

Figure 24: MMP-9 KO Sham group: Cauchy stress versus stretch ratio for the 0 to 1 ((*Top*) and 1 to 0 (*Bottom*) biaxial stretch testing protocols. Material parameter coefficients used were derived from the 1 to 1 and 2 to 1 stretch protocols for the sample group. Vertical axes values correspond with the curve to which they are closest.

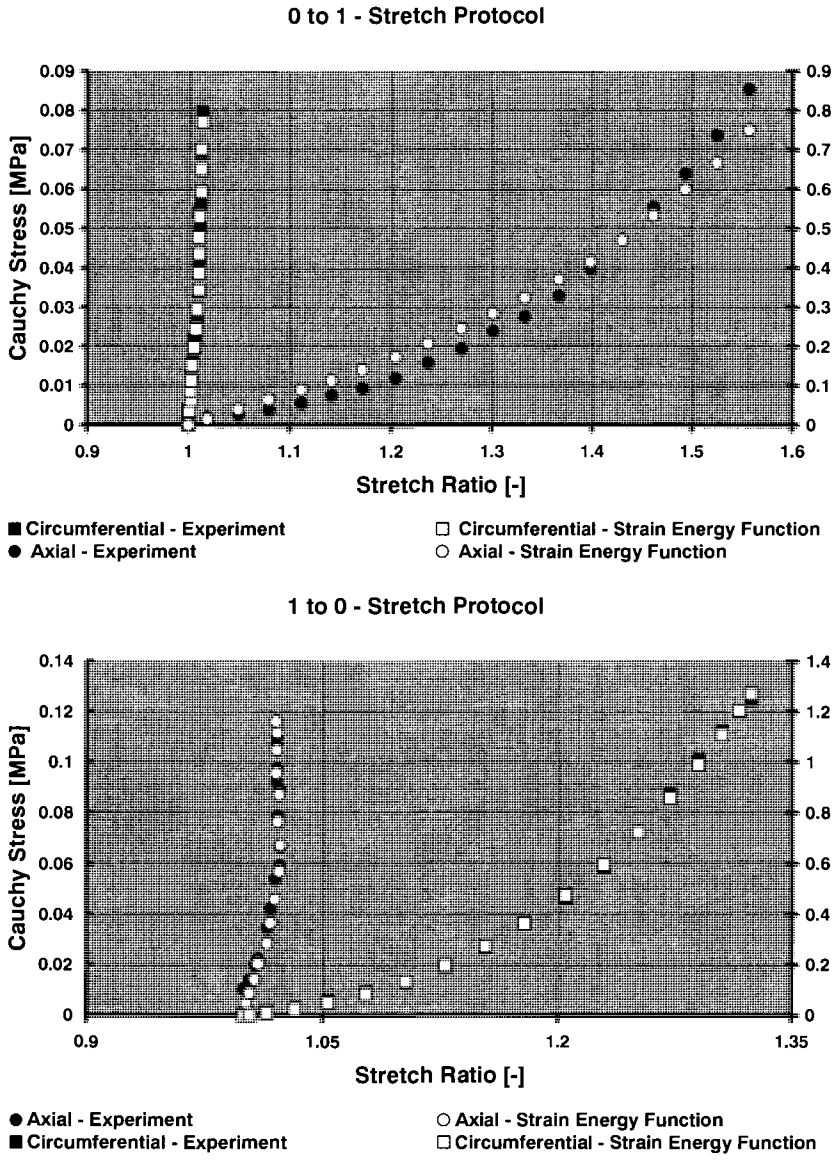

Figure 25: MMP-9 KO Ligation group: Cauchy stress versus stretch ratio for the 0 to 1 (*Top*) and 1 to 0 (*Bottom*) biaxial stretch testing protocols. Material parameter coefficients used were derived from the 1 to 1 and 2 to 1 stretch protocols for the sample group. Vertical axes values correspond with the curve to which they are closest.

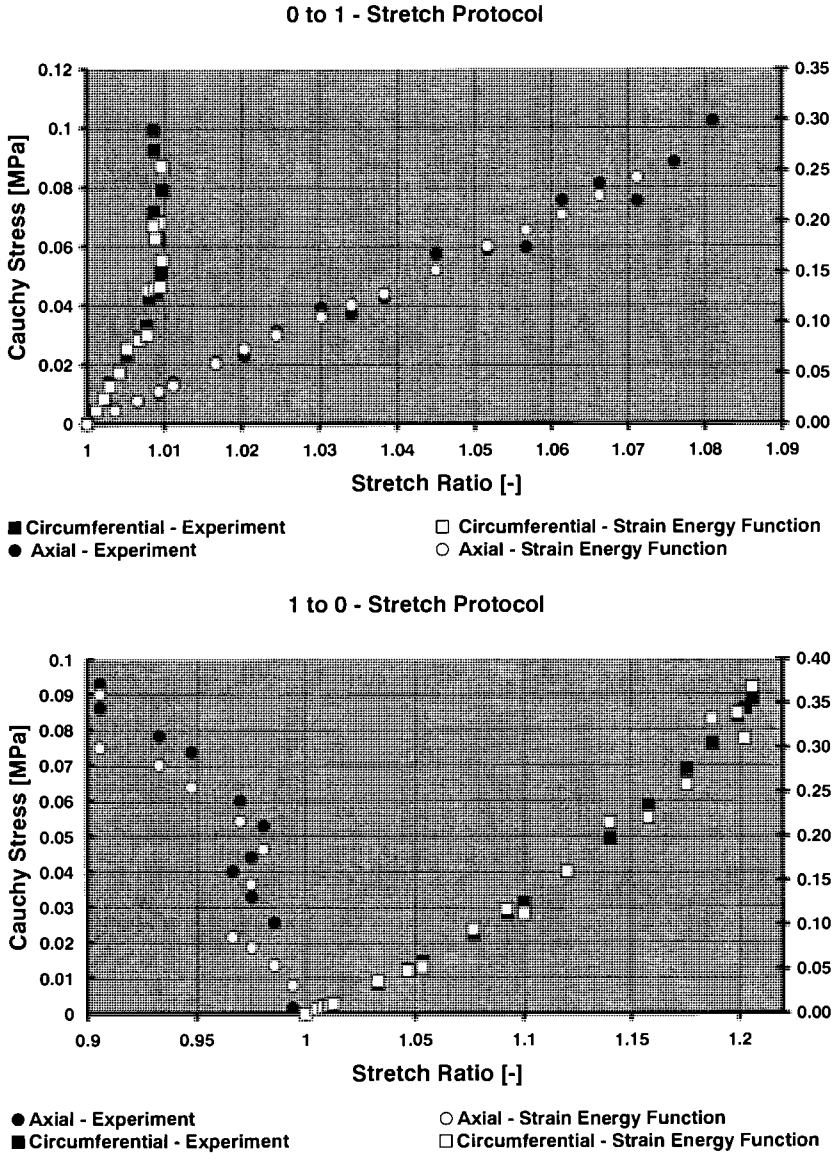

Figure 26: MMP-9 WT Sham: Cauchy stress versus stretch ratio for the 0 to 1 (*Top*) and 1 to 0 (*Bottom*) biaxial stretch testing protocols. Material parameter coefficients used were derived from the 1 to 1 and 2 to 1 stretch protocols for the sample group. Vertical axes values correspond with the curve to which they are closest.

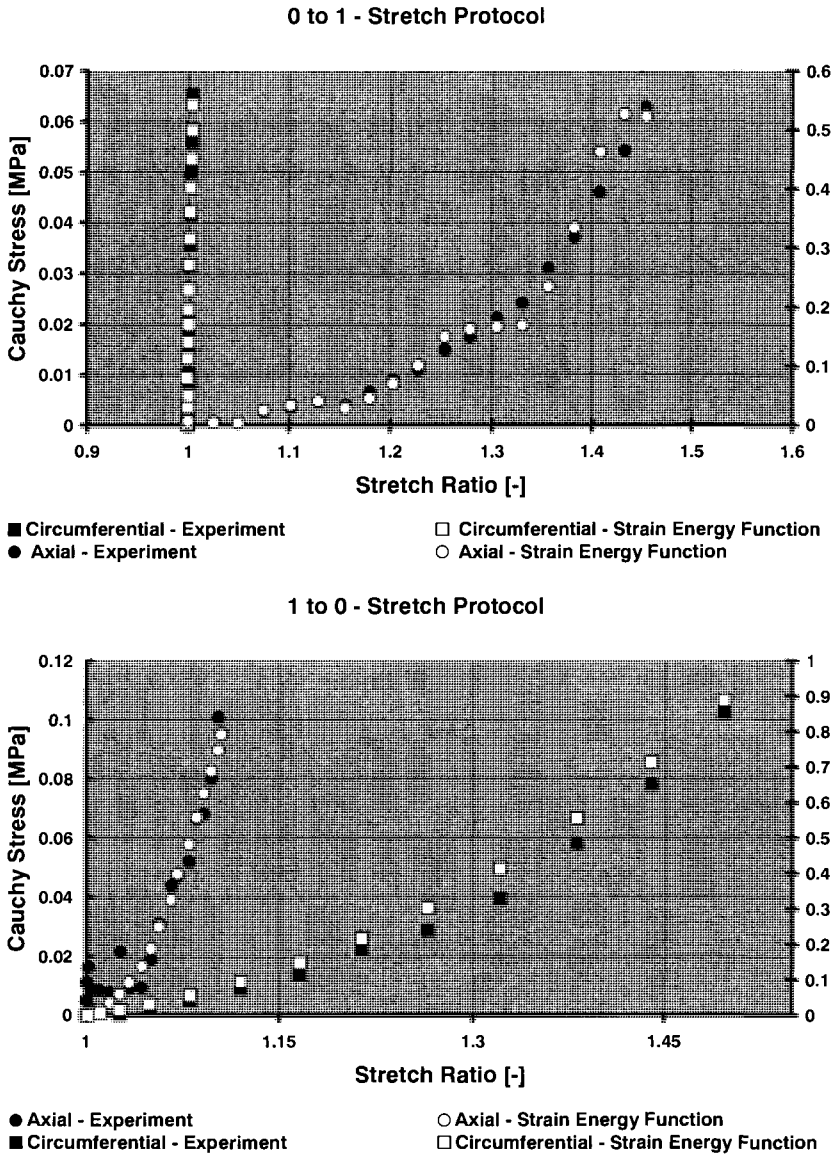

Figure 27: MMP-9 WT Ligation group: Cauchy stress versus stretch ratio for the 0 to 1 (*Top*) and 1 to 0 (*Bottom*) biaxial stretch testing protocols. Material parameter coefficients used were derived from the 1 to 1 and 2 to 1 stretch protocols for the sample group. Vertical axes values correspond with the curve to which they are closest.

7.3 Biaxial Stretch Experiment: Discussion

The strain energy function selected for this study was capable of accurately modeling the experimental biaxial data over the wide range of physiologically - relevant

biaxial stretch protocols. The response to multiple loading protocols revealed the complex planar behavior of the IVC. Specifically, a non-monotonic, highly nonlinear relationship between stress and strain was observed. The proposed constitutive model is based in part on histological information [37]. It therefore allows the material parameters to be associated with the individual constituents (extracellular matrix and collagen/elastin fiber families) of each mechanically relevant component within the vessel wall.

The structural coefficient C_{10} [MPa], associated with the first term of the strain energy function, represents the response of the non-collagenous isotropic ground material. The coefficient C_{10}, exhibited the greatest differences between sample groups, demonstrating statistical difference in 6 of the possible 10 comparisons between experimental variants (Table 9). Functionally, statistical differences in the value of the C_{10} coefficient indicate that there are significant alterations in the extracellular matrix (ECM) ground substance between groups. An increase in the C_{10} coefficient correlates to an increase in the overall strain energy stored in the material for a given stretch. From a functional standpoint, this means the vessel is demonstrating reduced compliance. As the value of C_{10} increases the corresponding stress calculated from the SEDF must also increase for a given stretch ratio. The data indicate that both the sham and ligation procedure (regardless of the murine model) significantly affect the ECM ground substance when compared to a non-operated CD1 control This is not surprising considering the preparation of the sham and ligation specimens involved surgical intervention which initiates, at a minimum, some degree of

the healing cascade. The manifestation of this healing appears to have a significant effect on the ECM of the venous wall.

The analyses indicate that there was a statistical difference in the value of C_{10} between the MMP-9 KO groups and the MMP-9 WT groups. Comparisons between the MMP-9 KO groups and the MMP-9 WT groups give insight into the effect that MMP-9 has on the biomechanical response of the tissue. A statistically significant increase of 253% in the value of C_{10} was noted for the MMP-9 WT Ligation group when compared against the MMP-9 KO Sham group. However, no statistically significant difference was noted between the MMP-9 KO Sham group and the MMP-9 KO Ligation group. This indicates that ligation of MMP-9 KO venous tissue does not significantly increase vein wall stiffness when compared to the corresponding shams. This seems to suggest that the knockout of MMP-9 (i.e. target gene therapy designed to remove MMP-9) could be an appealing solution to battle the clinical complications that arise following increased venous wall stiffness following DVT. A similar statistically significant increase of 169% in the value of C_{10} was noted for the MMP-9 WT Ligation group when compared against the MMP-9 KO Ligation group. These findings indicate that MMP-9 does play an important role in determining the biomechanical response of the venous tissue following any type of surgical intervention, however, this effect is significant following ligation. These results demonstrate that if MMP-9 is suppressed prior to thrombosis resolution then the deleterious effect of increased vein wall stiffness, manifested as a loss of ECM compliance (i.e. increased value of the C_{10} coefficient), are drastically

reduced by several orders of magnitude. It is hypothesized this would lead to a dramatic decrease in clinical complications caused by increased vein wall stiffness.

Statically significant changes between groups were also noted for the strain energy coefficient k_1 [MPa] (Figure 6, Table 9). From a physiological perspective, the parameter k_1 is associated with the anisotropic contribution of the collagen/elastin to the overall response of the material. Increases in the material parameter k_1 correspond to an increase in the magnitude of the second term of the strain energy equation. An increase in the second term of the SEDF manifests as increased stress under stretch, indicative of a stiffer, less compliant material. The mechanism through which the stiffness of the collagen fibers increase is unclear, whether it is solely due to changes in the ECM in which they are embedded, conformation / biochemical alterations within the fibers structure, or in the cross-linking of the fibers themselves. Future histological efforts hope to address this question. Regardless of the underlying microstructural mechanism, increases in the value of k_1 translate to a less compliant and stiffer material, and conversely, decreases in the value of k_1 indicate an increase in compliance. Statistically significant changes in the value of k_1 were noted for the MMP-9 KO Sham (-87%), MMP-9 KO Ligation (+170%), and the MMP-9 WT Ligations (+247%) groups as compared to the CD1 Non-operated control group. The data indicate that simulated DVT, via IVC ligation, leads to an increase in the stiffness of the fiber constituents in the vessel wall, which is independent of the model variant. Statically significant changes were also noted between the KO and WT groups for the k_1 parameter. Specifically, the MMP-9 KO Sham group had a k_1 value that is several orders of magnitude below that of

both the MMP-9 KO Ligation and MMP-9 WT Ligation groups (407% and 550% relative differences, respectively). A similar statistically significant trend was observed between the MMP-9 WT Sham and the MMP-9 WT Ligation groups, where the MMP-9 WT Ligation group demonstrated an increase of 137% in the mean measured k_1 value. These findings indicate that, regardless of the murine model examined, vessel ligation has a statistically significant and deleterious effect on the stiffness of the collagen/elastin fibers as compared to either control values or sham values. MMP-9 regulation did not have a statically significant effect on the response of the k_1 values, as demonstrated by no statically significant differences between the MMP-9 KO Ligation or MMP WT Ligation groups. However, this is not entirely unexpected. It has been reported that the primary role of MMP-9 is to regulate/breakdown the ECM during the wound healing cascade and contribute to degradation of collagen. The data presented within this study seem to indicate that, from a biomechanical standpoint, MMP-9 has an affects on the biomechanical response behavior of the ECM and on the collagen fibers following DVT.

No statistically significant differences where noted between the groups for the strain energy parameters k_2 [-], θ [Deg], and γ [-]. Physiologically, the parameter k_2 is associated with the anisotropic contribution of the collagen/elastin fibers [37], however its physical meaning is not entirely clear. The parameter k_2 can be considered to control the degree of non-linearity of the material; increases in k_2 are commiserate with increases in the non-linear response of the strain energy function. The data indicate that the degree of non-linearity (i.e. the value of k_2) is unaffected by murine model type

or MMP-9 expression. The dispersion and the preferred spatial orientations of the fiber families were also unaffected by murine model type andMMP-9 expression. These data would indicate that future histological efforts using these specific murine models should not use fiber dispersion or orientation as resultant outcome parameters. Rather, the current study suggests that collagen type and extracellular matrix constituents would give more insight in a histological study.

It is clear that ligation of the vessel leads to increased stiffness of the ECM and the anisotropic contribution of the collagen fibers. The data further sheds positive light on the hypothesis that clinical complications following DVT are directly related to changes in the compliance (calculated as the inverse of stiffness) of the vein wall. DVT - induced specimens exhibited a marked increase in the overall stiffness (i.e. a decrease in compliance) of the vessel wall under biaxial loading conditions. From a mechanical and structural perspective, DVT resolution produces statically significant changes in the ECM and fiber responses.

8.0 BIOMECHANICAL EVALUATION SUMMARY

8.1 Biomechanical Evaluation Summary: Uniaxial Tension Experiments

In summary the uniaxial tension experiments and analysis indicated:

- Complete ligation has the greatest effect on geometric parameters;
- Low flow ligation increases longitudinal\axial load at failure;
- Complete and partial ligation increase longitudinal\axial stiffness;
- Low flow ligation increases failure stress;

- Low flow ligation increases elastic modulus.

8.2 Biomechanical Evaluation Summary: Nanoindentation Experiments

In summary the nanoindentation experiments and analysis indicated:

- Unloading stiffness is the greatest in the longitudinal\axial direction;
- The JKR elastic moduli formulation provides the most accurate representation of hydrated indentation of venous tissue;
- Luminal elastic modulus is statistically increased following ligation;
- Longitudinal and circumferential modulus are increased following ligation.

8.3 Biomechanical Evaluation Summary: Biaxial Stretch Experiments

In summary the biaxial stretch experiments and analysis indicated:

- The strain energy function provides an accurate representation of venous wall tissue;
- Ligation significantly increases the stiffness of the ECM;
- MMP-9 KO significantly reduces the deleterious effects of increased ECM stiffness following ligation;
- Ligation significantly decreased the compliance of the collagen/elastin fibers;
- MMP-9 KO significantly reduces the deleterious effects of increased collagen/elastin stiffness following ligation;
- Sham procedures do alter the biomechanical response of the ECM and the fiber families.

9.0 FINITE ELEMENT MODELING

9.0 Finite Element Modeling: Background

Finite element modeling (FEM) offers the advantages of being able to model structures with intricate shapes and indirectly quantify different complex mechanical parameters at any point within the body [1]. FEM on healthy and DVT induced vessels provides a quantitative tool for predicting and diagnosing the effects of thrombus resolution under a vast range of conditions that is not possible to evaluate *in vivo* or clinically. Biomechanical data collected and analyzed following biaxial stretch testing was incorporated into a FEM of the murine inferior vena cava. Using the coefficients determined from the strain energy function presented by Ogden et al. [37] and the relevant biaxial stretch biomechanical data (strain energy coefficients, Tables 4 - 5), a FEM model using simplified geometry was developed in Abaqus CAE (Simulia, San Diego, CA, USA). In order to assess the changes in these internal mechanical parameters due solely to alterations in the material properties, a simplified "straight tube" geometry was used to represent the geometric structure of the vessel. The FEM model presented within the scope of this research project used validated material properties and was subjected to physiologically relevant boundary conditions and ranges in pressures from baseline to those observed following severe DVT occlusion of the vessel.

Blood vessels are known to undergo finite deformations under normal physiological conditions, and for this reason, vascular tissue has been modeled using hyperelastic material formulae by many researchers [93]. The venous tissue was considered to be an incompressible, homogenous, hyperelastic material undergoing

finite deformation in the present study. The material constants derived from the strain energy density function (SEDF) following biaxial stretch experiments served as input parameters for the FEM of the IVC.

9.0 Finite Element Modeling: Methods

Five material and geometric specific FEMs were generated using Abaqus CAE. Linear solid hybrid elements (C3D8H) were used to model the incompressible deformation of the vena cava wall. The mechanical response of the material was modeled using the anisotropic, hyperelastic strain energy function proposed by Gasser, Holzapfel, and Ogden [37] to model the arterial layers with heterogeneously distributed collagen fiber orientations. For this study, it was assumed that the vein wall was composed of two families of fibers embedded in a soft incompressible ground matrix. The coefficients that determine the response of the tissue were based on the least-squared fitting of the longitudinal and circumferential biaxial stretch experiments.

Five geometric (and material) specific straight tube models were generated using the averaged geometry measured during biaxial stretch experiments (Table 10). The length of the tube was designated to be a minimum of thirty times the inner radial dimension. This insured that a region of interest that was free of the edge effects (St. Venant's considerations) due to the loading and boundary conditions could be discretized for output parameter calculations.

	Experimental Measurements		Model Paramters		
	Width (mm)	Thickness (mm)	Inner Radius (mm)	Wall Thickness (mm)	Length (mm)
CD1 Non-Operated	0.6109 ± 0.0478	0.0343 ± 0.0105	0.0972	0.0343	3
MMP9 KO Sham	0.5460 ± 0.0986	0.0425 ± 0.0143	0.0869	0.0425	3
MMP9 KO Ligation	0.5852 ± 0.1024	0.0881 ± 0.0398	0.0931	0.0881	3
MMP9 WT Sham	0.5405 ± 0.0234	0.0301 ± 0.0213	0.0860	0.0301	3
MMP9 WT Ligation	0.5013 ± 0.0789	0.1048 ± 0.0409	0.0798	0.1042	3

Table 10: Geometric parameters calculated during biaxial stretch testing. Means are shown with standard deviations. Parameters served at inputs for finite element modeling.

The two free ends of the tube were fixed in the three axes of loading with primary rotation unconstrained at the vessel's termini. A cylindrical coordinate system was used in which the first axis was orientated in the radial outward direction away from the central axis of the tube; the second axis was orientated parallel to the circumferential direction of the tube; the third axis was orientated parallel to the longitudinal axis of the tube (Figure 28).

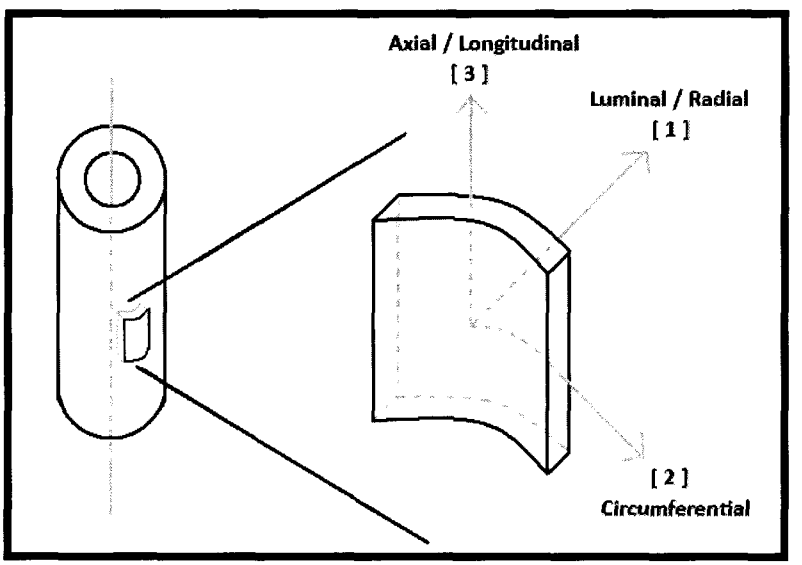

Figure 28: Coordinate system orientation used during finite element analysis.

A uniform pressure was applied to the inner surface of the vessel wall (luminal surface) with a smooth, step amplitude curve. The technical challenges of measuring venous pressure inside the peritoneum of a murine model have not yet been overcome; thus, the exact *in vivo* vena cava pressure is currently not available in the literature. However, vena cave luminal pressures measured in a rat model have been shown to range from almost zero to 3mm Hg (0.4kPa), where the physiological transmural pressure is approximately 2mm Hg (0.27kPa) [99]. Three intraluminal pressures (0.13kPa, 0.27kPa, 0.53kPa) where chosen to bound these physiologically relevant venous pressures, ranging from the lower physiologic range to the physiologic mean to hypertensive.

Finite element solution resolution is sensitive to mesh density when large deformation and nonlinear material responses are involved. To address this issue, three models of varying mesh density were developed in order to verify model convergence (Figure 29 - 31). The models ranged from 190 to 12,000 elements. The material coefficients derived during biaxial stretch experiments from the CD1 Non-Operated control group were used during the convergence study. Total model strain energy per unit volume versus circumferential stress measured at pressure of 0.53kPa was used to determine convergence (Figure 32). A convergence threshold of within 5% of the highest resolution mesh was considered a valid model with sufficient mesh resolution. The mid-resolution mesh (1,520 elements) was determined to have sufficient mesh resolution for this analysis (Figure 32 - 33).

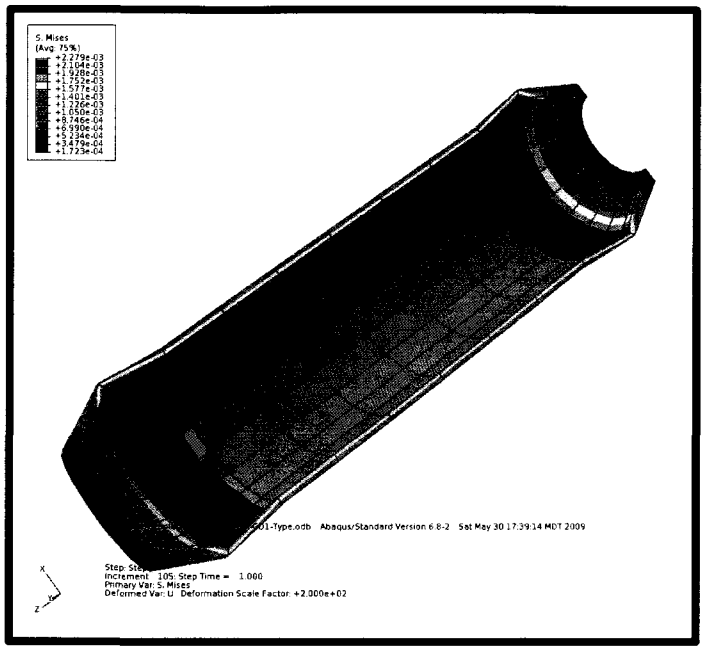

Figure 29: Low (190 Elements) mesh resolution FEM. Deformed cross-section shown under 0.53kPa of luminal pressure. Deformations have been magnified by 200% for visualization purposes.

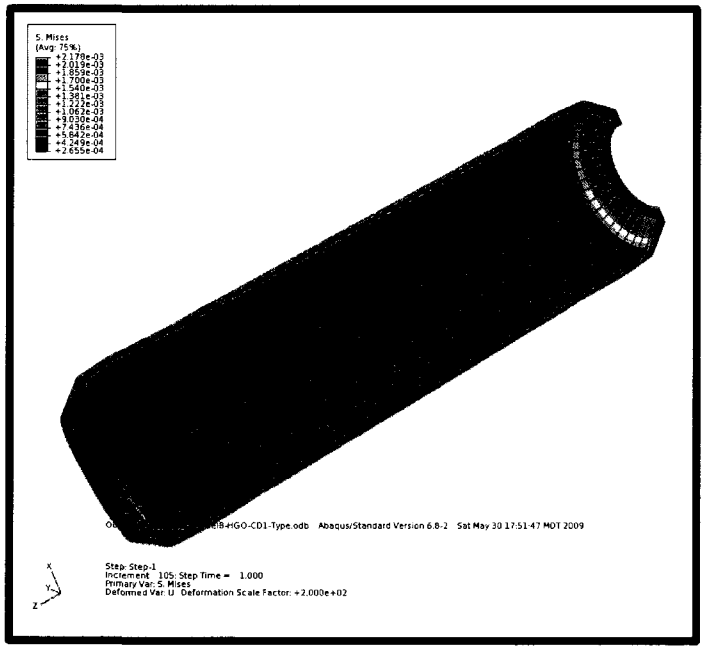

Figure 30: Mid (1,520 Elements) mesh resolution FEM. Deformed cross-section shown under 0.53kPa of luminal pressure. Deformations have been magnified by 200% for visualization purposes.

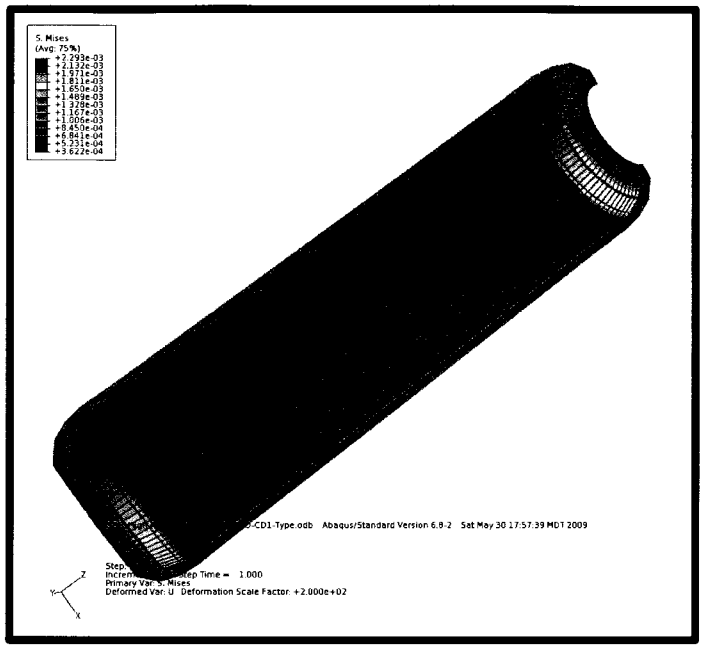

Figure 31: High (12,000 Elements) mesh resolution FEM. Deformed cross-section shown under 0.53kPa of luminal pressure. Deformations have been magnified by 200% for visualization purposes.

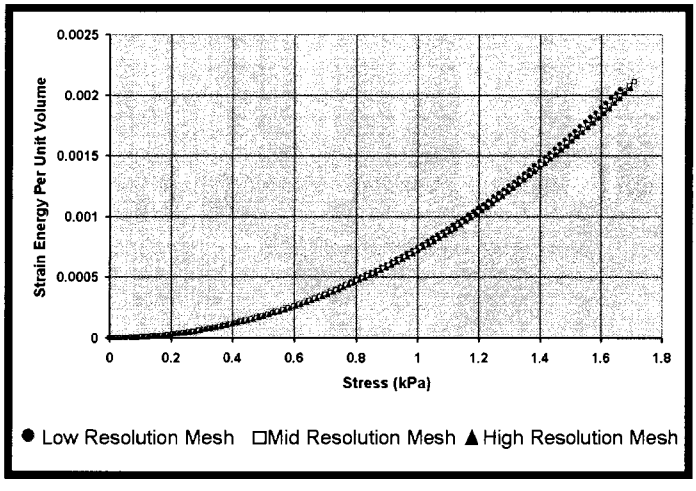

Figure 32: Strain energy per unit volume plotted against circumferential stress at a luminal pressure of 0.53 kPa for the three mesh resolutions

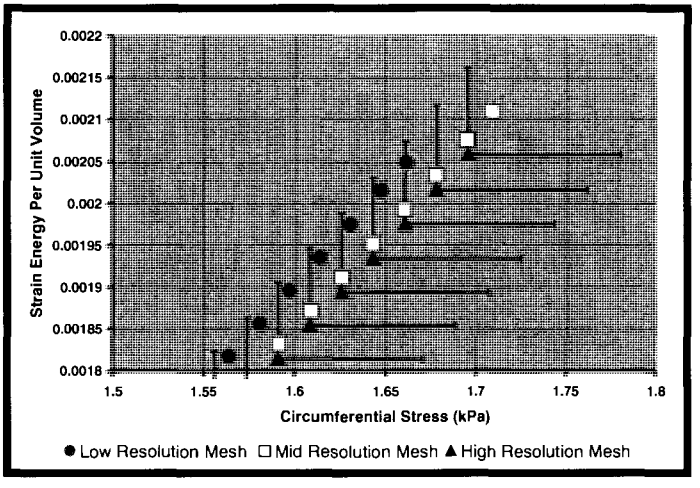

Figure 33: The peak stress – displacement predictions with error bars representing 5% of the calculated values of the highest resolution mesh are highlighted.

In summary using the mid-resolution model, five material and geometric specific FEMs (CD1 Non-Operated, MMP-9 KO Sham, MMP-9 KO Ligation, MMP-9 WT Sham, and MMP-9 WT Ligation) were used to predict stresses and displacements in the primary directions of loading (luminal, circumferential, and axial / flow) under a range of loading cases (0.13 MPa, 0.27 MPa, 0.53 MPa). The predicted stress values corresponded to the engineering stress components aligned with the cylindrical coordinate system. The predicted displacement values are also aligned with the cylindrical coordinate system of the FEM. The stress-displacement relationship served to indicate qualitative differences between groups and between loading regimes.

9.0 Finite Element Modeling: Results

An average of sixteen nodes located in the vessel centrum on the luminal surface of the vein wall was chosen for parameter identification (Figure 34). The same node set was analyzed across all models. The highest stress values were found to be on the

luminal surface of the vessel, and thus, the remainder of this analysis focused on this specific region.

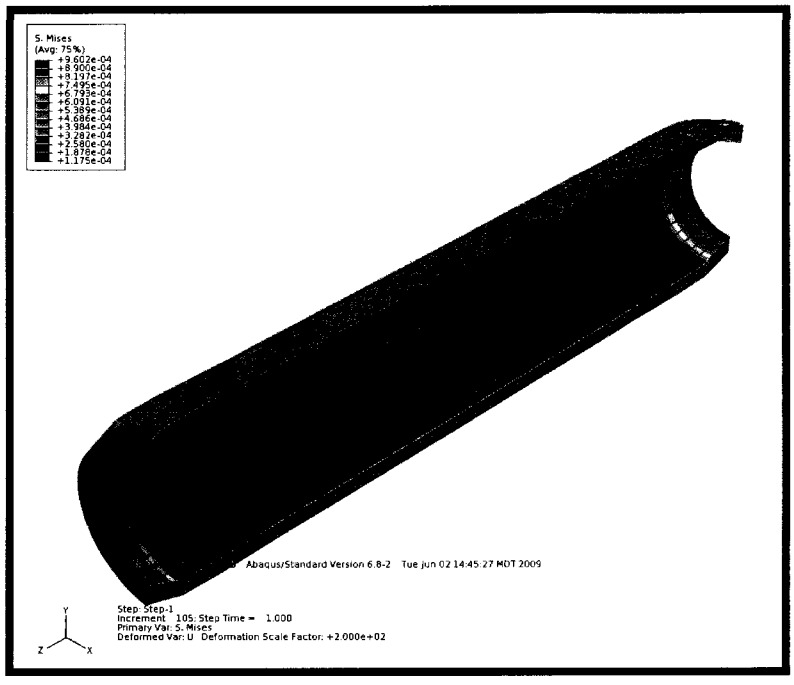

Figure 34: Node set used to define FEM output predictions are highlighted in grey. The highest stresses were observed on the luminal surface, and, therefore this region was chosen as the region of interest.

To illustrate the predicted response based on the FEM variants, plots of the simulated stress-displacement behavior are depicted in Figures 35 - 43. The stress-displacement plots show the biomechanical responses of the tissues in the luminal, circumferential and axial directions. The data have been arranged to demonstrate the engineering stress component aligned with the respective cylindrical axes of interest (i.e. Circumferential, Axial, and Luminal) plotted against the displacement within the region of interest. As a measure of relative change between treatment groups for a

specific loading case and direction of interest, the percent differences between peak stresses and displacements were calculated between the model variants (Table 11-19).

Biaxial stretch experimentation has demonstrated that sham surgical intervention statistically alters the biomechanical properties of the tissue, in both the ECM response and fiber contribution, as compared to control values. Sham – ligation comparisons gave the most precise representation of the effect of simulated DVT resolution. These comparisons remove "surgical intervention" as a confounding factor, making the ligation procedure the primary variable of observation. Therefore, direct comparisons between ligation and their corresponding sham groups have been highlighted (Table 11 - 19).

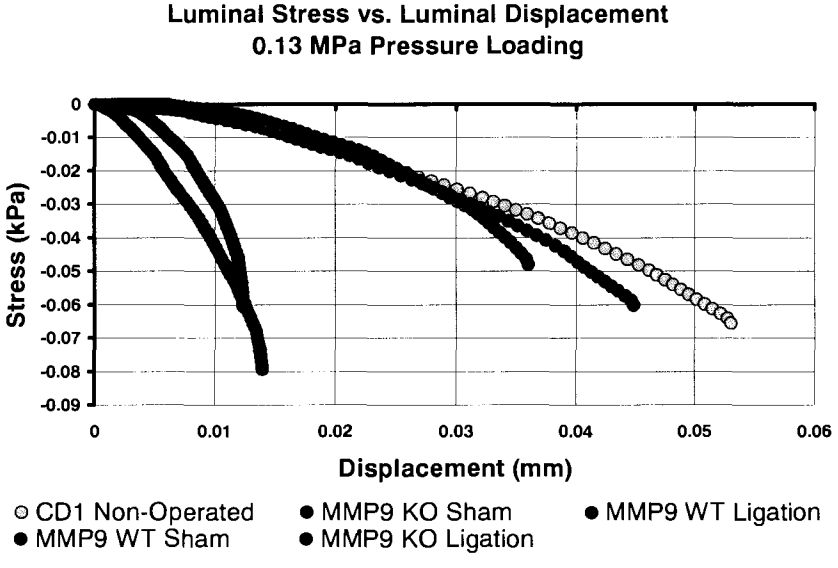

Figure 35: Luminal / Radial stress component versus corresponding displacement response predicted under 0.13 MPa of luminal pressure.

Luminal Orientation - 0.13 MPa Pressure Loading

Group	Stress (kPa)
CD1 Non-Operated	-0.066
MMP9 KO Sham	-0.060
MMP9 KO Ligation	-0.061
MMP9 WT Sham	-0.048
MMP9 WT Ligation	-0.079

Group	Displacement (mm)
CD1 Non-Operated	0.053
MMP9 KO Sham	0.045
MMP9 KO Ligation	0.012
MMP9 WT Sham	0.036
MMP9 WT Ligation	0.014

Stress - Percent Difference Between Groups				
	CD1 Non-Operated	MMP9 KO Sham	MMP9 KO Ligation	MMP9 WT Sham
MMP9 KO Sham	8.74%			
MMP9 KO Ligation	8.05%	0.69%		
MMP9 WT Sham	31.05%	22.46%	23.14%	
MMP9 WT Ligation	18.95%	27.57%	26.89%	49.27%

Displacement - Percent Difference Between Groups				
	CD1 Non-Operated	MMP9 KO Sham	MMP9 KO Ligation	MMP9 WT Sham
MMP9 KO Sham	16.33%			
MMP9 KO Ligation	126.15%	115.79%		
MMP9 WT Sham	38.20%	22.22%	100.00%	
MMP9 WT Ligation	116.42%	105.08%	320.27%	88.00%

Table 11: Predicted engineering stress and displacement components aligned with the luminal axis. Percent relative change between treatment groups was calculated. Percent differences between ligation and their corresponding sham groups have been highlighted.

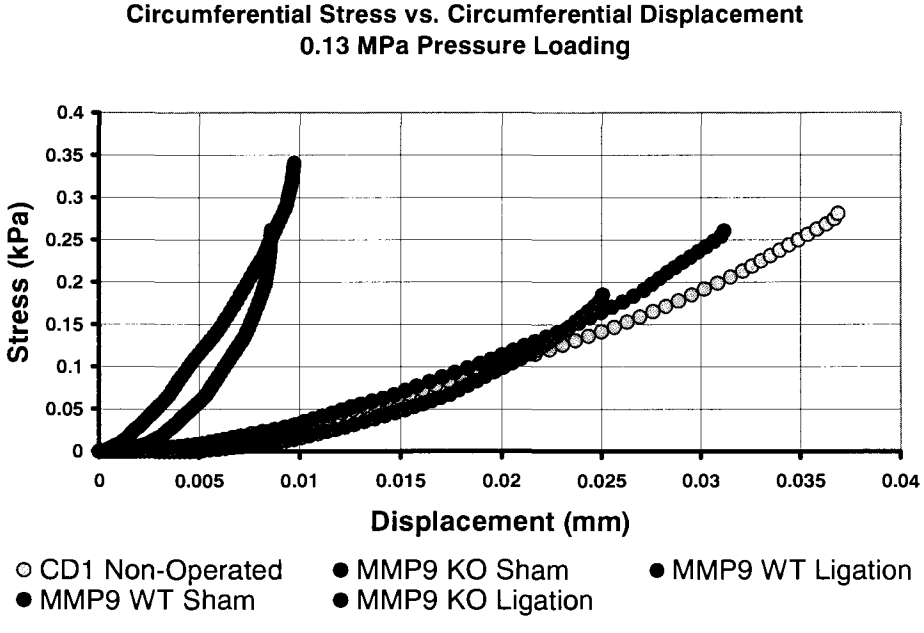

Figure 36: Circumferential stress – displacement response predicted under 0.13 MPa of luminal pressure.

Circumferential Orientation - 0.13 MPa Pressure Loading

Group	Stress (kPa)
CD1 Non-Operated	0.284
MMP9 KO Sham	0.263
MMP9 KO Ligation	0.265
MMP9 WT Sham	0.188
MMP9 WT Ligation	0.347

Group	Displacement (mm)
CD1 Non-Operated	0.037
MMP9 KO Sham	0.031
MMP9 KO Ligation	0.001
MMP9 WT Sham	0.025
MMP9 WT Ligation	0.010

Stress - Percent Difference Between Groups

	CD1 Non-Operated	MMP9 KO Sham	MMP9 KO Ligation	MMP9 WT Sham
MMP9 KO Sham	7.68%			
MMP9 KO Ligation	6.92%	0.76%		
MMP9 WT Sham	40.68%	33.26%	34.00%	
MMP9 WT Ligation	19.97%	27.54%	26.80%	59.44%

Displacement - Percent Difference Between Groups

	CD1 Non-Operated	MMP9 KO Sham	MMP9 KO Ligation	MMP9 WT Sham
MMP9 KO Sham	17.65%			
MMP9 KO Ligation	190.50%	188.71%		
MMP9 WT Sham	38.71%	21.43%	186.10%	
MMP9 WT Ligation	114.89%	102.44%	185.45%	85.71%

Table 12: Predicted engineering stress and displacement components aligned with the circumferential axis. Percent relative change between treatment groups was calculated. Percent differences between ligation and their corresponding sham groups have been highlighted.

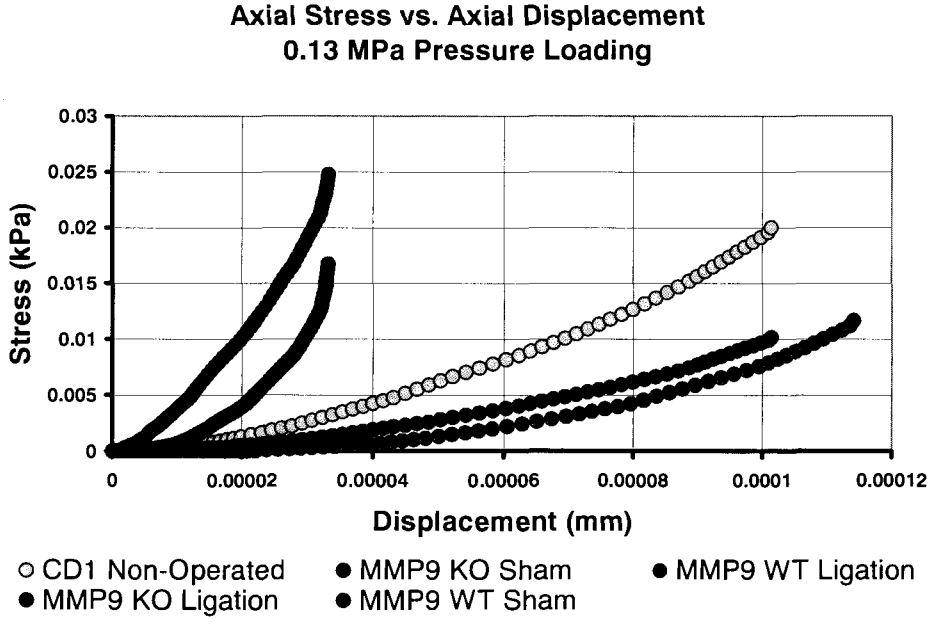

Figure 37: Axial / Longitudinal stress – displacement response predicted under 0.13 MPa of luminal pressure.

Axial Orientation - 0.13 MPa Pressure Loading

Group	Stress (kPa)
CD1 Non-Operated	0.020
MMP9 KO Sham	0.010
MMP9 KO Ligation	0.012
MMP9 WT Sham	0.017
MMP9 WT Ligation	0.025

Group	Displacement (mm)
CD1 Non-Operated	1.012E-04
MMP9 KO Sham	1.012E-04
MMP9 KO Ligation	3.308E-05
MMP9 WT Sham	1.139E-05
MMP9 WT Ligation	3.308E-05

Stress - Percent Difference Between Groups				
	CD1 Non-Operated	MMP9 KO Sham	MMP9 KO Ligation	MMP9 WT Sham
MMP9 KO Sham	66.67%			
MMP9 KO Ligation	50.00%	18.18%		
MMP9 WT Sham	16.22%	51.85%	34.48%	
MMP9 WT Ligation	22.22%	85.71%	70.27%	38.10%

Displacement - Percent Difference Between Groups				
	CD1 Non-Operated	MMP9 KO Sham	MMP9 KO Ligation	MMP9 WT Sham
MMP9 KO Sham	0.00%			
MMP9 KO Ligation	101.47%	101.47%		
MMP9 WT Sham	159.54%	159.54%	97.54%	
MMP9 WT Ligation	101.47%	101.47%	198.90%	97.54%

Table 13: Predicted engineering stress and displacement components aligned with the axial / longitudinal axis. Percent relative change between treatment groups was calculated. Percent differences between ligation and their corresponding sham groups have been highlighted.

The finite element analysis demonstrated ligation causes a significant decrease in vein wall distensability in the three directions of interest within the lower range of physiologic pressure (0.13 MPa). Finite element modeling predicts that dilatation decreases following ligation are between 88% in the luminal direction to 188% in the circumferential direction as compared to sham values. In the three axes of loading, the knock-out (KO) material model demonstrated the largest reduction in displacement as compared to sham values, while the wild-type (WT) model demonstrated the greatest increase in stress, as compared to sham values. The data indicate, within in the lower physiologic pressure range, that MMP-9 regulation (i.e. MMP-9 KO) reduces the stress generated in the wall as compared to wild type (WT) ligation predictions between 20 – 50%. Regulation of MMP-9 seems to have little effect on vein wall displacement as

compared to the wild type values. Suppression of MMP-9 expression reduces the stress generated within the vein wall, however, this suppression does not appear to reduce the deleterious effects of reduced dilation. Trends (i.e. grouping and value proximity) between the shams and control values for stress and displacement are consistent across all axes of interest.

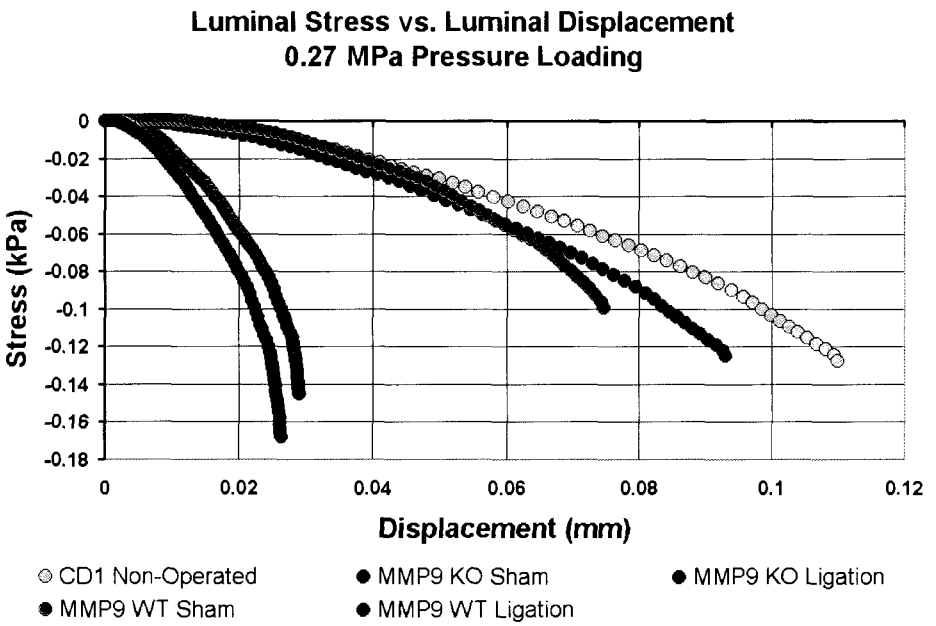

Figure 38: Luminal / Radial stress – displacement response predicted under 0.27 MPa of luminal pressure.

Luminal Orientation - 0.27 MPa Pressure Loading

Group	Stress (kPa)
CD1 Non-Operated	-0.127
MMP9 KO Sham	-0.125
MMP9 KO Ligation	-0.147
MMP9 WT Sham	-0.101
MMP9 WT Ligation	-0.165

Group	Displacement (mm)
CD1 Non-Operated	0.110
MMP9 KO Sham	0.093
MMP9 KO Ligation	0.075
MMP9 WT Sham	0.029
MMP9 WT Ligation	0.026

Stress - Percent Difference Between Groups

	CD1 Non-Operated	MMP9 KO Sham	MMP9 KO Ligation	MMP9 WT Sham
MMP9 KO Sham	1.59%			
MMP9 KO Ligation	14.60%	16.18%		
MMP9 WT Sham	22.81%	21.24%	37.10%	
MMP9 WT Ligation	26.03%	27.59%	11.54%	48.12%

Displacement - Percent Difference Between Groups

	CD1 Non-Operated	MMP9 KO Sham	MMP9 KO Ligation	MMP9 WT Sham
MMP9 KO Sham	16.75%			
MMP9 KO Ligation	37.84%	21.43%		
MMP9 WT Sham	116.55%	104.92%	88.46%	
MMP9 WT Ligation	123.53%	112.61%	285.95%	10.91%

Table 14: Predicted engineering stress component aligned with the luminal axis and displacement in that same axes calculated within the region of interest. Percent relative change between treatment groups was calculated. Percent differences between ligation and corresponding sham groups have been highlighted.

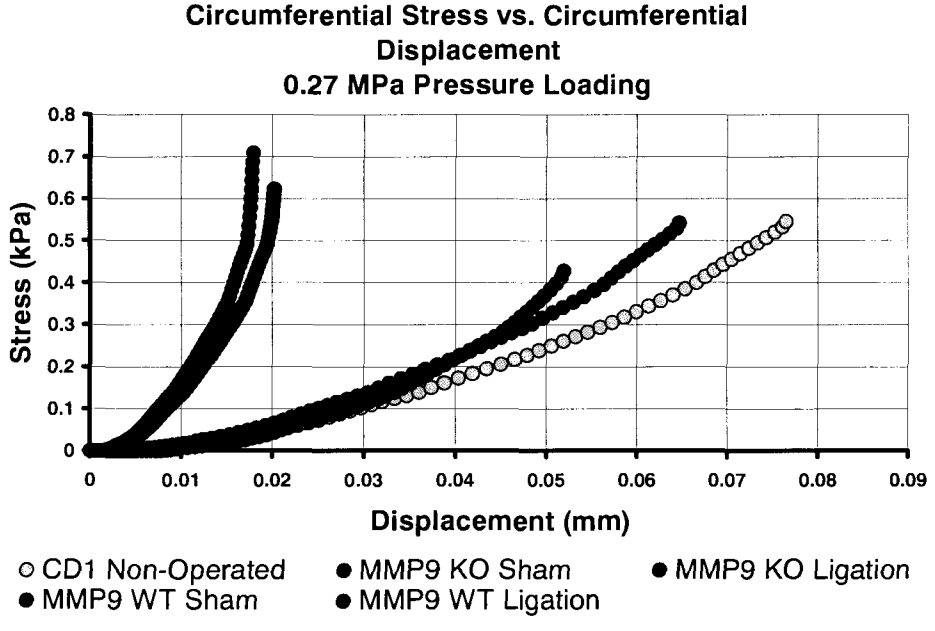

Figure 39: Circumferential stress – displacement response predicted under 0.27 MPa of luminal pressure.

Circumferential Orientation - 0.27 MPa Pressure Loading

Group	Stress (kPa)
CD1 Non-Operated	0.550
MMP9 KO Sham	0.548
MMP9 KO Ligation	0.622
MMP9 WT Sham	0.428
MMP9 WT Ligation	0.710

Group	Displacement (mm)
CD1 Non-Operated	0.076
MMP9 KO Sham	0.052
MMP9 KO Ligation	0.020
MMP9 WT Sham	0.065
MMP9 WT Ligation	0.018

Stress - Percent Difference Between Groups

	CD1 Non-Operated	MMP9 KO Sham	MMP9 KO Ligation	MMP9 WT Sham
MMP9 KO Sham	0.36%			
MMP9 KO Ligation	12.29%	12.65%		
MMP9 WT Sham	24.95%	24.59%	36.95%	
MMP9 WT Ligation	25.40%	25.76%	13.21%	49.56%

Displacement - Percent Difference Between Groups

	CD1 Non-Operated	MMP9 KO Sham	MMP9 KO Ligation	MMP9 WT Sham
MMP9 KO Sham	37.50%			
MMP9 KO Ligation	116.67%	88.89%		
MMP9 WT Sham	15.60%	22.22%	105.88%	
MMP9 WT Ligation	123.40%	97.14%	188.75%	113.25%

Table 15: Predicted engineering stress component aligned with the circumferential axis and displacement in that same axes calculated within the region of interest. Percent relative change between treatment groups was calculated. Percent differences between ligation and corresponding sham groups have been highlighted.

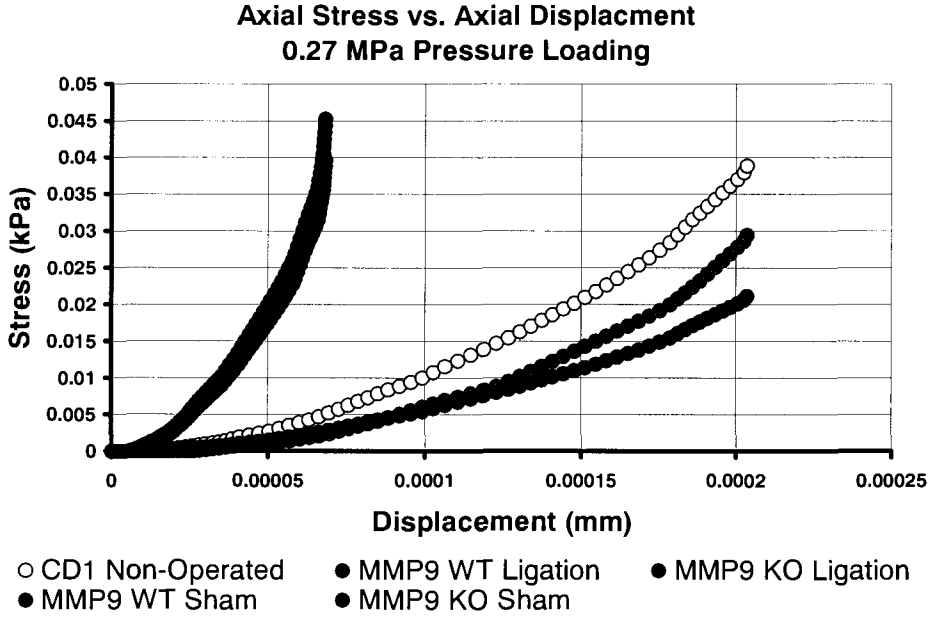

Figure 40: Axial / Longitudinal stress – displacement response predicted under 0.27 MPa of luminal pressure.

Axial Orientation - 0.27 MPa Pressure Loading

Group	Stress (kPa)
CD1 Non-Operated	0.039
MMP9 KO Sham	0.020
MMP9 KO Ligation	0.039
MMP9 WT Sham	0.029
MMP9 WT Ligation	0.045

Group	Displacement (mm)
CD1 Non-Operated	2.0345E-04
MMP9 KO Sham	2.0270E-04
MMP9 KO Ligation	6.8320E-04
MMP9 WT Sham	2.0383E-04
MMP9 WT Ligation	6.7940E-04

Stress - *Percent Difference Between Groups*

	CD1 Non-Operated	MMP9 KO Sham	MMP9 KO Ligation	MMP9 WT Sham
MMP9 KO Sham	64.41%			
MMP9 KO Ligation	0.00%	64.41%		
MMP9 WT Sham	29.41%	36.73%	29.41%	
MMP9 WT Ligation	14.29%	76.92%	14.29%	43.24%

Displacement - Percent Difference Between Groups

	CD1 Non-Operated	MMP9 KO Sham	MMP9 KO Ligation	MMP9 WT Sham
MMP9 KO Sham	0.37%			
MMP9 KO Ligation	108.22%	108.48%		
MMP9 WT Sham	0.19%	0.56%	108.08%	
MMP9 WT Ligation	107.82%	108.08%	193.15%	107.69%

Table 16: Predicted engineering stress component aligned with the circumferential axis and displacement in that same axes calculated within the region of interest. Percent relative change between treatment groups was calculated. Percent differences between ligation and corresponding sham groups have been highlighted.

Reductions in displacement were predicted for the three axes of loading following ligation as compared to both sham and control values, which correlated with increased stress values. Under a normal physiologic pressure distribution (0.27 MPA), the wall stresses increased between 13 – 65% following ligation as compared to the corresponding sham values. Stress was predicted to be the greatest in the circumferential direction, as compared to both the luminal and axial directions. Accordingly, luminal displacement was calculated as the largest between axes. Finite element modeling demonstrated that the vein wall undergoes compression (negative stress values) in the luminal direction. Predicted values of stress for the MMP-9 regulation (KO) model where reduced as compared to WT prediction in the three axes of loading. Ligation appeared to have a larger deleterious decreasing effect on displacement values as compared to deleterious increases in stress predictions. Dilation or the vessel's ability to expand under internal pressurization was reduced following

ligation between 10 – 130%. The MMP-9 KO material FEM demonstrated reduced stress and increased compliance as compared to the MMP-9 WT model. Control and sham groups demonstrated similar stress –displacement behavior, however the sham material models do demonstrate the effects of surgical intervention, as demonstrated by changes in peak stress and displacement when compared to control values. Finite element modeling indicates that the material coefficients used to model both the WT and KO ligation groups demonstrates increased stress under low displacements as compared to both control and sham values. Prediction based on the ligation material models demonstrate that DVT resolution decreases vessel compliance as demonstrated by a reduced capacity to displace in the three directions of loading.

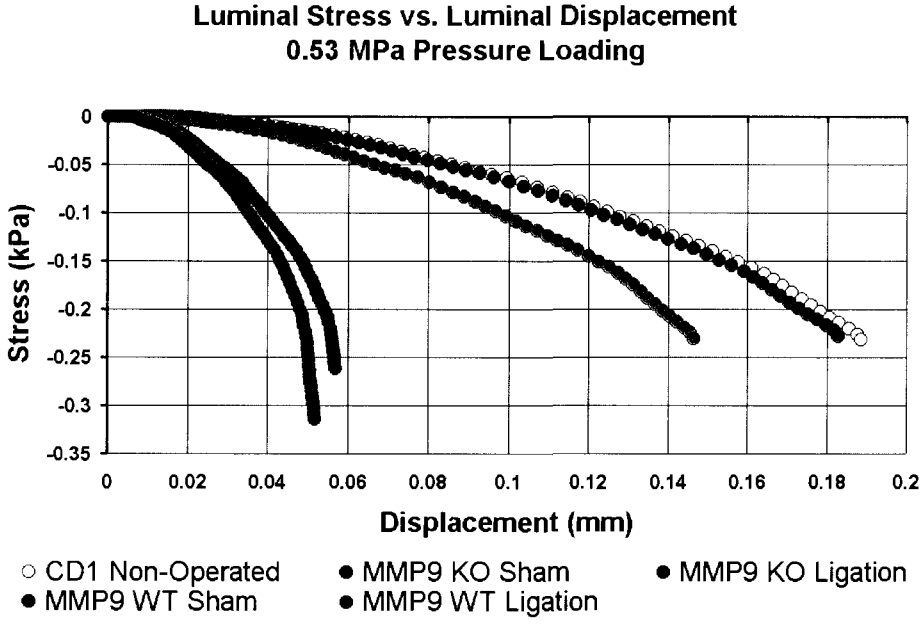

Figure 41: Luminal / Radial stress – displacement response predicted under 0.54 MPa of luminal pressure.

Luminal Orientation - 0.53 MPa Pressure Loading

Group	Stress (kPa)
CD1 Non-Operated	-0.230
MMP9 KO Sham	-0.229
MMP9 KO Ligation	-0.260
MMP9 WT Sham	-0.230
MMP9 WT Ligation	-0.315

Group	Displacement (mm)
CD1 Non-Operated	0.188
MMP9 KO Sham	0.183
MMP9 KO Ligation	0.057
MMP9 WT Sham	0.146
MMP9 WT Ligation	0.052

Stress - Percent Difference Between Groups

	CD1 Non-Operated	MMP9 KO Sham	MMP9 KO Ligation	MMP9 WT Sham
MMP9 KO Sham	0.44%			
MMP9 KO Ligation	12.24%	12.68%		
MMP9 WT Sham	0.00%	0.44%	12.24%	
MMP9 WT Ligation	31.19%	31.62%	19.13%	31.19%

Displacement - Percent Difference Between Groups

	CD1 Non-Operated	MMP9 KO Sham	MMP9 KO Ligation	MMP9 WT Sham
MMP9 KO Sham	2.70%			
MMP9 KO Ligation	106.94%	105.00%		
MMP9 WT Sham	25.15%	22.49%	87.68%	
MMP9 WT Ligation	113.33%	111.49%	300.00%	94.95%

Table 17: Predicted engineering stress component aligned with the luminal axis and displacement in that same axes calculated within the region of interest. Percent relative change between treatment groups was calculated. Percent differences between ligation and corresponding sham groups have been highlighted.

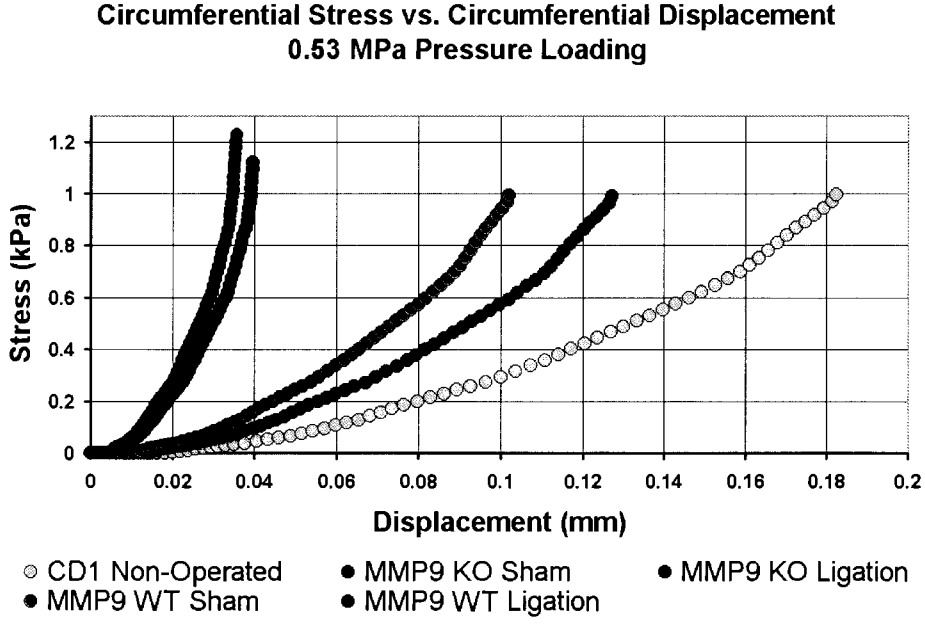

Figure 42: Circumferential stress – displacement response predicted under 0.53 MPa of luminal pressure.

Circumferential Orientation - 0.53 MPa Pressure Loading

Group	Stress (kPa)
CD1 Non-Operated	1.013
MMP9 KO Sham	1.004
MMP9 KO Ligation	1.129
MMP9 WT Sham	1.004
MMP9 WT Ligation	1.236

Group	Displacement (mm)
CD1 Non-Operated	0.182
MMP9 KO Sham	0.127
MMP9 KO Ligation	0.040
MMP9 WT Sham	0.102
MMP9 WT Ligation	0.035

Stress - Percent Difference Between Groups

	CD1 Non-Operated	MMP9 KO Sham	MMP9 KO Ligation	MMP9 WT Sham
MMP9 KO Sham	0.89%			
MMP9 KO Ligation	10.83%	11.72%		
MMP9 WT Sham	0.89%	0.00%	11.72%	
MMP9 WT Ligation	19.83%	20.71%	9.05%	20.71%

Displacement - Percent Difference Between Groups

	CD1 Non-Operated	MMP9 KO Sham	MMP9 KO Ligation	MMP9 WT Sham
MMP9 KO Sham	35.60%			
MMP9 KO Ligation	127.93%	104.19%		
MMP9 WT Sham	56.34%	21.83%	87.32%	
MMP9 WT Ligation	135.48%	113.58%	187.97%	97.61%

Table 18: Predicted engineering stress component aligned with the circumferential axis and displacement in that same axes calculated within the region of interest. Percent relative change between treatment groups was calculated. Percent differences between ligation and corresponding sham groups have been highlighted.

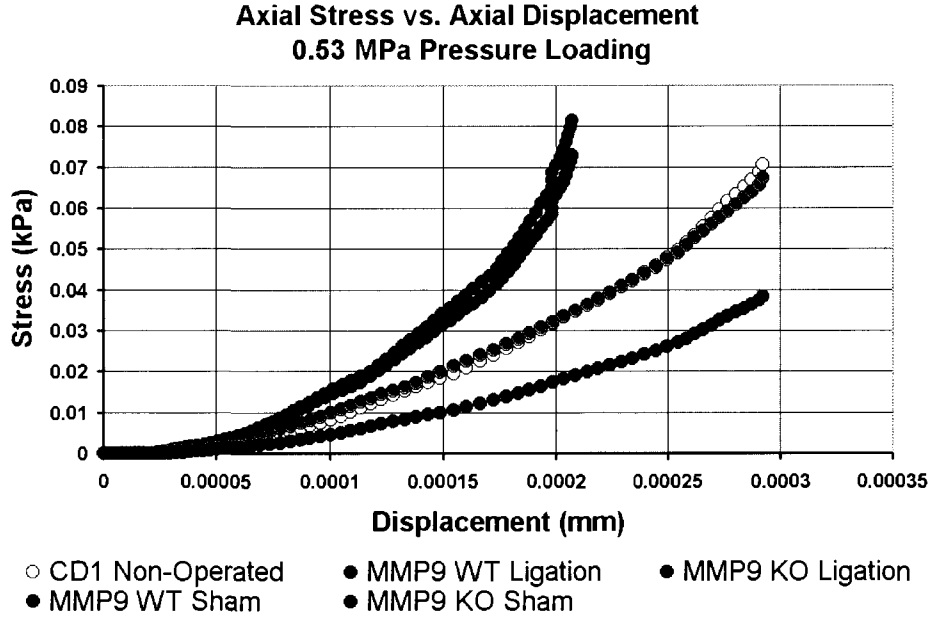

Figure 43: Axial / Longitudinal stress – displacement response predicted under 0.53 MPa of luminal pressure.

Axial Orientation - 0.53 MPa Pressure Loading

Group	Stress (kPa)
CD1 Non-Operated	0.071
MMP9 KO Sham	0.039
MMP9 KO Ligation	0.073
MMP9 WT Sham	0.067
MMP9 WT Ligation	0.083

Group	Displacement (mm)
CD1 Non-Operated	2.9175E-04
MMP9 KO Sham	2.9227E-04
MMP9 KO Ligation	2.9175E-04
MMP9 WT Sham	2.0670E-04
MMP9 WT Ligation	2.0670E-04

Stress - Percent Difference Between Groups

	CD1 Non-Operated	MMP9 KO Sham	MMP9 KO Ligation	MMP9 WT Sham
MMP9 KO Sham	58.18%			
MMP9 KO Ligation	2.78%	60.71%		
MMP9 WT Sham	5.80%	52.83%	8.57%	
MMP9 WT Ligation	15.58%	72.13%	12.82%	21.33%

Displacement - Percent Difference Between Groups

	CD1 Non-Operated	MMP9 KO Sham	MMP9 KO Ligation	MMP9 WT Sham
MMP9 KO Sham	-0.18%			
MMP9 KO Ligation	0.00%	0.18%		
MMP9 WT Sham	34.13%	34.30%	34.13%	
MMP9 WT Ligation	34.13%	34.30%	198.87%	0.00%

Table 19: Predicted engineering stress component aligned with the axial axis and displacement in that same axes calculated within the region of interest. Percent relative change between treatment groups was calculated. Percent differences between ligation and corresponding sham groups have been highlighted.

Increased stress and reduced displacement was also observed for the upper bound of physiologic loading (0.53 MPa). The MMP-9 KO material model demonstrated reduced stress as compared to the WT model.

To illustrate the reduction in dilation effect, representative FEMs are shown in Figures 44. These figures depict the CD1 Non-Operated (Inset A – B) and MMP9 WT Ligation (Inset C –D) groups under 0.27 MPa (Insert A - C) and 0.54 MPa (Inset B - D) of luminal pressure. Geometric scales are equivalent across the insets. Ligation reduced radial dilatation by 112% to 123%, for pressure loadings of 0.27MPa and 0.54MPa, respectively. This reduction in vessel expansion is easily visualized.

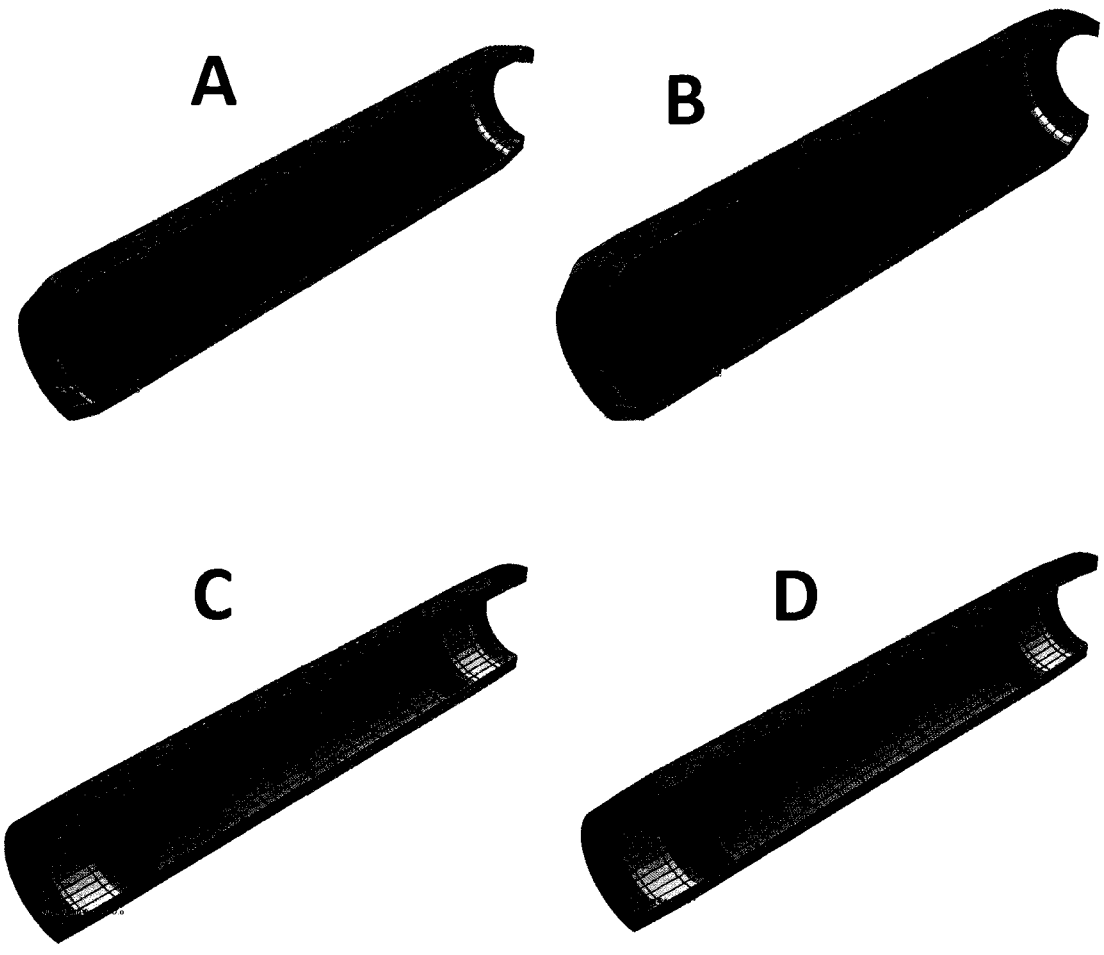

Figure 41: Finite element models depicting the CD1 Non-Operated (Inset A – B) and MMP9 WT Ligation (Inset C –D) groups under 0.27 MPa (Insert A - C) and 0.54 MPa (Inset B - D) of luminal pressure. . Geometric scale is equivalent for A - D.

9.0 Finite Element Modeling: Discussion

The stress – displacement relationships depicted from the finite element analysis emphasize the decreased compliance of the vascular wall, which is associated with increased stresses in the three primary directions of loading. All models demonstrated increased stress coupled with decreased displacement for the MMP-9 WT and MMP-9 KO ligation groups in all three directions as compared to control or sham values. For the

loading cases examined the MMP-9 WT material model demonstrated increased stress as compared to the MMP-9 KO material model. Predicted displacement values (for the three axes of interest) appeared to be less affected by ligation model type (wild or knock out) as compared to stress prediction. Explicitly, variations in the predicted stress values between the WT and KO groups were greater than the displacement prediction variation. An apparent increase in the ratio between the predicted stress and the corresponding displacement (aka increased "material stiffness") was observed following ligation as compared to control and sham values. This point highlights the importance of the nonlinear modeling aspect of these vessels and changes in this nonlinear behavior due to the different experimental treatments. The correspondence between the material characterization and resultant displacement is not linearly correlated (as would be expected if linear elasticity were implemented), which means that the degree of nonlinearity is one of the primary concerns when one models these tissues. The FEMs based on the control and sham material coefficients demonstrated close proximity in their predicted stress and displacement values, however the effects of surgical intervention are apparent, as control and sham values are not identical.

For the normal physiologic pressure of 0.27 MPa the finite element simulations indicated that differences in the magnitude of displacement between the ligation groups and the sham groups are most pronounced in the circumferential direction. The analysis indicated that peak stress values for the ligated groups increased from 15% (luminal direction) to 50% (axial direction) as compared to the corresponding sham values. Decreases in displacement magnitude ranged from 10% (luminal direction) to

260% (circumferential direction). These finite element modeling simulations indicated that biomechanical structural changes following ligation lead to increased stress and decreased displacement in the three primary axes of loading. The FEM prediction further supports the theory that clinical complications from DVT arise from the affected vessels reduced capacity to distend are correct, as demonstrated by the reduction in vein wall compliance following ligation observed in the three axes of interest under all pressure loads. The data conclusively demonstrates that DVT resolution created experimentally via full IVC ligation causes increased vein wall stress along with decreased vessel distention. This trend was observed in both the WT and KO out models as compared to sham and control values.

10.0 FINITE ELEMENT MODELING SUMMARY

In summary the finite element modeling and analysis indicated:

- FEM results demonstrated the decreased compliance of the vascular wall;
- Simulated stresses were increased for the ligation groups as compared to sham and control groups;
- Simulated displacements were decreased for the ligation groups as compared to sham and control groups;
- Peak stress values were measured in the circumferential direction of loading as compared against the other primary axes;

- The data conclusively demonstrate that DVT resolution created experimentally via full IVC ligation causes increased vein wall stress along with decreased vessel distention.

11.0 FUTURE WORK

While the current study represents a significant first attempt to describe the mechanical alterations associated with DVT, future research is warranted in order to fully understand the biomechanical effects secondary to deep vein thrombosis. This analysis did not examine the viscoelastic response of the tissue. The viscoelastic response of venous tissue is fundamental to the vessel's physiologic function, and future efforts to characterize this aspect of the vein's mechanical behavior should be focused in this area. A battery of biomechanical tests designed to specifically determine the viscoelastic parameters of both healthy and diseased venous tissue would further strength an understanding of DVT from a structural standpoint.

Histological information regarding changes in the constituents of the vein wall would help in understand the underlying reasons for changes in the biomechanical response of the tissue. Histological information would also be useful for more accurately simulating the geometric properties of the vein wall in FEM simulations. A more physiologic geometric representation would increase the accuracy of predicted output values. These histological data of the murine model would contribute to the structure - function understanding of the biomechanical response of the tissue measured.

With regard to clinical DVT resolution schema, utilizing the MMP-2 KO murine model might be an invaluable tool for developing future therapeutics. MMP-2 is known to contribute to the breakdown of the ECM and is believed to play a role in DVT. A biomechanical analysis of the effects of MMP-2 on the properties of venous tissue would give insight into which matrix metallopeptidase has the most deleterious effects on the tissue.

REFERENCES

1. Al-Sukhun, J., et al., *Microvascular stress analysis. Part I: simulation of microvascular anastomoses using finite element analysis.* Br J Oral Maxillofac Surg. , 2005. **45**(2): p. 130-137.

2. Alastrue, V., et al., *Experimental study and constitutive modelling of the passive mechanical properties of the ovine infrarenal vena cava tissue.* J Biomech, 2008. **41**(14): p. 3038-45.

3. Anderson, F.A., Jr. and H.B. Wheeler, *Physician practices in the management of venous thromboembolism: a community-wide survey.* J Vasc Surg, 1992. **16**(5): p. 707-14.

4. Apter, J.T. and E. Marquez, *A relation between hysteresis and other visco elastic properties of some biomaterials.* Biorheology, 1968. **5**(4): p. 285-301.

5. Azuma, T. and M. Hasegawa, *Distensibility of the vein: from the architectural point of view.* Biorheology, 1973. **10**(3): p. 469-79.

6. Bandick, N. and H. Sparks, *Viscoelastic properties of the aorta of hypertensive rats.* Proc Soc Exp Biol Med, 1970. **134**(1): p. 56-60.

7. Briscoe, B., L. Fiori, and E. Pelillo, *Nano-indentation of polymeric surfaces.* Journal of Physics D-Applied Pysics, 1998. **31**(19): p. 2395-2405.

8. Brossollet, L.J. and R.P. Vito, *An alternate formulation of blood vessel mechanics and the meaning of the in vivo property.* J Biomech, 1995. **28**(6): p. 679-87.

9. Brossollet, L.J. and R.P. Vito, *A new approach to mechanical testing and modeling of biological tissues, with application to blood vessels.* J Biomech Eng, 1996. **118**(4): p. 433-9.

10. Campbell, N. and J. Reece, *Biology*. Sixth ed. 2002, New York, New York: Benjamin Cummings.

11. CF, R., *Venous system: physiology of the capacitance vessel.*, in *Handbook of Physiology*. 1983, American Physiological Society: Bethesada, MD. p. 397-452.

12. Classen, J.N., *The post phlebitic syndrome.* Md State Med J, 1956. **5**(12): p. 739-42.

13. Cockett, F.B., *The post-phlebitic syndrome.* Proc R Soc Med, 1970. **63**(2): p. 131-2.

14. Cox, R.H., *Viscoelastic properties of canine pulmonary arteries.* Am J Physiol, 1984. **246**(1 Pt 2): p. H90-6.

15. Crawford, M., J. DiMarco, and W. Paulus, *Cardiology*. 2004, New York, New York: Mosby.

16. Davies, P.F., *Flow-mediated endothelial mechanotransduction.* Physiol Rev, 1995. **75**(3): p. 519-60.

17. Deatrick KB, et al., *Vein wall remodeling after deep vein thrombosis involves matrix metalloproteinases and late fibrosis in a mouse model.* J Vasc Surg, 2005. **42**(1): p. 140-8.

18. Debes, J.C. and Y.C. Fung, *Biaxial mechanics of excised canine pulmonary arteries.* Am J Physiol, 1995. **269**(2 Pt 2): p. H433-42.

19. Decamp, P.T. and A. Ochsner, *The post-phlebitic syndrome.* Postgrad Med J, 1952. **28**(324): p. 517-20.

20. Desch, G.W. and H.W. Weizsacker, *A model for passive elastic properties of rat vena cava.* J Biomech, 2007. **40**(14): p. 3130-45.

21. Dimitrios P. Sokolisa, et al., *A structural basis for the aortic stress–strain relation in uniaxial tension.* Journal of Biomechanics, 2005. **39**: p. 1651-1662.

22. Dobrin, P.B., *Mechanical properties of arterises.* Physiol Rev, 1978. **58**(2): p. 397-460.

23. Dobrin, P.B., *Mechanics of normal and diseased blood vessels.* Ann Vasc Surg, 1988. **2**(3): p. 283-94.

24. Ebenstein, D., *Biomechanical Characterization of Atherosclerotic Plaques: A Combined Nanoindentation and FTIR Approach*, in *Bioengineering*. 2002, University of California, Berkeley.

25. Ebenstein, D., et al., *A nanoindentation technique for functional evaluation of cartilage repair tissue.* J. Mater. Res., 2003. **19**(1): p. 273-281.

26. Ebenstein, L. and L. Pruitt, *Nanoindentation of soft hydrated materials for application to vascular tissues.* J Biomed Mater Res A., 2004. **69**(2): p. 222-232.

27. Elhadj, S., R. Chan, and K. Forsten-Williams, *Implementation of an optical method for the real-time determination of uniaxial strain and vessel mechanics.* IEEE Trans Biomed Eng, 2004. **51**(3): p. 536-8.

28. Frasher, W.G., Jr. and S.S. Sobin, *Pressure-volume response of isolated living main pulmonary artery in dogs.* J Appl Physiol, 1965. **20**(4): p. 675-82.

29. Fung, Y.C., *Biomechanics: Mechanical Properties of Living Tissues.* 1981.

30. Galis ZS, et al., *Increased expression of matrix metalloproteinases and matrix degrading activity in vulnerable regions of human atherosclerotic plaques.* J Clin Invest, 1994. **94**(6): p. 2493-503.

31. Gasser, T.C., R.W. Ogden, and G.A. Holzapfel, *Hyperelastic modelling of arterial layers with distributed collagen fibre orientations.* J R Soc Interface, 2006. **3**(6): p. 15-35.

32. Gupta, S., et al., *Adhesive forces signigicantly affect elastic modulus determination of soft polymeric materials in nanoindentation.* Materials Letters, 2007. **61**: p. 448-451.

33. Haviarova, Z., et al., *The determination of the collagen and elastin amount in the human varicose vein by the computer morphometric method.* Gen Physiol Biophys, 1999. **18 Suppl 1**: p. 30-3.

34. Hayashi, K., *Experimental approaches on measuring the mechanical properties and constitutive laws of arterial walls.* J Biomech Eng, 1993. **115**(4B): p. 481-8.

35. Henke, P.K., et al., *Deep vein thrombosis resolution is modulated by monocyte CXCR2-mediated activity in a mouse model.* Arterioscler Thromb Vasc Biol, 2004. **24**(6): p. 1130-7.

36. Holzapfel, G.A., *Determination of material models for arterial walls from uniaxial extension tests and histological structure.* J Theor Biol, 2006. **238**(2): p. 290-302.

37. Holzapfel, G.A., T.C. Gasser, and R.W. Ogden, *Comparison of a multi-layer structural model for arterial walls with a fung-type model, and issues of material stability.* J Biomech Eng, 2004. **126**(2): p. 264-75.

38. Holzapfel, G.A., T.C. Gasser, and R.W. Ogden, *A New Constitutive Framework for Arterial Wall Mechanics and a Comparative Study of Material Models.* Journal of Elasticity, 2000. **61**: p. 1-48.

39. Humphrey, J.D., *Mechanics of the arterial wall: review and directions.* Crit Rev Biomed Eng, 1995. **23**(1-2): p. 1-162.

40. Humphrey, J.D., D.L. Vawter, and R.P. Vito, *Quantification of strains in biaxially tested soft tissues.* Journal of Biomechanics, 1987. **20**: p. 59-65

41. Humphries J, et al., *Monocyte chemotactic protein-1 (MCP-1) accelerates the organization and resolution of venous thrombi.* J Vasc Surg, 1999. **30**(5): p. 894-9.

42. Ip JH, et al., *Syndromes of accelerated atherosclerosis: role of vascular injury and smooth muscle cell proliferation.* J Am Coll Cardiol., 1990. **15**(7): p. 1667-87.

43. Jacot, J., et al., *A simple microindentation technique for mapping the microscale compliance of soft hydrated materials and tissues.* Journal of Biomedical Materials Research, 2006: p. 485-494.

44. Jimenez Rios, J.L., P.S. Steif, and Y. Rabin, *Stress-strain measurements and viscoelastic response of blood vessels cryopreserved by vitrification.* Ann Biomed Eng, 2007. **35**(12): p. 2077-86.

45. Kong, S.K. and N.L. Stephens, *Mechanical properties of pulmonary arteries from sensitized dogs.* J Appl Physiol, 1983. **55**(6): p. 1669-73.

46. Labropoulos, N., et al., *Viscoelastic properties of normal and atherosclerotic carotid arteries.* Eur J Vasc Endovasc Surg, 2000. **19**(3): p. 221-5.

47. Lichtenstein, O., et al., *Biaxial mechanical properties of carotid arteries from normotensive and hypertensive rats.* Hypertension, 1995. **26**(1): p. 15-9.

48. Lillie MA and G. JM., *Mechanical properties of elastin along the thoracic aorta in the pig.* J Biomech, 2007. **40**(10): p. 2214-21.

49. Line BR, *Pathophysiology and Diagnosis of Deep Venous Thrombosis.* Seminars in Nuclear Medicine, 2001. **XXXL**(2): p. 90-101.

50. MacDougall, D.A., et al., *Economic burden of deep-vein thrombosis, pulmonary embolism, and post-thrombotic syndrome.* Am J Health Syst Pharm, 2006. **63**(20 Suppl 6): p. S5-15.

51. Mackay, E.H., et al., *Structural basis for the changing physical properties of human pulmonary vessels with age.* Thorax, 1978. **33**(3): p. 335-44.

52. Marchena Yglesias, P.J., et al., *[Acute-phase reactants and markers of inflammation in venous thromboembolic disease: correlation with clinical and evolution parameters].* An Med Interna, 2006. **23**(3): p. 105-10.

53. Marquardt, D.W., *An Algorithm for Least Squares Estimation of Nonlinear Parameters.* Journal of the Society of Industrial and Applied Mathematics, 1963. **11**: p. 431-441.

54. McGuinness CL, et al., *A new model of venous thrombosis.* Cardiovasc Surg, 1997. **5**(123).

55. Milnor, W., *Cardiovascular Physiology*. 1990, New York, New York: Oxford University Press.

56. Minten, J., et al., *Correlation between mechanical properties and wall composition of the canine superior vena cava.* Arch Int Physiol Biochim, 1986. **94**(5): p. 349-62.

57. Moaveni, D.K., et al., *Vein wall re-endothelialization after deep vein thrombosis is improved with low-molecular-weight heparin.* J Vasc Surg, 2008. **47**(3): p. 616-24.

58. Molnar, A.A., et al., *Generalized changes in venous distensibility in postthrombotic patients.* Thromb Res, 2006. **117**(6): p. 639-45.

59. Monos, E., *Biomechanical aspects of blood vessel function.* Connect Tissue Res, 1986. **15**(1-2): p. 85-96.

60. Monos, E., V. Berczi, and G. Nadasy, *Local control of veins: biomechanical, metabolic, and humoral aspects.* Physiol Rev, 1995. **75**(3): p. 611-66.

61. Monos, E. and A.G. Kovach, *Biomechanical properties of splenic artery.* Acta Physiol Acad Sci Hung, 1980. **55**(4): p. 355-64.

62. Moreno, A.H., et al., *Mechanics of distension of dog veins and other very thin-walled tubular structures.* Circ Res, 1970. **27**(6): p. 1069-80.

63. Nagasawa, S., *[Biomechanical study of human cerebral arteries (author's transl)].* Nippon Geka Hokan, 1980. **49**(5): p. 620-36.

64. Nerem, R.M., *Role of mechanics in vascular tissue engineering.* Biorheology, 2003. **40**(1-3): p. 281-7.

65. Norwich, I., *The post-phlebitic syndrome of the lower limb.* S Afr Med J, 1953. **27**(32): p. 663-72.

66. Novak, V.P., F.C. Yin, and J.D. Humphrey, *Regional mechanical properties of passive myocardium.* J Biomech, 1994. **27**(4): p. 403-12.

67. O'Brien, J.A. and J.J. Caro, *Direct medical cost of managing deep vein thrombosis according to the occurrence of complications.* Pharmacoeconomics, 2002. **20**(9): p. 603-15.

68. O'Rourke, M.F. and G. Mancia, *Arterial stiffness.* J Hypertens, 1999. **17**(1): p. 1-4.

69. Okamoto, R.J., et al., *Mechanical properties of dilated human ascending aorta.* Ann Biomed Eng, 2002. **30**(5): p. 624-35.

70. Olin, J.W., et al., *Medical costs of treating venous stasis ulcers: evidence from a retrospective cohort study.* Vasc Med, 1999. **4**(1): p. 1-7.

71. Oliver, W.C. and G.M. Pharr, *An Improved Technique for Determining Hardness and Elastic Modus Using Load and Displacement Sensing Indentation Experiments.* Journal of Material Research, 1992. **7**: p. 1564-1584.

72. Patel, D.J., J.S. Janicki, and T.E. Carew, *Static anisotropic elastic properties of the aorta in living dogs.* Circ Res, 1969. **25**(6): p. 765-79.

73. Plante, G.E., *Vascular response to stress in health and disease.* Metabolism, 2002. **51**(6 Suppl 1): p. 25-30.

74. Rhodin, J.A., *Ultrastructure of mammalian venous capillaries, venules, and small collecting veins.* J Ultrastruct Res, 1968. **25**(5): p. 452-500.

75. Ross, R., *Atherosclerosis--an inflammatory disease.* N Engl J Med, 1999. **340**(2): p. 115-126.

76. Ross, R., *Atherosclerosis is an inflammatory disease.* Am Heart J., 1999. **138**(5 Pt. 2): p. S419-20.

77. Roy, S., P. Silacci, and N. Stergiopulos, *Biomechanical properties of decellularized porcine common carotid arteries.* Am J Physiol Heart Circ Physiol, 2005. **289**(4): p. H1567-76.

78. Ruigomez, J., *Biomechanical Factors: Influence on Cardiovascular Function.* Rev Esp Cardiol., 2005. **58**(2): p. 121-125.

79. Sacks, M.S., *A method for planar biaxial mechanical testing that includes in-plane shear.* J Biomech Eng, 1999. **121**(5): p. 551-5.

80. Sacks, M.S. and C.J. Chuong, *Biaxial mechanical properties of passive right ventricular free wall myocardium.* J Biomech Eng, 1993. **115**(2): p. 202-5.

81. Sacks, M.S. and C.J. Chuong, *Orthotropic mechanical properties of chemically treated bovine pericardium.* Ann Biomed Eng, 1998. **26**(5): p. 892-902.

82. Sacks, M.S. and W. Sun, *Multiaxial mechanical behavior of biological materials.* Annu Rev Biomed Eng, 2003. **5**: p. 251-84.

83. Salunke, N. and L. Topoleski, *Biomechanics of atherosclerotic plaque.* Crit Rev Biomed Eng, 1997. **25**(3): p. 243-85.

84. Scott, P.J., *The arterial wall and the process of atherosclerosis.* N Z Med J, 1973. **77**(488): p. 1-6.

85. Singh, R., et al., *Role for tissue factor pathway in murine model of vascular remodeling.* Circ Res, 2001. **89**(1): p. 71-6.

86. Sneddon, I.N., *The relation between load and penetration in the axisymmetric boussinesq problem for a punch of arbitrary profile.* Int J Engng Sci, 1965. **3**: p. 47-57.

87. Spyropoulos, A.C. and J. Lin, *Direct medical costs of venous thromboembolism and subsequent hospital readmission rates: an administrative claims analysis from 30 managed care organizations.* J Manag Care Pharm, 2007. **13**(6): p. 475-86.

88. Stary, H., *Atlas of Atheroscolerosis Progression and Refression*. 2nd ed. 2003, New York, NY: The Parthenon Publishing Group Inc.

89. Stemper, B.D., et al., *Biomechanical characterization of internal layer subfailure in blunt arterial injury.* Ann Biomed Eng, 2007. **35**(2): p. 285-91.

90. Sun, W. and M.S. Sacks, *Finite element implementation of a generalized Fung-elastic constitutive model for planar soft tissues.* Biomech Model Mechanobiol, 2005. **4**(2-3): p. 190-9.

91. Topoleski, L.D. and N.V. Salunke, *Mechanical behavior of calcified plaques: a summary of compression and stress-relaxation experiments.* Z Kardiol, 2000. **89 Suppl 2**: p. 85-91.

92. Touw, D.M., M.H. Sherebrin, and M.R. Roach, *The elastic properties of canine abdominal aorta at its branches.* Can J Physiol Pharmacol, 1985. **63**(11): p. 1378-83.

93. Vande Geest, J.P., M.S. Sacks, and D.A. Vorp, *Age dependency of the biaxial biomechanical behavior of human abdominal aorta.* J Biomech Eng, 2004. **126**(6): p. 815-22.

94. Vande Geest, J.P., M.S. Sacks, and D.A. Vorp, *A planar biaxial constitutive relation for the luminal layer of intra-luminal thrombus in abdominal aortic aneurysms.* J Biomech, 2006. **39**(13): p. 2347-54.

95. Venkatasubramanian, R.T., et al., *Effects of freezing and cryopreservation on the mechanical properties of arteries.* Ann Biomed Eng, 2006. **34**(5): p. 823-32.

96. Venturi, M., et al., *Biochemical assay of collagen and elastin in the normal and varicose vein wall.* J Surg Res, 1996. **60**(1): p. 245-8.

97. Vesely, I., et al., *Mechanical testing of cryopreserved aortic allografts. Comparison with xenografts and fresh tissue.* J Thorac Cardiovasc Surg, 1990. **99**(1): p. 119-23.

98. Vito, R.P. and J. Hickey, *The mechanical properties of soft tissues--II: the elastic response of arterial segments.* J Biomech, 1980. **13**(11): p. 951-7.

99. Weizsacker, H.W., *Passive elastic properties of the rat abdominal vena cava.* Pflugers Arch, 1988. **412**(1-2): p. 147-54.

100. Wesly, R.L., et al., *Static linear and nonlinear elastic properties of normal and arterialized venous tissue in dog and man.* Circ Res, 1975. **37**(4): p. 509-20.

101. Wesseling, K.H., H. Weber, and B. de Wit, *Estimated five component viscoelastic model parameters for human arterial walls.* J Biomech, 1973. **6**(1): p. 13-24.

102. Wiederhielm, C.A., *Viscoelastic properties of relaxed and constricted arteriolar walls.* Bibl Anat, 1965. **7**: p. 346-52.

103. Wu, S.G. and G.C. Lee, *On nonlinear viscoelastic properties of arterial tissue.* J Biomech Eng, 1984. **106**(1): p. 42-7.

104. Wurzel, M., G.R. Cowper, and J.M. McCook, *Smooth muscle contraction and viscoelasticity of arterial wall.* Can J Physiol Pharmacol, 1970. **48**(8): p. 510-23.

105. Xu, Y., et al., *Effects of freezing rates and dimethyl sulfoxide concentrations on thermal expansion of rabbit aorta during freezing phase change as measured by thermo mechanical analysis.* J Biomech, 2007. **40**(14): p. 3201-6.

106. Yoshida, W.B., et al., *Tensile strength and histological changes of abdominal aorta of malnourished rats.* Cardiovasc Surg, 1995. **3**(4): p. 437-9.

107. Zhang, W., et al., *The effect of longitudinal pre-stretch and radial constraint on the stress distribution in the vessel wall: a new hypothesis.* Mech Chem Biosyst, 2005. **2**(1): p. 41-52.

108. Zhang, W. and G.S. Kassab, *A bilinear stress-strain relationship for arteries.* Biomaterials, 2007. **28**(6): p. 1307-15.

109. Zhou, J. and Y.C. Fung, *The degree of nonlinearity and anisotropy of blood vessel elasticity.* Proc Natl Acad Sci U S A, 1997. **94**(26): p. 14255-60.

APPENDIX A - Strain Energy Function Partial Derivatives

Strain Energy Function built into Abaqus CAE has the form:

$$\Psi(I_1,I_4,I_6) = C_{10}\cdot(I_1 - 3) + \frac{k_1}{2\cdot k_2}\cdot\sum_{\alpha=1}^{N}\left[e^{k_2\cdot\left[\kappa\cdot(I_1-3)+(1-3\cdot\kappa)\cdot(I_\beta-1)\right]^2} - 1\right]$$

$\beta = 4,6$

This formulation was taken from Holzapfel et al.

<u>The partial derivative with respect to the strain invariants are computed as follows</u>

$$\frac{\partial}{\partial I_1}\Psi(I_1,I_4,I_6) = \frac{\partial}{\partial I_1}\left[\begin{array}{l} C_{10}\cdot(I_1 - 3) + \frac{k_1}{2\cdot k_2}\cdot\left[e^{k_2\cdot\left[\kappa\cdot(I_1-3)+(1-3\cdot\kappa)\cdot(I_4-1)\right]^2} - 1\right]\ldots \\ + \frac{k_1}{2\cdot k_2}\cdot\left[e^{k_2\cdot\left[\kappa\cdot(I_1-3)+(1-3\cdot\kappa)\cdot(I_6-1)\right]^2} - 1\right] \end{array}\right]$$

$$\begin{aligned}\frac{\partial}{\partial I_1}\Psi(I_1,I_4,I_6) = {} & C_{10} + \kappa\cdot k_1\cdot e^{k_2\cdot\left[\kappa\cdot(I_1-3)-(I_4-1)\cdot(3\cdot\kappa-1)\right]^2}\cdot\left[\kappa\cdot(I_1 - 3) - (I_4 - 1)\cdot(3\cdot\kappa - 1)\right]\ldots \\ & + \kappa\cdot k_1\cdot e^{k_2\cdot\left[\kappa\cdot(I_1-3)-(I_6-1)\cdot(3\cdot\kappa-1)\right]^2}\cdot\left[\kappa\cdot(I_1 - 3) - (I_6 - 1)\cdot(3\cdot\kappa - 1)\right]\end{aligned}$$

$$\frac{\partial}{\partial I_4}\Psi(I_1,I_4,I_6) = \frac{\partial}{\partial I_4}\left[\begin{array}{l} C_{10}\cdot(I_1 - 3) + \frac{k_1}{2\cdot k_2}\cdot\left[e^{k_2\cdot\left[\kappa\cdot(I_1-3)+(1-3\cdot\kappa)\cdot(I_4-1)\right]^2} - 1\right]\ldots \\ + \frac{k_1}{2\cdot k_2}\cdot\left[e^{k_2\cdot\left[\kappa\cdot(I_1-3)+(1-3\cdot\kappa)\cdot(I_6-1)\right]^2} - 1\right] \end{array}\right]$$

$$\frac{\partial}{\partial I_4}\Psi(I_1,I_4,I_6) = -k_1\cdot e^{k_2\cdot\left[\kappa\cdot(I_1-3)-(I_4-1)\cdot(3\cdot\kappa-1)\right]^2}\cdot(3\cdot\kappa - 1)\cdot\left[\kappa\cdot(I_1 - 3) - (I_4 - 1)\cdot(3\cdot\kappa - 1)\right]$$

$$\frac{\partial}{\partial I_6}\Psi(I_1,I_4,I_6) = \frac{\partial}{\partial I_6}\left[\begin{array}{l} C_{10}\cdot(I_1-3) + \frac{k_1}{2\cdot k_2}\cdot\left[e^{k_2\cdot\left[\kappa\cdot(I_1-3)+(1-3\cdot\kappa)\cdot(I_4-1)\right]^2} - 1\right] \ldots \\ + \frac{k_1}{2\cdot k_2}\cdot\left[e^{k_2\cdot\left[\kappa\cdot(I_1-3)+(1-3\cdot\kappa)\cdot(I_6-1)\right]^2} - 1\right] \end{array}\right]$$

$$\frac{\partial}{\partial I_6}\Psi(I_1,I_4,I_6) = -k_1\cdot e^{k_2\cdot\left[\kappa\cdot(I_1-3)-(I_6-1)\cdot(3\cdot\kappa-1)\right]^2}\cdot(3\cdot\kappa-1)\cdot\left[\kappa\cdot(I_1-3)-(I_6-1)\cdot(3\cdot\kappa-1)\right]$$

Where k_1, k_2, and κ are material parameters (k_1 dimensions of stress, k_2 and κ are dimensionless structure parameters)

$$I_1 = \lambda_{axial}^{\ 2} + \lambda_{circum}^{\ 2} + (\lambda_{axial}\cdot\lambda_{circum})^{-2}$$

$$I_4 = \lambda_{axial}^{\ 2}\cdot\sin(\gamma)^2 + \lambda_{circum}^{\ 2}\cdot\cos(\gamma)^2$$

For this analysis it is assumed:

$$I_6 = I_4 = \lambda_{axial}^{\ 2}\cdot\sin(\gamma)^2 + \lambda_{circum}^{\ 2}\cdot\cos(\gamma)^2$$

Where γ is a structure parameter denoting the angle between the circumference and mean orientation of the fiber families. $0 \le \kappa \le \frac{1}{3}$ Where κ=0 perfectly aligned fibers and κ=1/3 randomly distributed fibers. If the strain-energy function Ψ is based on strain invariants, we may regard Ψ as a function of the principle stretches λ_a, a = 1, 2, 3. Consequently, the principal Cauchy stresses σ_a, a =1,2,3 simply result in:

("Nonlinear Solid Mechanics - A continuum Approach for Engineering" by Gerhard A. Holzapfel 2000 page 219 equation 6.45)

$$\sigma_a = J^{-1}\cdot\lambda_a\cdot\frac{\partial}{\partial\lambda_a}\Psi = \lambda_a\cdot\frac{\partial}{\partial\lambda_a}\Psi \qquad a = 1,2,3$$

$$\Psi(\lambda_1,\lambda_2) = C_{10}\cdot\left[\left[\lambda_1^{\,2}+\lambda_2^{\,2}+(\lambda_1\cdot\lambda_2)^{-2}\right]-3\right]\ldots$$
$$+\frac{k_1}{2\cdot k_2}\cdot\left[e^{\,k_2\cdot\left[\kappa\cdot\left[\left[\lambda_1^{\,2}+\lambda_2^{\,2}+(\lambda_1\cdot\lambda_2)^{-2}\right]-3\right]+(1-3\cdot\kappa)\cdot\left[\left(\lambda_2^{\,2}\cdot\sin(\gamma)^2+\lambda_1^{\,2}\cdot\cos(\gamma)^2\right)-1\right]\right]^2}-1\right]\ldots$$
$$+\frac{k_1}{2\cdot k_2}\cdot\left[e^{\,k_2\cdot\left[\kappa\cdot\left[\left[\lambda_1^{\,2}+\lambda_2^{\,2}+(\lambda_1\cdot\lambda_2)^{-2}\right]-3\right]+(1-3\cdot\kappa)\cdot\left[\left(\lambda_2^{\,2}\cdot\sin(\gamma)^2+\lambda_1^{\,2}\cdot\cos(\gamma)^2\right)-1\right]\right]^2}-1\right]$$

$$\Psi(\lambda_1,\lambda_2) = C_{10}\cdot\left(\lambda_1^{\,2}+\lambda_2^{\,2}+\frac{1}{\lambda_1^{\,2}\cdot\lambda_2^{\,2}}-3\right)\ldots$$
$$+\frac{k_1\cdot\left[e^{\,k_2\cdot\left[(3\cdot\kappa-1)\cdot\left(\lambda_1^{\,2}\cdot\cos(\gamma)^2+\lambda_2^{\,2}\cdot\sin(\gamma)^2-1\right)-\kappa\cdot\left(\lambda_1^{\,2}+\lambda_2^{\,2}+\frac{1}{\lambda_1^{\,2}\cdot\lambda_2^{\,2}}-3\right)\right]^2}-1\right]}{k_2}$$

$$\sigma_1 = \lambda_1\cdot\frac{\partial}{\partial\lambda_1}\left[C_{10}\cdot\left(\lambda_1^{\,2}+\lambda_2^{\,2}+\frac{1}{\lambda_1^{\,2}\cdot\lambda_2^{\,2}}-3\right)\ldots\right.$$
$$\left.+\frac{k_1\cdot\left[e^{\,k_2\cdot\left[(3\cdot\kappa-1)\cdot\left(\lambda_1^{\,2}\cdot\cos(\gamma)^2+\lambda_2^{\,2}\cdot\sin(\gamma)^2-1\right)-\kappa\cdot\left(\lambda_1^{\,2}+\lambda_2^{\,2}+\frac{1}{\lambda_1^{\,2}\cdot\lambda_2^{\,2}}-3\right)\right]^2}-1\right]}{k_2}\right]$$

$$\sigma_2 = \lambda_2\cdot\frac{\partial}{\partial\lambda_2}\left[C_{10}\cdot\left(\lambda_1^{\,2}+\lambda_2^{\,2}+\frac{1}{\lambda_1^{\,2}\cdot\lambda_2^{\,2}}-3\right)\ldots\right.$$
$$\left.+\frac{k_1\cdot\left[e^{\,k_2\cdot\left[(3\cdot\kappa-1)\cdot\left(\lambda_1^{\,2}\cdot\cos(\gamma)^2+\lambda_2^{\,2}\cdot\sin(\gamma)^2-1\right)-\kappa\cdot\left(\lambda_1^{\,2}+\lambda_2^{\,2}+\frac{1}{\lambda_1^{\,2}\cdot\lambda_2^{\,2}}-3\right)\right]^2}-1\right]}{k_2}\right]$$